Simulation of Transverse Multi-Bunch Instabilities of Proton Beams in LHC

Dissertation zur Erlangung des akademischen Titels
Doktor der technischen Wissenschaften

Eingereicht an der Technisch-Naturwissenschaftlichen Fakultät
der Technischen Universität Graz

Durchgeführt am europäischen
Elementarteilchen-Forschungszentrum CERN, CH-1211 Genève 23,
und am Institut für Theoretische Physik der TU Graz, A-8010 Graz,

von
Alexander Koschik

CERN & Technische Universität Graz,
Genf und Graz, 2004

Abstract

The CERN Large Hadron Collider (LHC) is designed for highest luminosity and therefore requires operation with a large number of bunches and high intensities. Its performance could be limited by the electromagnetic interaction between the charged particle beam and its surroundings which cause collective instabilities.

This thesis describes methods of simulating and analyzing multi-bunch instabilities in circular accelerators and storage rings. The simulation models as well as analyzing tools presented here, also facilitate the interpretation of measurements in multi-bunch machines.

The 3-dimensional, multi-bunch tracking program *MultiTRISIM* was developed, based on its single-bunch predecessor TRISIM3D. It allows the exploration of long-range effects in round or flat vacuum chambers for equidistant or uneven filling schemes.

Previous computer simulations of collective effects concentrated mainly on instabilities of single or few bunches in electron storage rings. There, the strong radiation damping reduces the required simulation time to a few thousand turns at most. For multi-bunch proton beams, however, where radiation damping is weak, much longer computation times are needed. Also the modelling of long-range wakes due to higher order modes and other impedances is computationally quite challenging. Therefore approximations have been investigated carefully. A method has been implemented allowing fast wake summation, which is based on the convolution theorem and the discrete FFT.

The resistive wall instability is a major concern for the LHC, in particular since collimators made of graphite are installed. Well-known and recently developed resistive wall impedance models have been compared, and the wake function required for time domain simulation has been obtained in analytical form for one of the models.

The simulation program has been verified by making predictions for the effects of impedances on proton beams in the CERN SPS and comparing them with measurements.

The results of multi-bunch and/or multi-turn simulations of LHC are presented. Various performance issues related to the resistive wall effect of the collimators have been simulated and analyzed. The partial filling scheme of the LHC beam has been taken into account. The simulation shows that the proposed octupole strengths are adequate to stabilize the LHC beam at top energy.

Keywords:
collective effects; resistive wall impedance; computer simulation; multi-bunch instabilities; coupled-bunch modes; long-range wake fields; particle accelerators.

Zusammenfassung

Der CERN Large Hadron Collider (LHC) ist für höchste Luminosität ausgelegt. Dies erfordert einen Beschleunigerbetrieb mit vielen Teilchenpaketen und hohen Intensitäten. Die maximale Leistung könnte durch die elektromagnetische Wechselwirkung zwischen dem Teilchenstrahl und seiner Umgebung begrenzt werden, da diese kollektive Instabilitäten verursachen kann.

Diese Doktorarbeit beschreibt Simulationsmethoden und Analyseverfahren von kollektiven Instabilitäten, verursacht durch mehrere Teilchenpakete im Beschleuniger. Die dargestellten Simulationsmodelle und Analyseverfahren helfen auch, Messungen in realen Beschleunigern besser zu interpretieren.

Das 3-dimensionale Simulationsprogramm *MultiTRISIM* für die Bewegung mehrerer Teilchenpakete wurde entwickelt, ausgehend von dem früheren Simulationsprogramm TRISIM3D für einzelne Teilchenpakete. Es erlaubt die Untersuchung von Langzeiteffekten verursacht durch den ohmschen Widerstand der Vakuumkammerwand oder durch resonante Impedanzen in runden oder flachen Vakuumkammern. Das Programm erlaubt die Simulation von Teilchenstrahlen mit äquidistanten Paketen und auch unsymmetrischen Füllungen.

Frühere Computersimulationen von kollektiven Effekten konzentrierten sich hauptsächlich auf Instabilitäten von einzelnen Teilchenpaketen in Elektronen-Speicherringen. Dort bewirkt die starke Synchrotron-Strahlung eine rasche Dämpfung der Teilchenbewegung und verringert somit die erforderliche Simulationszeit auf wenige tausend Umläufe. Für Protonen ist diese Dämpfung schwach, daher werden viel längere Simulationszeiten benötigt. Die Modellierung der Langzeiteffekte durch Resonatoren und resistive Wände ist ebenfalls rechnerisch zeitaufwendig. Daher wurden zulässige Näherungen sorgfältig untersucht. Eine Methode zur raschen Summierung von Wake-Feldern wurde gefunden, welche auf dem Faltungstheorem und der diskreten FFT basiert.

Für den Betrieb von LHC ist die Instabilität, die durch den ohmschen Widerstand der Vakuumkammern und den aus Graphit bestehenden Strahlkollimatoren angeregt wird, von besonderem Interesse.

Bekannte und kürzlich entwickelte Impedanzmodelle von resistiven Elementen wurden verglichen und für eine geeignete Impedanz die zugehörige Wake-Funktion in analytischer Form berechnet.

Die Ergebnisse des Simulationsprogramms wurden durch Vergleich mit Messungen am Protonenstrahl des CERN SPS unter denselben experimentellen Bedingungen verifiziert.

Resultate der Simulation von Langzeiteffekten im LHC werden präsentiert. Mehrere Impedanzen, welche die Leistung des Beschleunigers beeinträchtigen könnten, wurden simuliert. Insbesondere wurde der Einfluss der resistiven Wand und der Strahlkollimatoren untersucht. Die unsymmetrische Füllung der Maschine wurde berücksichtigt. Die Simulationsergebnisse zeigen, dass die Oktupole im LHC den Teilchenstrahl bei 7 TeV stabilisieren können.

Schlagwörter:
Kollektive Effekte; Impedanz von resistiven Wänden; Computersimulation; multiple Teilchenpakete; gekoppelte Schwingungsmoden; Langzeiteffekte; Teilchenbeschleuniger.

Acknowledgements

My thanks go to Dr. Bruno Zotter, my CERN tutor, who proposed the topic and guided and supported me in preparing this thesis. I would like to thank Prof. Bernhard Schnizer, my supervisor at the Institut für theoretische Physik, TU Graz, for his patience and support. Furthermore I would like to thank Dr. Daniel Brandt and Dr. Francesco Ruggiero, my CERN thesis supervisors, for their constant help and encouragement.

Thanks as well go to Helmut Burkhardt, Elias Métral, Daniel Schulte and Elmar Vogel of CERN AB-ABP group for their help and for many stimulating discussions.

The help and support of Angelika Lippitsch is gratefully acknowledged. Thanks to you so much.

Table of Contents

Chapter 1

Introduction

Particle accelerators are build to serve a wide range of applications. Although their original goal was and mainly still is to explore the elementary structure of of matter, nowadays the focus has also shifted towards medical and industrial applications. The layout and operational parameters may differ widely for a specific purpose, but their operation is based on common fundamental principles. Charged particles are moving in guiding electro-magnetic fields which keep them on the desired trajectory, and accelerating RF-fields which provide the energy needed to bring them to the design energy. The particles must be moving in a highly evacuated chamber in order to avoid collisions with molecules of the rest gas, which could lead to blow-up and beam loss.

Fields are induced by the charged particles in their surroundings, which are called wake fields. They limit the number of particles and can even cause instabilities. In addition to analytical studies of such collective effects which are limited to simplified situations, simulation programs are a valuable tool to investigate the effects, and their dependence on various parameters.

To be able to probe objects of ever smaller scale or greater masses, physicists need more powerful accelerators that operate with higher intensities at high event rates (i.e. high "luminosities") and at even higher energies. High intensities in charged particle bunches, paired with a large total number of bunches, are challenging in terms of collective effects, which comprise both single-bunch instabilities as well as multi-bunch instabilities.

Many simplifications must still be made to construct an “accelerator model” which can be studied with simulation techniques, in general they do not strongly influence the simulation results. The number of structures in an accelerator is usually too high to consider each of them separately, hence one concentrates their effects into fewer elements for an appropriate machine model. Also the number of particles in the accelerator has to be represented by a smaller number of macro-particles, each one consisting of a large number of real particles.

The wake fields induced by a bunch result in deflections of the particles which disturb their trajectories and distribution. An exact solution of this problem is not possible in a simulation program, since the numerical computation of wake potentials

is not fast enough to be repeated at every passage of a bunch through a structure. A possible way to avoid this problem is to expand the bunch distribution into a suitable set of basis functions for which the wake potentials can be precalculated. The wake potential of the actual distribution can then be obtained rapidly from the wake potentials of these basis functions.

An efficient technique to represent the particle distribution by a set of triangular-shaped basis functions [34] was further developed into a 3-dimensional multi-particle tracking program TRISIM3D [42]. This code was limited to single-bunch effects in electron machines like the Large Electron Positron Collider (LEP).

Part of the present thesis was the development of a simulation code which allows to study multi-bunch effects in proton machines such as the Large Hadron Collider (LHC). The main difference compared to the previous codes is the lack of radiation damping in the case of protons and the necessary inclusion of long-range wake fields because of the multi-bunch operation of LHC.

Long-range wake fields cannot be calculated exactly by numerical mesh codes due to the sensitivity of the wakes to unavoidable dimensional changes and cannot be kept in precalculated tables due to the limitations in storing massive amounts of data.

Thus for multi-bunch proton beams much longer computation times are required. The modelling of long-range wakes due to higher order modes and other impedances is likewise computationally challenging. Necessary approximations have been studied intensively. A method to allow fast wake summation, which is based on the convolution theorem and the discrete FFT, has been found.

A special focus has been put on the resistive wall effect, which is known to be critical for LHC top performance. Different available resistive wall impedance models have been compared and for the most likely the corresponding wake function has been derived. The outcome has been checked against results from electromagnetic field calculation codes and analytic field matching calculations.

1.1 CERN — LHC

CERN is the European Organization for High Energy Physics, the largest particle physics center in Europe, where physicists come to explore what matter is made of and what forces hold it together. CERN exists primarily to provide them with the necessary tools and infrastructure, such as *accelerators*, which accelerate particles to high energies and *detectors* to make elementary particle collisions visible.

From its early beginnings in 1954, CERN has continuously evolved over time. The accelerator complex at CERN is a succession of machines with increasingly higher energies, injecting the particle beams each time into the next one, which takes over to bring the beam to an energy even higher, and so on. The accelerator complex was always adapted to the physics to be studied. In the LHC era, the CERN accelerator chain will consist of the the following parts, which are also depicted in Fig. 1.1. A proton (or ion) source, a Linear Accelerator (LINAC), the PS Booster Ring, the Proton Synchrotron (PS), the Super Proton Synchrotron (SPS) and finally the LHC, Large Hadron Collider.

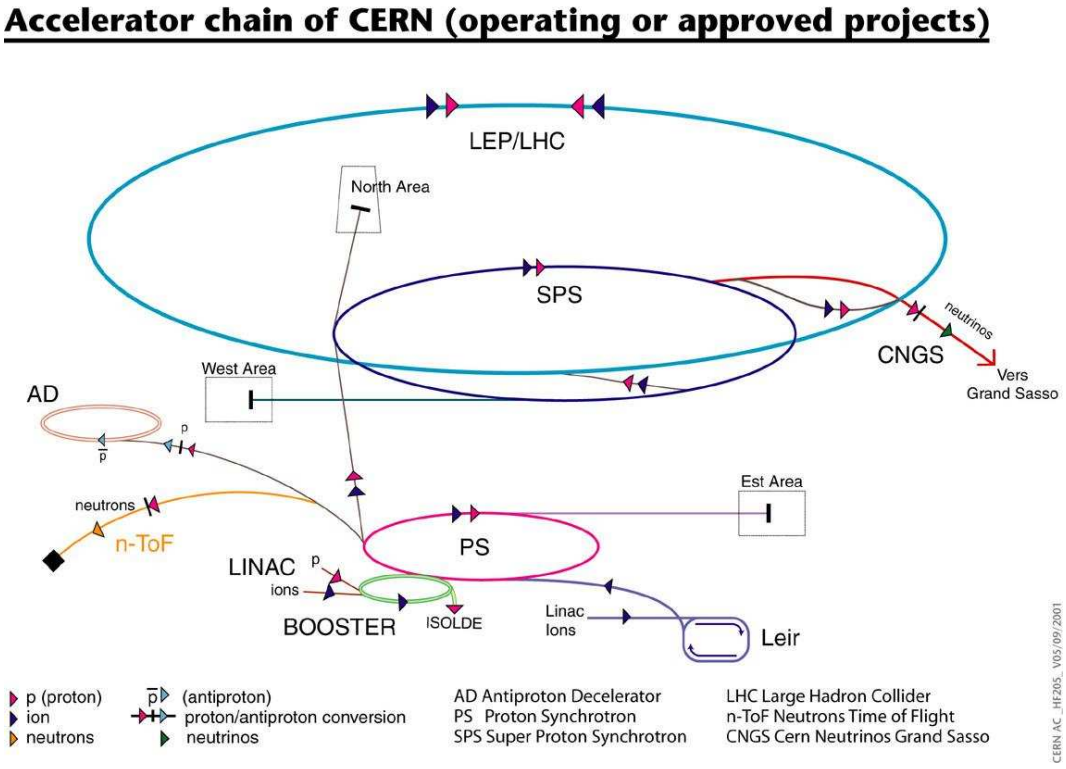

Figure 1.1: *The CERN accelerator complex in the year 2004.*

For physics studies there will be four experiments installed in the LHC, namely the ATLAS, ALICE, CMS and LHCb detectors, see also Fig. 1.2.

LHC Physics The effort of building such a large center of particle physics research is undertaken because our current understanding of the Universe is incomplete. The

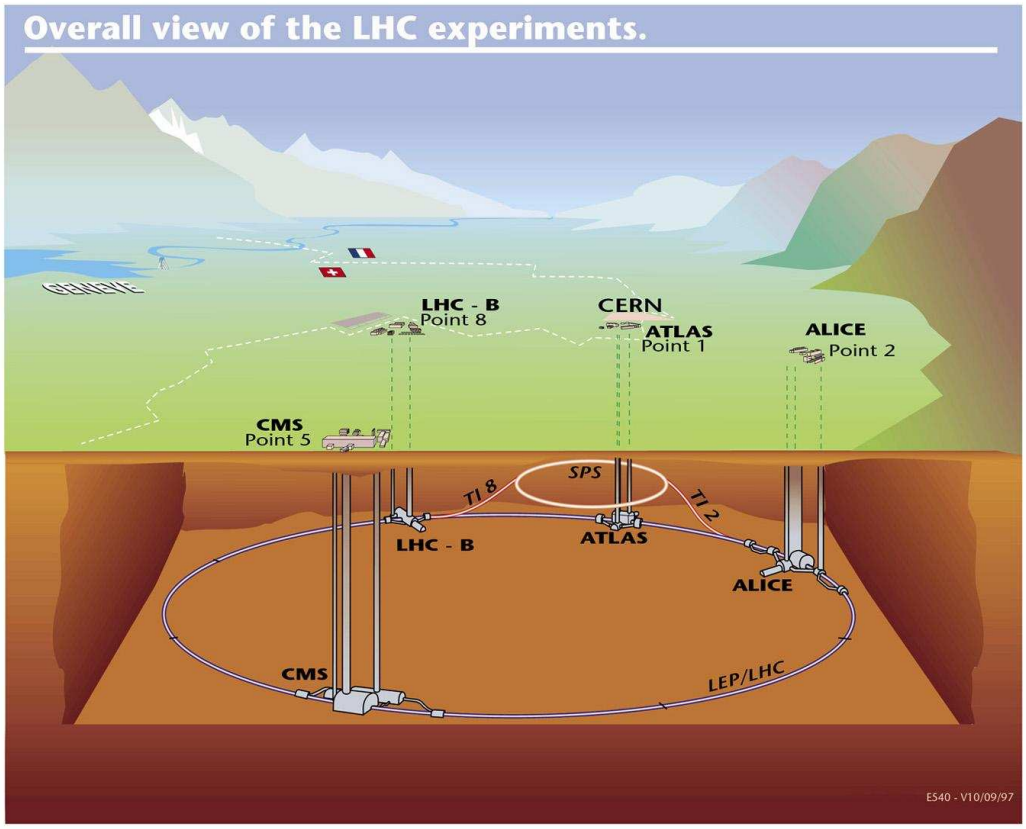

Figure 1.2: *Schematic overview of the Geneva area and CERN with the LHC tunnel and the experiments (ATLAS, ALICE, CMS, LHCb).*

latest basic theory, the "Standard Model", leaves many questions unsolved. Among them, the reason why elementary particles have mass, and why their masses differ is the most perplexing one.

The answer may lie in an idea called the "Higgs mechanism". According to this, the whole of space is filled with a 'Higgs field' and, by interacting with this field, particles acquire their masses. Particles which interact strongly with the Higgs field are heavy, whilst those which interact weakly are light. The Higgs field has at least one new particle associated with it, the Higgs boson. If such particle exists, the LHC will be able to make it detectable.

Furthermore, particle physicists hope to find a single theoretical framework where strong, weak, and electromagnetic forces and gravity are unified ("grand unification theory – GUT"). A very popular idea suggested by the unification of the forces is called "supersymmetry", or SUSY for short. SUSY predicts that for each known particle there is a 'supersymmetric' partner. If SUSY is right, then supersymmetric particles should also be found at the LHC.

Another riddle the LHC might help to solve as well is CP violation. The latter expression means that particles and antiparticles behave differently, especially CP

(charge-parity) asymmetry is needed to explain the separation of matter and antimatter in the very early universe and the imbalance of matter and antimatter in today's world. The understanding of CP violation will have an important impact on our understanding of the microscopic and macroscopic world, since the implications range from cosmology and astrophysics to elementary particle physics.

These are the main questions the LHC should answer, but although physicists have a good idea of what to expect, the greatest advances in science are often unexpected ("serendipity") and hence the LHC project is exciting in any sense.

The LHC accelerator In order to address the physics demands, the LHC pushes available technology to the limits. Superconducting magnets are used to keep the beam on track. With its 27 km circumference, the accelerator will be the largest superconducting installation in the world.

Because the LHC will accelerate two beams moving in opposite directions, it is really two accelerators in one. To keep the machine as compact and economical as possible, the magnets for both will be built into a single iron yoke with two beam channels ("2-in-1" housing).

The LHC is built in the same tunnel as CERN's Large Electron Positron collider (LEP). Proton beams will be prepared by CERN's existing accelerator chain before being injected into the LHC.

The 'standard' particles in LHC operation will be protons (fully ionized hydrogen atoms), but heavier ions such as Pb are foreseen as well. The particles start their journey at the source, where they are ionized by stripping off the electrons from the atoms. In the linear accelerator (LINAC) they are accelerated up to 50 MeV, then they enter the PS Booster, consisting of 4 superimposed synchrotrons, where they are further accelerated to 1 GeV. In the PS the kinetic energy of the particles is increased to 26 GeV and in the SPS to 450 GeV. Finally the particles enter the LHC at 450 GeV and are accelerated up to 7 TeV.

The machine will provide proton–proton collisions with a center-of-mass energy of 14 TeV and a luminosity of $10^{34}\mathrm{cm}^{-2}\mathrm{s}^{-1}$.

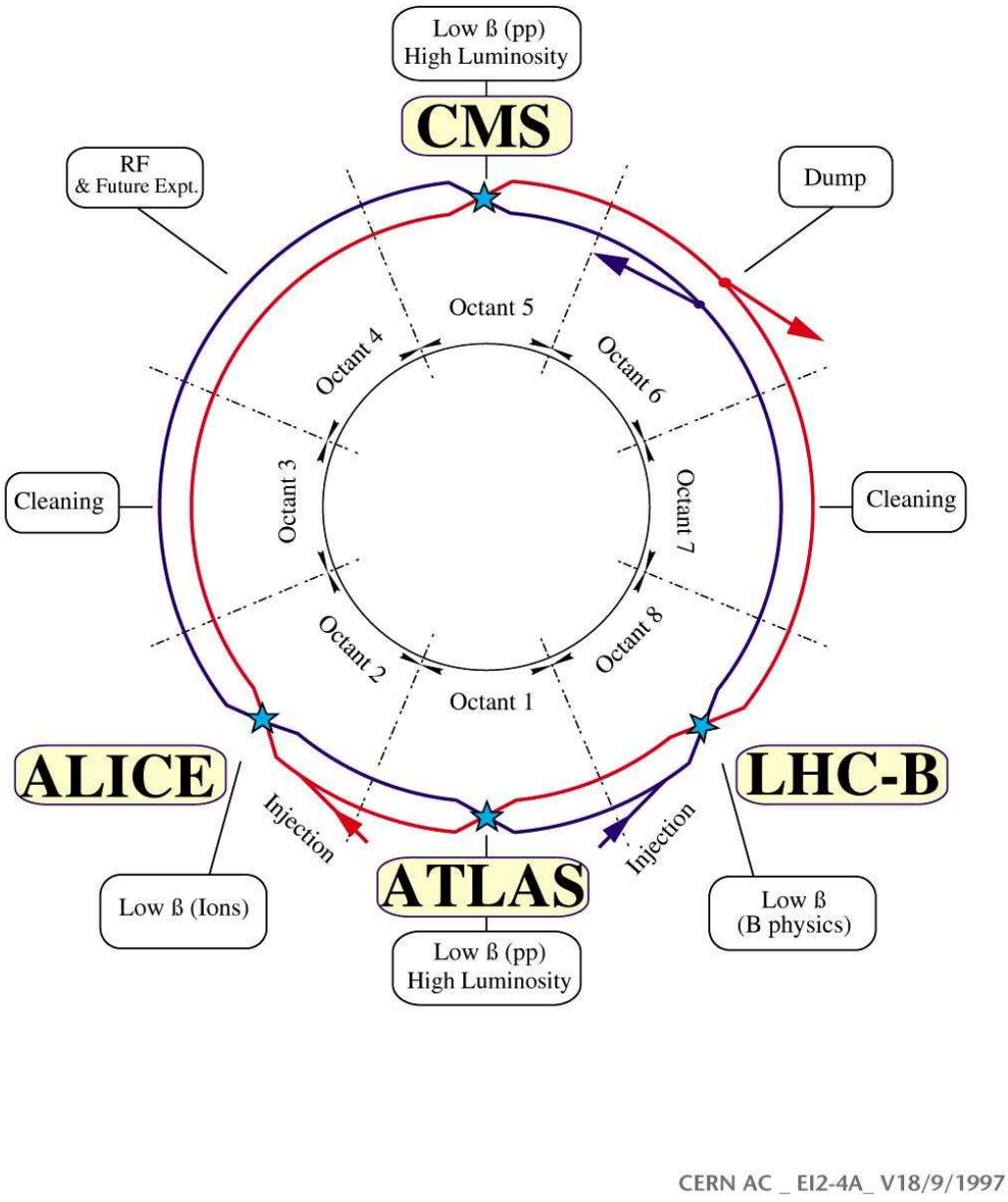

Figure 1.3: *Schematic layout of the LHC.*

1.2 Thesis Outline

The parameters of the LHC were chosen to maximize its performance. In order not to limit the beam current required for high luminosity, a lot of care has been taken to keep the impedance of the machine as low as possible. However, even after careful minimization of the impedance design, the beam may become unstable when it interacts with its surrounding through induced electromagnetic fields, so-called wake fields.

The fields induced by the head of a bunch can drive the tail of the bunch unstable. In frequency domain these wakes correspond to an impedance. Certain wake fields can remain in the beam pipe for a very long and hence they can also act on the following bunches or even on the exciting bunch itself after one or more turns.

The goal of this thesis is to develop a simulation code which allows the investigation of such long-range effects. The main issues therein are the correct modelling of long-range wake fields and their efficient implementation in a simulation code, which allows prediction of beam instabilities due to collective effects.

Chapter 2

Basic Concepts of Accelerator Physics and Collective Effects

In this chapter basic accelerator physics concepts will be reviewed. However we will keep the chapter short as details can be found in the literature [44, 16, 6].

A very short introduction to collective effects and instability theory will also be given, starting by introducing the quantities wake field, wake potential, wake function and impedances; and their use in stability analysis. An in-depth treatment can be found in [12, 48]. An excellent treatment on the multi-bunch instabilities can be found in [30].

2.1 Circular Accelerators and Storage Rings

An accelerator usually consists of a vacuum chamber surrounded by a long sequence of vacuum pumps, magnets, radio-frequency (RF) cavities, high voltage instruments and electronic circuits. Each of these elements has its specific function.

Here we are concentrating on circular machines, that means the particles are forced to move on a closed orbit. This is done by dipole magnets, whose magnetic force is always perpendicular to the velocity of the charged particles. The higher the energy of a particle, the stronger the field that is needed to bend it. As the maximum magnetic field is limited (to about 2 Tesla for conventional magnets, below 10 Tesla for superconducting ones), the more powerful a machine, the larger it needs to be.

To focus the particle beams, a sequence of alternating focusing and defocusing quadrupole magnets is used, which act like lenses in conventional optics. Additional higher order multipole magnets are used as correctors.

In order to accelerate the particles, RF cavities are installed, which are driven by powerful amplifiers. These provide the necessary energy to accelerate the particle beams.

2.2 Beam Dynamics (Linear Beam Optics)

The motion of charged particles in a circular accelerator are best described in a co-moving coordinate system, where x and y denote the horizontal and vertical position and s the longitudinal position on the particles orbit.

The force $\vec{F}$ acting on a charged particle with velocity $\vec{v}$ in a magnetic field $\vec{B}$ has the general form

$$\vec{F} = e\,(\vec{v} \times \vec{B}), \tag{2.1}$$

and the rate of change of momentum of the particle is given by

$$\frac{d\vec{p}}{dt} = \frac{d}{dt}\,(\gamma m_0\,\vec{v}) = e\,(\vec{v} \times \vec{B}). \tag{2.2}$$

A vertical magnetic field B_y bends the particles on a horizontal circular trajectory with radius ρ

$$F_x = ev\,B_y = \frac{\gamma m_0 v^2}{\rho}. \tag{2.3}$$

The quantity

$$\frac{1}{B\,\rho} = \frac{e}{p} \tag{2.4}$$

is called *magnetic rigidity*.

2.2.1 Transverse (Betatron) Motion

A synchrotron or storage ring consists of bending magnets (dipoles) and quadrupole magnets which provide focusing. In the focusing structure called FODO, alternating focusing and defocusing magnets are separated by straight sections or dipoles.

The focal length f of a quadrupole with strength k is given by

$$f = -\frac{1}{k\,l}, \tag{2.5}$$

where l is the length of the quadrupole and k the quadrupole gradient dB/dz normalized by the magnetic rigidity $B\,\rho$. If k is negative, the quadrupole is horizontally focusing and vertically defocusing.

The angular deflection (kick) given to a charged particle passing through a short quadrupole of length ds and strength k at a displacement z is

$$dz' = -k\,z\,ds.$$

The differential equation of motion deduced from this is

$$y'' + k(s)\,y = 0 \tag{2.6}$$

in the vertical plane and

$$x'' + \left[\frac{1}{\rho(s)^2} - k(s)\right]\,x = 0 \tag{2.7}$$

in the horizontal plane, where $rho(s)$ is the local bending radius and $k(s)$ is the local focusing strength.

This is Hill's equation, i.e. a second-order linear differential equation with periodic coefficient $k(s)$. Its periodic solution can be written as

$$x(s) = \sqrt{\beta(s)\,\epsilon}\,\cos\left[\psi(s) + \psi_0\right], \tag{2.8}$$

where

$$\phi(s) = \int \frac{ds}{\beta(s)} \tag{2.9}$$

is the *phase advance*, $\beta(s)$ is called the betatron function. The emittance ϵ measures the area of the described ellipse in phase space, which is an invariant of motion at constant energy.

Particles will oscillate transversely due to the alternating focusing structure and this so-called betatron oscillations are described by the solution of Hill's equation. The number of betatron wave lengths on one revolution is called the betatron tune Q given by

$$Q = \frac{1}{2\pi} \oint \frac{ds}{\beta(s)}.$$

The solution of any linear differential equation can also be written in matrix form, describing the transport of phase space coordinates from one point to another.

With the parameterization due to Courant and Snyder, the solution of Hill's equation can be written as the "Twiss matrix"

$$\begin{pmatrix} x(s_1) \\ x'(s_1) \end{pmatrix} = \mathbf{M} \cdot \begin{pmatrix} x(s_0) \\ x'(s_0) \end{pmatrix} \tag{2.10}$$

$$\mathbf{M} = \begin{pmatrix} \cos\mu + \alpha\sin\mu & \beta\sin\mu \\ -\gamma\sin\mu & \cos\mu - \alpha\sin\mu \end{pmatrix} \tag{2.11}$$

$$\begin{aligned} \alpha &= -\frac{\beta'}{2} \\ \gamma &= \frac{1+\alpha^2}{\beta} \end{aligned} \tag{2.12}$$

The particle's motion in phase space describes an ellipse according to this rotation matrix. The equation of the ellipse, often called the Courant and Snyder invariant, has the form

$$\gamma(s)x^2 + 2\alpha(s)xx' + \beta(s)x'^2 = \epsilon. \tag{2.13}$$

The area of the ellipse in phase space is called emittance ϵ.

Particles with a momentum deviation $\Delta p = p - p_0$ from the design momentum p_0 are bent differently in the dipoles. As a consequence the path length on one revolution of particles with a higher momentum $\Delta p/p_0 > 0$ is longer than the reference particles path length. This is expressed by the momentum compaction factor α_c defined as

$$\alpha_c = \frac{\Delta C}{C_0} \Big/ \frac{\Delta p}{p_0}\,, \tag{2.14}$$

which relates the relative change in orbit length to the momentum deviation.

For an off-momentum particle, Hill's equation can be written as

$$y'' + k(s)\, y = \frac{1}{\rho(s)}\, \frac{\Delta p}{p_0}, \tag{2.15}$$

and the solution can be written in the form

$$\begin{aligned} y(s) &= y_D(s) + y_\beta(s) \\ y_D(s) &= D(s)\, \frac{\Delta p}{p_0}, \end{aligned} \tag{2.16}$$

where $y_\beta(s)$ is the solution for the on-momentum particle and $D(s)$ is the dispersion function.

Off-momentum particles $\Delta p \neq 0$ are also focused differently in the quadrupoles. This results in a tune shift depending on relative momentum error

$$\Delta Q = \xi\, \frac{\Delta p}{p_0}, \tag{2.17}$$

where the quantity ξ is called chromaticity.

2.2.2 Longitudinal (Synchrotron) Motion

A particle circulates around the machine with a period or frequency:

$$T_0 = \frac{C}{\beta c}, \quad f_0 = \frac{\beta c}{2\pi R}, \tag{2.18}$$

where $C = 2\pi R$ is the circumference and βc is the velocity (β is the relativistic quantity).

The *synchronous particle* is defined as that particle which always arrives at the desired synchronous phase lag ϕ_s behind the rising zero-crossing of the RF wave in the cavity. For this to occur, the RF frequency, f_{RF}, must be an integer multiple of f_0:

$$f_{RF} = h\, f_0, \tag{2.19}$$

where h is also known as the harmonic number. It determines the places on the circumference where a particle could be located and arrive synchronously. The segments of the circumference centered on these points are called *buckets*. The groups of particles in these buckets are called *bunches*.

Depending on its phase lag ϕ with respect to the synchronous phase ϕ_s, a particle traversing the RF cavity will see the voltage V

$$V = V_0 \sin(\phi_s - \phi), \tag{2.20}$$

where V_0 is the RF peak voltage. By setting a synchronous phase ϕ_s, the resulting voltage V can be used to compensate energy losses through synchrotron radiation or to increase (decrease) the particle momentum.

Particles with less energy than the synchronous particle have a longer revolution time and hence arrive later at the RF cavity. If the RF voltage is such, that the particles arriving late see an additional voltage increment, they will be accelerated and overtake the synchronous particle. For particles arriving early the opposite applies.

Hence off-momentum particles ($\Delta p/p \neq 0$) will start to oscillate around the energy of the synchronous particle. The number of such oscillations per revolution is called synchrotron tune Q_s and given by

$$Q_s = \frac{f_s}{f} = \sqrt{\frac{|\eta|\, e\, h\, V_0}{2\pi\, E_0\, \beta^2 \gamma}}, \tag{2.21}$$

where f_s is the synchrotron frequency, β and γ are the relativistic quantities and E_0 is the energy of the synchronous particle. η is the fractional change in revolution frequency per unit of fractional change in momentum spread

$$\eta = \frac{\Delta f}{f_0} \Big/ \frac{\Delta p}{p_0} = \frac{1}{\gamma^2} - \alpha_c, \tag{2.22}$$

where α_c is the momentum compaction factor.

Below the transition energy

$$\gamma_{\mathrm{tr}} = \alpha_c^{-\frac{1}{2}} \tag{2.23}$$

particles with higher energies have *higher* revolution times, whereas above transition this picture is reversed.

It is appropriate to introduce the longitudinal phase space coordinates ϕ and $\Delta p/p$. The motion in longitudinal phase space is then given by the second order differential equation

$$\ddot{\phi} = -\frac{2\pi\, e\, V_0\, \eta\, h\, f^2}{E_0\, \beta^2\, \gamma}\, (\sin\phi - \sin\phi_s). \tag{2.24}$$

2.3 Wake Fields and Impedances

Charged particle beams interact electromagnetically with their vacuum chamber surroundings. The electromagnetic fields generated by an oscillating beam itself, through induced currents in the vacuum chamber walls, can drive the beam unstable by initiating transverse oscillations that grow in amplitude. The strength of the interaction of the beam with its environment is described in frequency domain by a coupling impedance. In time domain the interaction is conveyed by the same electromagnetic fields, and as the particles move at nearly the speed of light, those fields remain behind the exciting charge, therefore they are called wake fields [12, 16].

The wake field is given by the components of the electric and magnetic field $\vec{E}, \vec{B}$. The wake force experienced by a trailing test charge is of course given by the Lorentz force $\vec{F} = e(\vec{E} + c\vec{\beta}\vec{B})$, which has the components

$$\begin{aligned} F_{\parallel} &= eE_s \\ F_{\Theta} &= e\,(E_\theta + v_z \times B_r) \\ F_r &= e\,(E_r - v_z \times B_\theta) \end{aligned} \tag{2.25}$$

In general one is not interested in the wake fields directly (as it is anyway too complicated to calculate them for a whole ring), but in the integrated or averaged effect those fields have on the particle trajectory during one revolution in the machine. The normalized integral of the *EM* force over one revolution period defines the so-called wake potential. In the case of an elementary charge exciting the wake fields, the wake potential is called wake function. Impedances and wake functions are related through Fourier transforms.

The longitudinal and transverse wake function seen by a witness particle trailing at a distance z from the source particle are given by

$$W_{\parallel}(\vec{r_s}, \vec{r_w}, z) = -\frac{1}{q}\int_{-L}^{L} ds\, E_s(\vec{r_s}, \vec{r_w}, s, t = \frac{s+z}{c}) \tag{2.26}$$

$$W_{\perp}(\vec{r_s}, \vec{r_w}, z) = -\frac{1}{q\,\xi}\int_{-L}^{L} ds \left(\vec{E} + \vec{v} \times \vec{B}\right), \tag{2.27}$$

where $\vec{r_s}$ is the position of the source charge, $\vec{r_w}$ the position of the witness charge. $q\,\xi$ is the dipole moment, ξ being the displacement.

In case the excitation comes from a distribution of charged particles the wakepotential is given by the convolution of the wake function with line density $\lambda(t)$,

$$W_{pot}^{\parallel}\left(\tau = \frac{z}{c}\right) = \int_{-\infty}^{\tau} dt\, W_{\parallel}(\tau - t)\,\lambda(t) \tag{2.28}$$

$$= \int_{0}^{\infty} dt\, W_{\parallel}(t)\,\lambda(\tau - t) \tag{2.29}$$

$$W_{pot}^{\parallel}\left(\tau = \frac{z}{c}\right) = \int_{0}^{\infty} dt\, W_{\perp}(t)\,\lambda(\tau - t) \tag{2.30}$$

The electromagnetic interaction with the surrounding can also be described in the frequency domain where it is given by the coupling impedance $Z(\omega)$. It relates the induced voltage to the inducing current in frequency domain.

$$V(\omega) = -Z(\omega) \cdot I(\omega) \tag{2.31}$$

The coupling impedance is the Fourier transform of the wake function.

$$Z_{\parallel}(\omega) = \int_{-\infty}^{\infty} d\tau\, W_{\parallel}(\tau)\, \exp\left(-j\omega\tau\right) \tag{2.32}$$

$$Z_{\perp}(\omega) = \int_{-\infty}^{\infty} d\tau\, W_{\perp}(\tau)\, \exp\left(-j\omega\tau\right) \tag{2.33}$$

There are three main impedances present in a machine:

- Direct Space Charge impedance due to the Coulomb interaction between charged particles. It scales with $1/\gamma^2$ and can thus be neglected at high energies.
- Geometric impedances caused by cavities and cross section variations.
- Resistive Wall impedance due to the lossy material of the vacuum chamber wall.

The overlap of the beam spectrum and the impedance can be used as a measure for the beam stability. Therefore, the use of different impedance models will give different stability predictions/conclusions depending on the discrepancy of the impedance functions in frequency regions of large magnitude of the beam spectrum.

2.4 Collective Effects and instabilities

Wake fields induced by a collection of particles act back on the particles oscillation. If the oscillation amplitude is increased we have instability.

The betatron motion (transverse motion) of a particle can be written in the form

$$\frac{d^2x}{dt^2} + \omega_0^2 Q^2 x = 0 \qquad x(t) = \mathrm{Re}\left[A \cdot e^{i\,\omega_0 Q\,t}\right] \tag{2.34}$$

where ω_0 is the angular revolution frequency and Q is the tune. If a (wake) force F_x is acting on the particles motion the differential equation reads as

$$\frac{d^2x}{dt^2} + \omega_0^2 Q^2 x = \frac{F_x}{m_0\,\gamma}. \tag{2.35}$$

Suppose the force can be written as

$$\frac{F_x}{m_0\,\gamma} = K \cdot x, \tag{2.36}$$

then we can include the force term on the r.h.s. to get

$$\begin{aligned} \frac{d^2x}{dt^2} + \underbrace{\left(\omega_0^2 Q^2 - K\right)}\, x &= 0 \\ \left(\omega_0^2 Q^2 - K\right) &= \omega_0^2 \left(Q + \Delta Q\right)^2 = \\ &= \omega_0^2 \left(Q^2 + 2Q\,\Delta Q + \underbrace{(\Delta Q)^2}_{\approx 0} \right) \\ &\approx \omega_0^2 \left(Q^2 + 2\,Q\,\Delta Q\right). \end{aligned} \tag{2.37}$$

Therefore we identify

$$K = -2\,Q\,\Delta Q\,\omega_0^2 \qquad \Delta Q = -\frac{K}{2\,Q\omega_0^2}. \tag{2.38}$$

The differential equation and its solution now read as:

$$\begin{aligned} &\frac{d^2x}{dt^2} + \omega_0^2 \left(Q + \Delta Q\right)^2 x = 0 \\ &x(t) = \mathrm{Re}\left[A \cdot e^{i\,\omega_0 (Q + \Delta Q) t}\right]. \end{aligned} \tag{2.39}$$

It can be shown that the wake force F is directly proportional to the impedance Z and the total beam current I

$$F \propto -i\,Z \cdot I. \tag{2.40}$$

The impedance is a complex quantity, therefore in general $\Delta\Omega = \omega_0 \Delta Q$ will be complex (depending on the fields acting), so that we can write the solution as:

$$x(t) = \mathrm{Re}\left[A \cdot e^{i\,\omega_0 (Q + \mathrm{Re}[\Delta Q])t} \cdot e^{\omega_0\,\mathrm{Im}[\Delta Q]t}\right] \tag{2.41}$$

$\mathrm{Re}\,[\Delta Q]$	gives a real tuneshift
$\mathrm{Im}\,[\Delta Q]$	gives growth or damping
	$\frac{1}{\tau} = \mathrm{Im}\,[\Delta\Omega]$ is the growth rate.

Because $\Delta\Omega \propto i\,Z \cdot I$ the resistive part of the impedance causes growth and decay, while its reactive part gives real tuneshifts.

$\mathrm{Re}\,[Z]$	resistive part: growth / damping
$\mathrm{Im}\,[Z]$	reactive part: tuneshift
	$\Delta\Omega_{\max}$ defines tolerable $I_{\max}$
	$I_{\max}$ = threshold current.

2.5 Non-axially symmetric structures

In non-axially symmetric structures the wake fields no longer depend only on the offset x or y of the source charge, but also on the transverse position $\bar{x}$ and $\bar{y}$ of the test charge.

However, it has been shown [42], that the wake potential in such structures is mainly composed of a dipole component proportional to the source charge offset and a quadrupolar component proportional to the offset of the test charge.

$$\begin{aligned} W^{\mathrm{pot}}_{\perp,x}(x,y,\bar{x},\bar{y},s) &\approx x\,W^{\mathrm{pot}}_{\perp}(x,s) + \bar{x}\,W^{\mathrm{pot}}_{\perp}(\bar{x},s) \\ W^{\mathrm{pot}}_{\perp,y}(x,y,\bar{x},\bar{y},s) &\approx y\,W^{\mathrm{pot}}_{\perp}(x,s) + \bar{x}\,W^{\mathrm{pot}}_{\perp}(\bar{y},s) \end{aligned} \tag{2.42}$$

Fig. 2.1 depicts this situation graphically. To get the wake potentials in elliptic or rectangular structures the Yokoya factors [46] can be applied to the wake potentials of a corresponding circular symmetric structure.

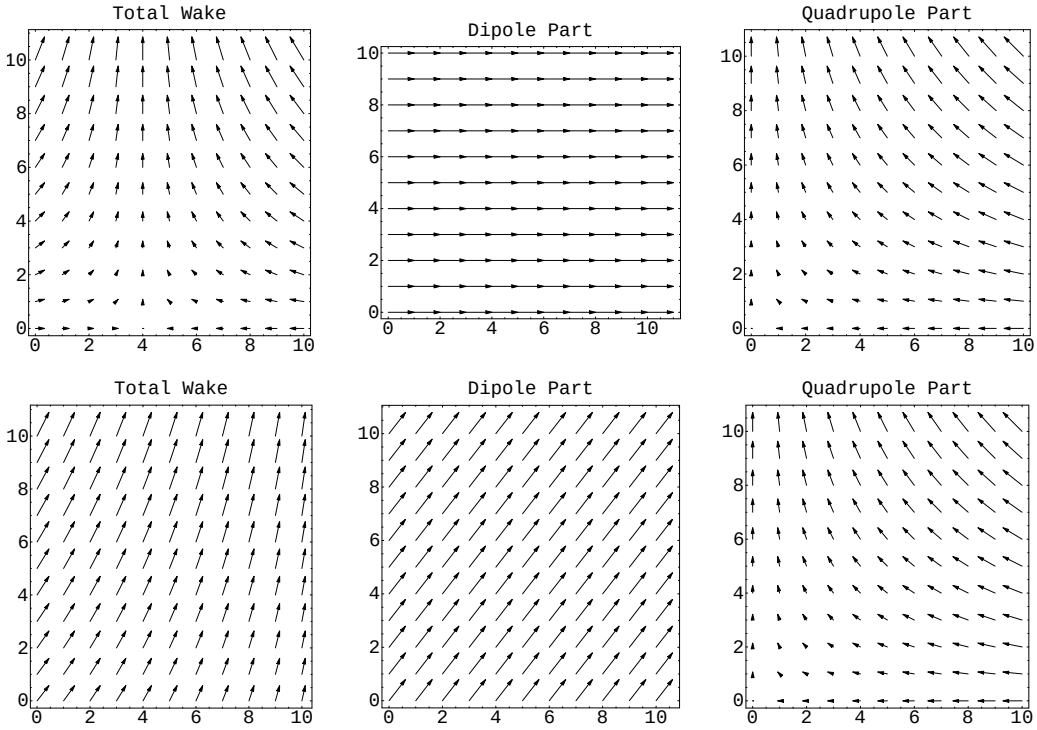

Figure 2.1: *Dipolar and quadrupolar wake components describe very well the generalized wakes in asymmetric structures.*

Chapter 3

Simulation Models & Techniques

Simulations are a valuable tool to study collective effects. In this chapter the concepts and numerical techniques of multi-bunch and/or multi-turn collective effects simulation will be presented. Multi-bunch effects become especially interesting for machines such as LHC, while single-bunch effects had already been treated for LEP [4, 29, 43, 34, 42].

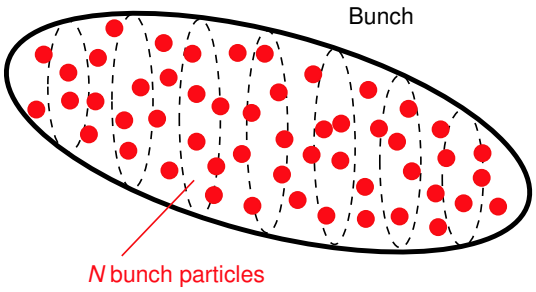

Figure 3.1: *Collection of Particles*

We start from a linear, single-particle dynamics model. This usually implies only the dynamics of the particle according to the optical elements (dipole, quadrupole) in the machine. The expansion to a collection of particles (ie. to a bunch) immediately requires the description of the particle-particle interaction inside the collection as well. However, direct space-charge forces become negligible for high energy machines, hence we do not include them here. But the particle interaction with its surrounding (eg. the vacuum chamber) is important. The electromagnetic fields of the moving particle induce currents in the surrounding structure, which themselves induce fields (called **wake fields**) that can act back on the following particles. The effects induced by wake fields are called **collective effects**, as they are associated with a collection of particles. If the fields induced by the head of the bunch act back on succeeding parts of the bunch, one talks about *single-bunch* effects. Imagine the induced fields decay slowly enough to affect the motion of the next bunch or bunches as well. This is called *multi-bunch* effect. If both the field decay is slow and the ring revolution frequency is high, wake fields can accumulate over several turns, hence we speak about *multi-turn* effects.

The study of collective effects is an addition to beam optics in the sense that the optics must be already available and the effects due to the beam interaction with its surrounding are superimposed. In principle this sounds simple: Take a set of

particles, track them through the machine according to the optics and compute the wake fields which give the forces that act back on this charged particle beam. But the straightforward implementation is computationally simply not possible as will be shown in the next section. However, also the motion of the original set of particles will be affected, which complicates the situation.

3.1 Macro-Particle Simulations in Time Domain

Given the dimension of an accelerator and its numerous different structure elements, it is easy to see that it is computationally not practicable to describe every piece of it in detail. In addition, to follow the motion of each particle in a beam (up to 10^{14}) is computationally impossible even with the most powerful computers available today. Therefore simplifications must be made in order to fit the actual situation into a mathematical model that can be handled by the simulation.

Just to get a feeling for the orders of magnitude imvolved, let us start with an example: Imagine you want to simulate the "real"LHC with all its 10^{14} particles in total. Let us say we want to keep track of their motion over 10^5 turns (which is not much, in LHC it corresponds to 10 seconds) and assume that the motion of a single particle over one turn could be calculated in 100 CPU cycles. At least at this stage it has to be pointed out that these are very optimistic numbers and the example should not be taken too seriously; in particular the number of cycles needed for this step can be much bigger. But let's proceed:

$$10^{14} \text{ particles} \cdot 10^5 \text{ turns} \cdot 10^2 \text{ cycles} = 10^{21} \text{ CPU cycles},$$
$$10^{21} \text{ cycles}/10^9 \text{ (cycles on a 1 GHz CPU)} = 10^{12} \text{ sec} \approx 3 \cdot 10^4 \text{ years}$$

Thus it is necessary to (drastically) simplify the calculations, and fortunately this can be done.

The way out is to use a reduced number of particles, which is still capable of describing the internal degrees of freedom of a bunch or a beam. They are often called *macro-particles*. It has been shown [5, 34] that in general a set of $10^4 - 10^5$ macro-particles is sufficient to describe a bunch adequately.

Given the parameters of LHC (see also Chap. 6), with over 2800 bunches, we would still end up with 10^{7-8} macro-particles, which is still above (or at least at the edge) of what is presently computationally possible. Therefore further simplifications have been made in order to save CPU time. Namely, as will be shown later (see Sec. 3.2 and 3.5), only the dipole motion of the bunches will be taken into account in the long-range regime. Only the barycenter of the bunches is simulated and accordingly we need only a single *super-particle* to describe one bunch.

As mentioned before, in a multi-particle simulation we cannot calculate the interaction of each (macro)-particle with every structure element in the accelerator. Fortunately the whole beam optics can be represented by maps, which can often be simplified to linear transfer matrices. Then the tracking of the particles through all optical elements of the machine is described by one or a few matrix multiplications. This is why collective effects simulations need existing beam optics data for a particular machine.

3.2 Approximations & Simplifications

In general there are two primary approaches to calculate collective effects:

Frequency domain calculations are done in terms of impedances and are in principle (numerical) solutions to eigenvalue problems. Hence only systems which have already relaxed to a certain dynamical equillibrium can be treated. Simulation of transient effects is limited to growth/decay. This approach is best adapted to analytical studies of simplified situations [35].

Time domain methods in general are used in macro-particle tracking codes. Usually one macro-particle describes 10^{6-8} real particles. The equations of motion are derived from classical mechanics taking into account the relativistic factors. "Tracking" means following the particle trajectory around the machine for several turns. The optics is described by a linear transfer matrix (Courant-Snyder parameters) or a non-linear map, of which both transport initial into final phase space points for one turn or a fraction of it. The Lorentz force due to the wake fields excited by the particles themselves influences their motion and collective behavior and needs to taken into account.

For the sake of completeness we also mention the Vlasov equation, that describes the collective behavior of a multiparticle system under the influence of electromagnetic forces as a differential equation of a continuous distribution function in phase space. In principle this can be used to simulate the evolution of the particle distribution. The emphasis should be put on "in principle", as exploiting the mathematics involved is very complicated. Related information can be found in [15, 36, 27, 28, 22].

In practice, frequency and time domain methods are applied profitably where they are of advantage. For the simulation studies of LHC the time domain approach was chosen because transient effects can easily be studied and the interplay of different impedances can be studied as well.

Having reduced the computational amount by the above-mentioned measures (macro-particles, see Sec. 3.1) we have to address the most important issue: The computation of the interaction of macro-particles with the wake fields. As in general the wake force $\vec{F}$ is a complicated function of position and time $\vec{F}(\vec{x}, t)$ all around the machine, it is computationally extremely challenging to calculate it and in several cases even impossible. Hence we again have to simplify and approximate to stay within feasible computation times; which can be achieved as follows.

A typical tracking code for collective effects beam simulation may be schematically represented as (see also for Fig. 3.2):

$$\vec{z}_n = \begin{pmatrix} x \\ x' \\ y \\ y' \\ \Delta t \\ \Delta E \end{pmatrix}_n \longrightarrow \vec{z}_{n+1} = \mathbf{M}\left(\vec{z}_n\right) \longrightarrow \vec{z}^{\,*}_{n+1} = \vec{z}_{n+1} + \delta\vec{z} \tag{3.1}$$

One starts with a set of phase space coordinates $\vec{z}$ for each macro-particle and tracks them over a certain distance in the machine according to the beam optics given as a linear or non-linear map $\mathbf{M}$. Particles coordinates are propagated from one turn to the next $\vec{z}_n \rightarrow \vec{z}_{n+1}$. At so-called *interaction points* (IP) the macro-particles experience a *kick* $\delta\vec{z}$, which affects their momentum but not their position. The strength of the kick is in general given by the wake field at that particular position, but in practice the kick is computed from the wake potential, which is already an integrated quantity over a certain distance, in most cases over the particular structure of concern or even the whole circumference. Hence we speak of the **lumped impedance approximation** as the effect of the impedance (wake field) is concentrated and applied in a location of zero length.

This practice is comprehensible for impedances such as cavities or cavity-like elements as they are usually of very limited length and the (ultra-) relativistic particle motion is not significantly disturbed during the passage of such an impedance. But for impedances due to space charge and wall resistivity, this is by no means a priori logical and has to be shown to be applicable. This has been done by Thompson and Ruth [38, Appendix.A].

Despite the variety of simulation codes, if it comes to computing the collective effects all codes are reduced to the same common problem: The wake fields must first be computed in order to get the kick that the particles experience. The kick is the change in energy or transverse momentum and is caused by the Lorentz force due to the wake fields. The concept of wake potential and wake function (see Sec. 2.3) simplifies this task enormously, but the computation of long-range wake potentials remains challenging and also potentially inaccurate.

In the following we will demonstrate how long-range wake field kicks have been treated and justify the simplifications and approximations pursued.

3.2.1 Rigid Dipole Mode Approximation

We will deploy and justify two major simplifications to facilitate the computation of wake field kicks, namely the

Wake Function Approximation; where we use the wake function instead of the wake potential, neglecting the influence of the individual bunch distribution on the wake fields, and the

Rigid Bunch Approximation; where we will represent the bunch by only a single macro-particle, hence only dipole mode effects can be described.

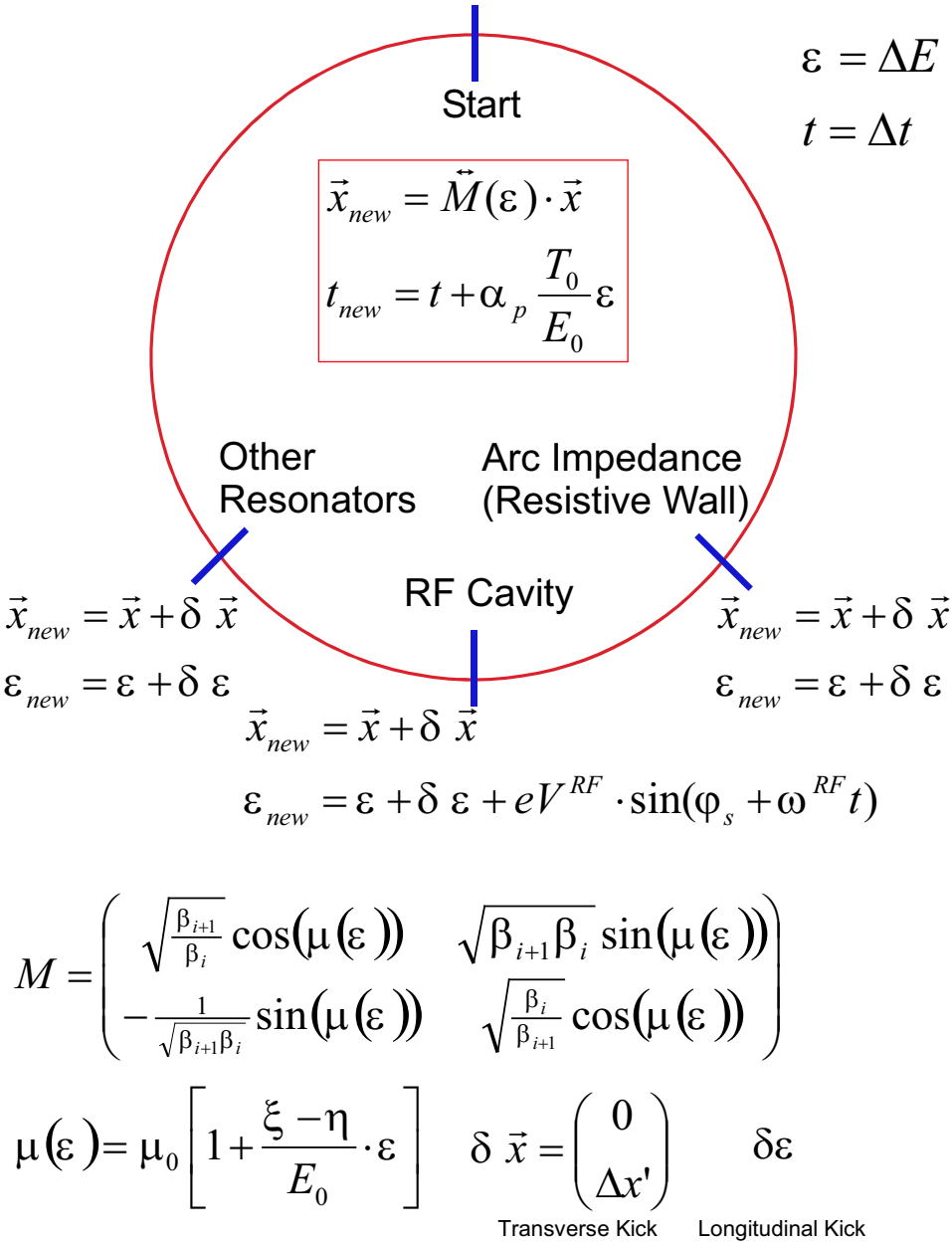

Figure 3.2: *Schematic representation of a typical macro-particle tracking code in time-domain. Refer also to Chap. 2 for basics on the equations of motion. Transverse phase space coordinates $\vec{x} = (x, x')$ are propagated from one IP to the next through the transfer matrix $\vec{M}(\varepsilon)$, where ε and t are the energy and time deviation from the synchronous particle. T_0 is the revolution time, E_0 is the synchronous particle energy, α_c and η are the momentum compaction and slip factor, μ is the phase advance between IPs and $\mu(\varepsilon)$ is the phase advance taking into account chromaticity ξ.*

Both simplifications are somewhat connected to each other. Using the rigid bunch approximation naturally results in the wake function approximation. On the other hand, using the wake function approximation, even for bunches with a certain spatial charge distribution, results in the same effect as using rigid bunches.

The total wake field in axially symmetric structures can be expressed as a sum over the wake fields of the multipole components of the exciting charge distribution. In general, higher multipole components have a weaker effect, thus only the $m = 0$ (rigid dipole) mode in longitudinal and the $m = 1$ (quadrupole) mode in transverse plane play a dominant role and are the only wake fields that will usually be included.

If the source of the wake fields consists of a charge distribution, one has to compute the wake potential as the convolution of the longitudinal charge distribution with the wake function. This means, that also bunch shape oscillations will influence the wake potential.

In the short-range regime ($\tau \approx \sigma_\tau$, i.e. inside the bunch) efficient use of precalculated waketables can be made in oder to compute the wake potential of an arbitrary bunch distribution [34]. The constraints of computer storage space and memory speed make this approach inapplicable for the long-range regime ($\tau \gg \sigma_\tau$) where we are interested in the effect of the wake fields excited by one bunch on the succeeding ones or even on itself in succeeding turns.

In the following we will assume the long-range regime, i.e.

$$z \gg \sigma_z \quad \text{or} \quad \tau \gg \sigma_\tau, \tag{3.2}$$

where distances z (in units of length) or τ (in units of time) between source and witness particles are assumed to be much larger than the typical rms bunch length σ_z (σ_τ), thus we are looking at wake fields outside or even far away from the exciting bunch.

Consider looking at a bunch with whatever bunch shape oscillations from some distance. Depending on the distance the bunch will appear more and more like a point-like object, without any shape at all. The only motion we will be able to detect is a dipole motion of the point-like object. Hence, in the long-range regime we will consider the bunch to be rigid and replace it by its barycenter that will be executing only dipole oscillations. As a consequence, we approximate the wake potential by the wake function, which is the wake potential of a point charge,

$$W_{pot}(\tau) \approx W(\tau). \tag{3.3}$$

wake function approximation

In mathematical terms, the wake function approximation reads as

$$W^{\parallel}_{pot}(\tau) = \int_0^\infty dt\, W_\parallel(t)\, \lambda(\tau - t) \qquad \approx W_\parallel(\tau) \text{ for } \tau \gg \sigma_t, \tag{3.4}$$

$$W^{\perp}_{pot}(\tau) = \frac{1}{\bar{\xi}} \int_0^\infty dt\, W_\perp(t)\, \xi(\tau - t)\, \lambda(\tau - t) \qquad \approx W_\perp(\tau) \text{ for } \tau \gg \sigma_t, \tag{3.5}$$

where $\lambda(t)$ is the (longitudinal) line density, $\xi(t)$ describes the varying and $\bar{\xi}$ is the average displacement. This approximation can be understood by physical reasoning

in the following way: For large times $\tau \gg \sigma_t$ the exciting bunch resembles more and more a delta-excitation in relation to the time scale, which consequently leads to the wake function. A mathematical motivation of this circumstance, which is far from being a proof follows along the following lines. The integration interval for the wake potential

$$W_{pot} = \int_{-\infty}^{\tau} dt\, W(\tau - t)\, \lambda(t) \tag{3.6}$$

can be reduced to the interval of total bunch length $t \in [-t_\sigma, t_\sigma]$, hence to the time range where $\lambda(t) \neq 0$. Under the assumption $\tau \gg t_\sigma$ and $\tau - t \approx \tau$ we can write

$$\int_{-t_\sigma}^{t_\sigma} dt\, W(\tau - t)\, \lambda(t) \approx \int_{-t_\sigma}^{t_\sigma} dt\, W(\tau)\, \lambda(t) \tag{3.7}$$

The exact condition for this approximation is that the wake function $W(t)$ varies little *at large distances* from the source. This is always the case due to damping of the wake by finite resistivity, which is present in reality. Applying this approximation we finally get

$$\int_{-t_\sigma}^{t_\sigma} dt\, W(\tau)\, \lambda(t) = W(\tau) \int_{t_1}^{t_2} dt\, \lambda(t) = W(\tau) \cdot q, \tag{3.8}$$

where $q = \int_{t_1}^{t_2} dt\, \lambda(t)$ is the total charge of the bunch.

The replacement of the wake potential by the wake function thus depends on the specific behavior of the wake at large distance. Fortunately the resistive wall wake function is of the slow-varying kind, and hence there the approximation is correct. However, for high-Q resonators with long memory, the time required for the wake function to decay to small enough amplitude may become rather large.

To simulate bunch shape oscillations one has to use a number of macro-particles that is sufficient to represent the degrees of freedom associated with the bunch shape mode (head-tail mode). The code developed is based on previous programs dedicated to single bunch effects [42, 34], where the representation of a single bunch by several hundreds or thousands of macro-particles was already available.

However, as only dipolar motion is simulated in the long-range regime all the other bunches are represented by only one macro-particle each. We call the representation of a bunch by only on macro-particle (i.e. modelling the motion of the barycenter only) **rigid bunch approximation**.

As will become apparent in the following sections both approximations, the *wake function* and the *rigid bunch* approximation are limited but justified under certain conditions.

3.2.2 Long-Range Effect of Higher Order Modes

In an accelerating cavity the fundamental mode is used for acceleration, but there are also Higher Order Modes (HOM), that are always present and must be damped in cases where they would deteriorate the beam quality. Those modes are not only

driven by the powering klystron itself but can also be driven by the beam. It has been found a long time ago, that wake fields due to HOMs can be well described by the resonator model, in the case of HOMs by a narrow band (high-Q) resonator.

In the Resonator Model a resonance is described by a parallel RLC-circuit. The corresponding longitudinal and transverse wake functions are given by

$$W_{\parallel}(t) = \mathrm{Re}\left[\frac{\omega_1 R}{Q'} \cdot \exp(j\ \omega_1 t)\right], \tag{3.9}$$

$$W_{\perp}(t) = \mathrm{Im}\left[\frac{\omega_r R_{\perp}}{Q'} \cdot \exp(j\ \omega_1 t)\right], \tag{3.10}$$

where R is the shunt impedance, Q_r the quality factor and ω_r the resonant frequency. The reduced quality factor ${Q_r}' = \sqrt{Q_r^2 - 1/4}$ and the complex frequencies $\omega_{1,2} = (\omega_r/Q_r)(j\ /2 \pm {Q_r}')$ are introduced as well [48].

Any element in the beam pipe that represents a structural cross-section variation, such as cavities, bellows, pick-ups, vacuum pumping ports and collimators will lead to geometric wakes, which in general again can be well described by the resonator model. As a natural consequence this section will thus not only be valid for HOMs, but for any wakes that can be described by a resonator model.

In the long-range regime ($\tau \gg \sigma_\tau$), only high-Q resonators are considered. Since low-Q resonator are strongly damped, they have no effect in the long-range regime. Again with an eye on the computation time, we will apply some simplifications. As the resonator wake function summation is very easy to do, we will use the wake function approximation. This seems to be a very crude approximation, especially when the corresponding wavelength λ_r of the resonators is smaller or in the order of the bunch length σ_z (in LHC this is the case for frequencies above 2 GHz). Then the wake function is strongly oscillating within the bunch, causing bunch shape oscillations and does not meet the condition of being only slowly varying along the bunch. However, as we only simulate rigid dipole modes, this is still a good model because the wake function is exactly the average value of the wake potential in this case.

Frequency Variation

A more severe problem in the modelling of HOMs is the fact that we never know the resonance frequencies to infinite precision (see for Fig. 3.3). Even if we would be able to precisely specify them, it would not help as due to temperature and vacuum pressure changes, the frequencies tend to drift away or what is especially worrisome: New modes appear.

There are two straightforward approaches to tackle this problem: First, one can artificially widen the peak of the resonator $\Delta Q \rightarrow x \cdot \Delta Q, x > 1$ to make it effective over a larger range of frequencies. As this directly changes the impedance properties of the resonator this approach has been discarded. The second possibility is to slowly vary the resonant frequency ω_r of the resonator over a certain range. As this refers more to reality, this approach is favoured.

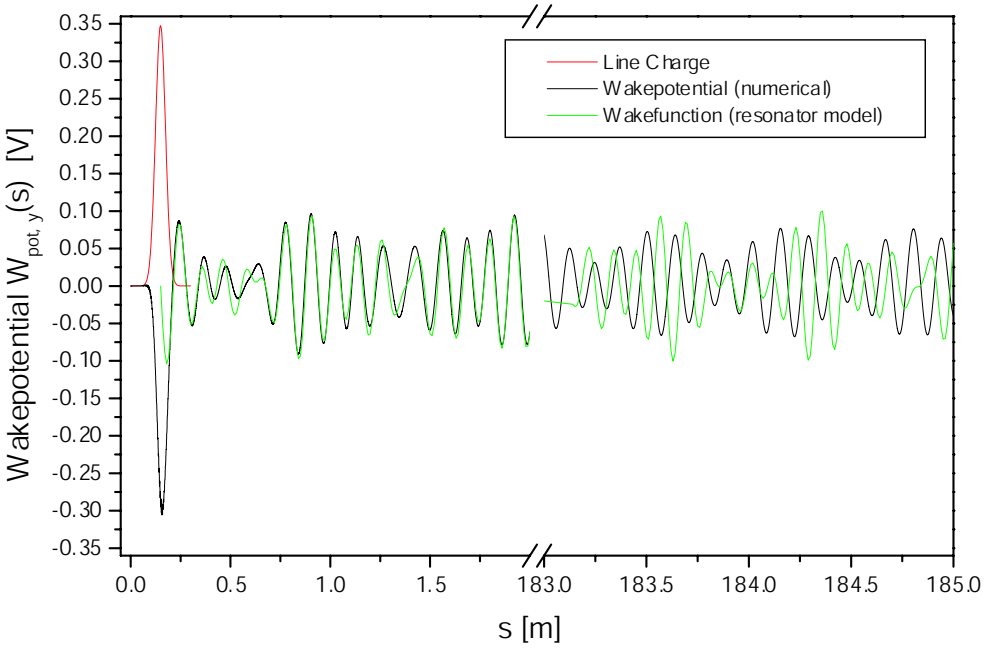

Figure 3.3: *Transverse wake potential of a gaussian longitudinal charge density in a LHC collimator computed by* GdfidL *as compared to its wake function approximation by the resonator model.*

Resonator Approximation

We would prefer to compute the wake potential with a mesh code (e.g. MAFIA, GdfidL, ABCI), which was done for TRISIM and TRISIM3D. However, it takes hours or days to compute the wake fields for distances of several meters and it is quite impossible to compute the wake over 27 km, the circumference of LHC. Also the computed wakes become more and more inaccurate the larger the distance behind the source. Finally it would not be possible to store these data efficiently for later use. Hence geometric wakes are simplified to narrow band resonators. For HOMs the resonator model is a very good approximation.

3.2.3 Long-Range Effect of the Resistive Wall

In general, all elements in an accelerator are made of lossy materials, i.e. they have a finite conductivity σ_c or resistivity ρ_c. Most parts of the machine will be designed to have a low impedance, they are made of good conductors such as copper, aluminium or stainless steel. To reduce the impedance of badly conducting materials, they might even be copper-coated. Whatever measures are taken, a resistive component will remain in the accelerator.

The impedance of an axially symmetric resistive wall surrounding the beam is

given by [24],

$$Z^{\perp}_{m=1}(\omega) = (1 + j\ \mathrm{sgn}\,\omega)\ \frac{cL}{\pi b^3}\sqrt{\frac{\mu_o\mu_r}{2\,\sigma_c}}\cdot\frac{\sqrt{|\omega|}}{\omega}. \tag{3.11}$$

L is the length of the structure and the impedance scales with the inverse cube of the beam pipe radius b. Therefore not only the conductivity σ_c of the wall material is important but also its distance to the beam.

The corresponding wake function

$$W^{\perp}_{m=1}(t > 0) = \frac{cL}{\pi^{3/2} b^3}\sqrt{\frac{\mu_o\mu_r}{\sigma_c}}\cdot\frac{1}{\sqrt{|t|}} \tag{3.12}$$

decays slowly as $1/\sqrt{t}$, hence in a multi-bunch machine the individual wake contributions can accumulate.

In LHC several conditions make the resistive wall effect especially important: The beam pipe radius is small $b \simeq 1\,\mathrm{cm}$ and the machine will be filled with many closely spaced bunches. Furthermore collimators made of graphite will be installed with a minimum half-gap opening of 1.3 mm. This makes the transverse impedance of LHC dominated by the resistive wall effect.

3.3 The Wake Summation Problem

To study the stability of a particle beam, its motion is analyzed under the influence of wake fields. Hence, in general, the interest lies in the impact of the accumulated wake forces on the beam motion.

The transverse wake potential $\int_{-L/2}^{L/2}\vec{F}_{\perp}ds$ experienced by a test charge e travelling at a time distance t behind the beam with an $m = 1$ dipole moment is given by

$$-e\,q\,\langle x\rangle\,W^{\perp}_{m=1}(t),$$

where q is the charge of the exciting beam and $\langle x\rangle$ its displacement ($q\langle x\rangle$ is the dipole moment), see also Chao [12, p.63]. $W^{\perp}_{m=1}$ is the transverse dipole wake function. Consider a single one-particle bunch executing transverse betatron oscillations. At successive turns with revolution time $\tau_{\mathrm{rev.}}$ the bunch will see its own wake fields, thus its motion at turn n will be perturbed by the wake force which is proportional to

$$-e\sum_{k=0}^{n-1} q\,\langle x\rangle_k\,W^{\perp}_{m=1}\left(t = (n-k)\,\tau_{\mathrm{rev.}}\right). \tag{3.13}$$

Note that the transverse wake experienced by the bunch at turn n is weighted by its transverse offsets at all previous turns $\langle x\rangle_k$, with $k = 0, 1, 2, \ldots, n-1$. Hence the sum of wake field kicks has the following structure depending on the number of

turns n:

$$\begin{aligned}
\Delta x'_1 &\propto \langle x\rangle_0 \, W_1^{\perp}\left(1\,\tau_{\text{rev.}}\right) \\
\Delta x'_2 &\propto \langle x\rangle_0 \, W_1^{\perp}\left(2\,\tau_{\text{rev.}}\right) + \langle x\rangle_1 \, W_1^{\perp}\left(1\,\tau_{\text{rev.}}\right) \\
&\vdots \\
\Delta x'_n &\propto \langle x\rangle_0 \, W_1^{\perp}\left(n\,\tau_{\text{rev.}}\right) + \langle x\rangle_1 \, W_1^{\perp}\left((n-1)\,\tau_{\text{rev.}}\right) + \cdots + \langle x\rangle_{n-1} \, W_1^{\perp}\left(1\,\tau_{\text{rev.}}\right).
\end{aligned} \tag{3.14}$$

Note that the corresponding time in the wake function changes at each new turn

$$\langle x\rangle_0 \, W_1^{\perp}\left(\mathbf{1}\,\tau_{\text{rev.}}\right) \longrightarrow \langle x\rangle_0 \, W_1^{\perp}\left(\mathbf{2}\,\tau_{\text{rev.}}\right) \longrightarrow \cdots \longrightarrow \langle x\rangle_0 \, W_1^{\perp}\left(\mathbf{n}\,\tau_{\text{rev.}}\right).$$

The *resonator* wake function (with resonant frequency ω_r) has the comfortable mathematical property that the step

$$W_1^{\perp,Res.}\left(\mathbf{n}\,\tau_{\text{rev.}}\right) \xrightarrow{\exp(j\omega_r\tau_{\text{rev.}})} W_1^{\perp,Res.}\left((\mathbf{n}+\mathbf{1})\,\tau_{\text{rev.}}\right)$$

is a simple multiplication with a complex exponential (phasor). This will be used and shown in Sec. 3.4.

For the resistive wall impedance such a simple mathematical operation is not known, therefore another approach has to be chosen. In Sec. 3.5 we will show the FFT convolution algorithm for the resistive wall wake function, and any impedance that can be cast into the same framework can be treated as well.

3.4 Summation of Long-Range Resonator Wake Fields

The resonator model is often the first choice to approximate or describe impedances because of its mathematical simplicity. Especially the resonator wake function can represented as a vector in the complex plane, which is called a phasor. Time evolution and summation reduce to a simple multiplication with an complex exponential and a simple vector addition, see also Fig. 3.4.

The Phasor approach for summation of wake function contributions can be summarized as follows:

Longitudinal Resonator Wake Function

$$\boxed{\begin{aligned}
W_{\parallel}(t) &= \operatorname{Re}\left[\widetilde{W}_{\parallel}(t)\right] = \operatorname{Re}\left[\frac{R}{Q'}\,\omega_1 \cdot \exp(j\,\omega_1 t)\right] && \text{Phasor} \\
\widetilde{W}_{\parallel}(t+\Delta t) &= \widetilde{W}_{\parallel}(t) \cdot \exp(j\,\omega_1 \Delta t) && \text{Time Evolution} \\
\widetilde{W}_{\parallel}(t_1) + \widetilde{W}_{\parallel}(t_2) &= \frac{R}{Q'}\,\omega_1 \left(\underbrace{\exp(j\,\omega_1 t_1) + \exp(j\,\omega_1 t_2)}_{\text{vector addition}}\right) && \text{Summation}
\end{aligned}} \tag{3.15}$$

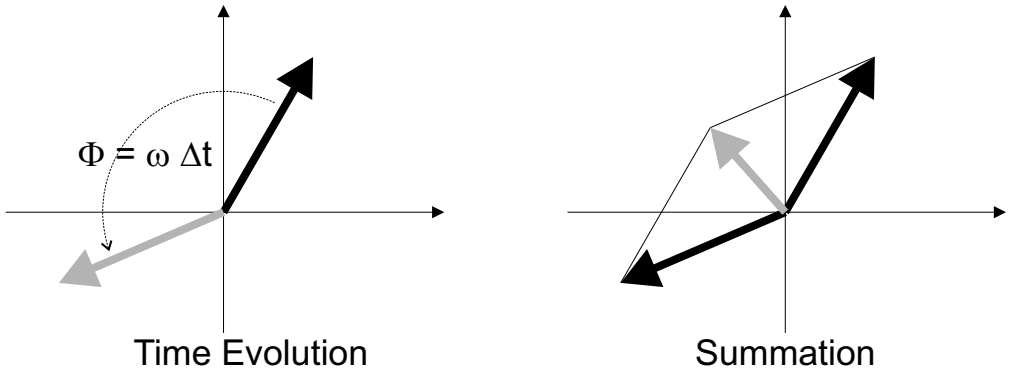

Figure 3.4: *Summation and time evolution in the Phasor description.*

Transverse Resonator Wake Function

$$\begin{aligned} W_\perp(t) &= \operatorname{Im}\left[\widetilde{W}_\perp(t)\right] = \operatorname{Im}\left[\frac{\omega_r R}{Q'}\,\exp(j\,\omega_1 t)\right] \\ &\text{Phasor} \\ \widetilde{W}_\perp(t+\Delta t) &= \widetilde{W}_\perp(t)\cdot\exp(j\,\omega_1\Delta t) \\ &\text{Time Evolution} \\ \widetilde{W}_\perp(t_1)+\widetilde{W}_\perp(t_2) &= \frac{\omega_r R}{Q'}\left(\underbrace{\exp(j\,\omega_1 t_1)+\exp(j\,\omega_1 t_2)}_{\text{vector addition}}\right) \\ &\text{Summation} \end{aligned} \tag{3.16}$$

3.5 Summation of Long-Range Resistive Wall Wake Fields

For resonator impedances, the phasor approach is well known and can be used to efficiently calculate the wake at each time step. Unfortunately such a nice mathematical tool does not exist for impedances like the resistive wall, where the $1/\sqrt{t}$-dependence (t being the time parameter in the wake function) does not allow for an easy summation. However, recognizing that the sum to be evaluated can be cast into the framework of the discrete convolution theorem, directs us to the FFT convolution algorithm, which reduces the computation time enormously.

In the following the necessary derivations will be given and the algorithm for the summation of the resistive-wall wake contributions will be explained. It should be noted, however, that this wake summation scheme is not restricted to the resistive wall impedance at all, it can be applied to any other impedance that can be cast into the required framework.

Various references [12, 16] show the derivation of the classical, transverse, resistive (thick) wall impedance in round pipes as well as the wake function. The impedance of the lowest dipole mode $m = 1$ (higher modes can be found in Ref. [13, p.204])

reads as:

$$\begin{aligned} Z^{\perp}_{m=1}(\omega) &= (1 + j\ \mathrm{sgn}\,\omega)\ \frac{cL}{\pi b^3}\sqrt{\frac{\mu_o\mu_r}{2\,\sigma_c}}\cdot\frac{\sqrt{|\omega|}}{\omega} \\ &= (\mathrm{sgn}\,\omega + j)\ \frac{\mu_r\, Z_0\, L\,\delta_0}{2\,\pi\, b^3}\cdot\sqrt{\frac{\omega_0}{|\omega|}} \end{aligned} \tag{3.17}$$

In the above formula c denotes the speed of light, L indicates the length over which the impedance is defined (e.g. $L = 2\pi R =$ the circumference), b is the vacuum chamber radius, μ_0 and μ_r denote the free-space and relative permeability, respectively, and finally σ_c designates the conductivity of the vacuum chamber wall. In the second expression the quantities $\omega_0 = 2\pi/\tau_{rev}$, the angular revolution frequency, and $Z_0 = c\,\mu_0$, the free space impedance, were used. Consequently, δ_0 denotes the skin depth at the angular revolution frequency. All expressions are given in *MKSA* units.

Applying the inverse Fourier transformation to Eq. (3.17) leads to the classical transverse wake function for a thick wall:

$$\begin{aligned} W^{\perp}_{m=1}(t > 0) &= \frac{cL}{\pi^{3/2} b^3}\sqrt{\frac{\mu_o\mu_r}{\sigma_c}}\cdot\frac{1}{\sqrt{|t|}} \\ &= \frac{\mu_r\, Z_0\, L\,\delta_0}{\pi\, b^3\,\tau_{rev}}\cdot\sqrt{\frac{\tau_{rev}}{|t|}} \end{aligned} \tag{3.18}$$

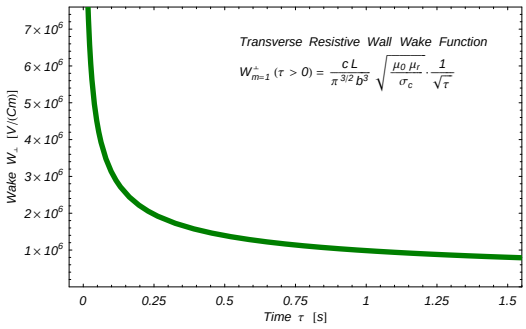

Figure 3.5: *Qualitative behavior of the transverse resistive wall wake function*

Due to the slow decay of the resistive wall wake fields ($1/\sqrt{t}$), a bunch can see its own wake created at previous turns. Furthermore, if several bunches are involved, each of them sees not only itself but all the others as well. Thus the problem is to sum up all the wakes over previous turns and bunches.

We assume in the following that the action of the resistive wall can be concentrated in one single point of zero longitudinal extent ("interaction point = IP"), although in reality the resistivity is distributed around the machine circumference. This refers to the **lumped impedance approximation**, which was shown to be valid in Ref. [38, Appendix.A]. Furthermore mind that the summation is taken to be that of wake functions of a δ-function bunch and not of wake potentials according to the longitudinal charge distribution (**wake function approximation**). For the slowly varying resistive wall wake field the approximation of point-like bunches in the long-range regime is intuitively plausible but this approximation might not be applicable to other impedances.

Equation (3.13) is already anticipating some assumptions. In the most general case the resistive wall kick at the n-th turn, in the case of a single bunch seeing its

own fields reads as

$$\Delta x'_n = const. \cdot \sum_{k=0}^{n-1} \frac{\langle x \rangle_k}{\sqrt{t_{nk}}}, \tag{3.19}$$

where constants have been collected and $\langle x \rangle_k$ is the bunch's displacement at revolution k and t_{nk} is the time elapsed between the passage of the bunch at turn k and turn n. Generally the $\langle x \rangle_k$ an the t_{nk} are found in the course of the simulation and can not be precalculated. As the sum (3.19) has to be computed from scratch at each turn this leads easily to sums that need excessive computation time as well as memory. Therefore it is necessary to find other ways to compute such sums faster.

The first ansatz is to define the t_{nk} more precisely

$$t_{nk} = (n-k) \cdot \tau_{rev.} + \Delta t_k + \Delta t_n, \tag{3.20}$$

where $\tau_{rev.}$ is the revolution frequency, Δt_k is the time offset from the synchronous particle at turn k and Δt_n is the time offset at the current turn. Assuming that these time offsets are negligibly small with respect to the revolution time, one can omit them and recover the simpler equation (3.13):

$$\Delta x'_n = const. \cdot \sum_{k=0}^{n-1} \frac{\langle x \rangle_k}{\sqrt{(n-k) \cdot \tau_{rev.}}} \tag{3.21}$$

To disregard the offsets from the synchronous particle is a good approximation; e.g. over the length of an LHC type bucket, the resistive-wall wake fields change by less than 5%.

The case of several bunches N_b present in the machine is slightly more complex. The kick on bunch $j \in [0, N_b - 1]$ at turn n is given by:

$$\begin{aligned} \Delta x'^j_n = & \; const. \cdot \sum_{k=0}^{n-1} \sum_{i=0}^{N_b-1} \frac{\langle x \rangle_k^i}{\sqrt{(n-k) \cdot \tau_{rev.} + (j-i) \cdot \tau_{buc.}}} \Bigg\} \text{previous turns} \\ & + const. \cdot \sum_{i=0}^{j-1} \frac{\langle x \rangle_n^i}{\sqrt{(j-i) \cdot \tau_{buc.}}} \Bigg\} \text{current turn} \end{aligned} \tag{3.22}$$

Here we assumed that every bucket is filled, but uneven bunch patterns can be handled easily by setting the $\langle x \rangle^i$ to zero accordingly (i.e. by using a 'mask'). The superscript in $\langle x \rangle_k^i$ denotes the bunch number while the subscript denotes the turn number. Mind that the bunches are numbered from 0 to $N_b - 1$. $\tau_{buc.}$ is the bucket spacing in time units.

In practice we will only sum a finite number of turns n_{mem} because the fields penetrate the vacuum chamber proper after some diffusion time [11, Eq.(13)]. Hence we keep a memory of n_{mem} turns and the summation is truncated for $k < n - n_{mem}$:

$$\begin{aligned} \Delta x'^j_n = & \; const. \cdot \sum_{k=n-n_{\mathrm{mem}}}^{n-1} \sum_{i=0}^{N_b-1} \frac{\langle x \rangle_k^i}{\sqrt{(n-k) \cdot \tau_{rev.} + (j-i) \cdot \tau_{buc.}}} \\ & + const. \cdot \sum_{i=0}^{j-1} \frac{\langle x \rangle_n^i}{\sqrt{(j-i) \cdot \tau_{buc.}}} \end{aligned} \tag{3.23}$$

The outermost sum in Eq. (3.23) is now added up to a constant number of turns, which depending on the penetration time of the fields can be in the order of a few up to 100 turns. This is feasible for modern computers if the inner sum can be calculated in a fast manner, hence we concentrate on this innermost sum in the following. Furthermore for the sake of brevity and clarity we start explaining the algorithms for the sum (3.21) which has the same structure as the last term in (3.23). We will also show that the innermost sum of the first term in (3.23) can be treated alike using slight modifications.

So far the wake summation problem has been stated in a mathematical form in equation (3.23). We will show in the next section how to speed up the computations of these sums by FFT convolution.

3.5.1 A Shortcut by the Long Way Around – FFT Convolution

In the following we will exploit the fact, that *multiplication* in the frequency domain corresponds to *convolution* in the time domain. This is the quintessence of the convolution theorem which says that the Fourier transform of the convolution of two functions is equal to the product of their individual Fourier transforms.

The problem at hand is transformed into the frequency domain using the discrete Fourier transform (DFT), there the summation reduces to a multiplication, then it is transformed back into the time domain using the inverse DFT. The time needed for all this operations ('the long way around') is shorter than the direct evaluation of the convolution because of the speed of the Fast Fourier transform (FFT).

We come back to the problem of summing up the wakes due to the resistive wall for a single bunch. The kick at the n-th turn is given by

$$\Delta x'_n = const. \cdot \sum_{k=0}^{n-1} \frac{\langle x \rangle_k}{\sqrt{(n-k)\cdot\tau_{rev.}}} = const. \cdot \sum_{k=0}^{n-1} g(k)\cdot f(n-k)\ , \tag{3.24}$$

where $\langle x \rangle_k$ is the (vertical or horizontal) bunch offset at turn k and the denominator gives the time delay between the current turn n and the turn k. The offsets can be seen as a function $g(k) \equiv \langle x \rangle_k$ and the rest can be interpreted as a function $f(n-k) \equiv const. \cdot \frac{1}{\sqrt{(n-k)\cdot\tau_{rev.}}}$.

Writing the sum in the before mentioned way, it can be cast into the framework of convolution theory. The discrete convolution for the functions g and f (the signal and response function respectively) is defined as (see also Sec. 3.6.2)

$$h(n) = g * f = \sum_{k=0}^{N-1} g(k)\, f(n-k) = \sum_{k=0}^{N-1} g_k\, f_{n-k}\ , \tag{3.25}$$

where g_i and f_i are two arrays of size $N(\geq n)$ holding the values $g(i)$ and $f(i)$. Correspondingly the output array h_i (with values $h(i)$) is also of length N.

The (circular) FFT convolution algorithm consists in finding the individual FFTs of g and f, their multiplication $H_j = G_j\, F_j$ and finally the inverse FFT of H,

$$h_n = (g*f)_n = \sum_{k=0}^{N-1} g_k\, f_{n-k} \quad \overset{FFT}{\underset{IFFT}{\Longleftrightarrow}} \quad G_j F_j = H_j. \tag{3.26}$$

By carrying out the multiplication and inverse Fourier transform we get an array h containing the following sums:

$$\begin{aligned}
h_0 &= g_0 f_0 + g_1 f_{-1} + g_2 f_{-2} + \cdots + g_{N-1} f_{-N+1} \\
h_1 &= \underline{g_0 f_1} + g_1 f_0 + g_2 f_{-1} + \cdots + g_{N-1} f_{-N+2} \\
h_2 &= \underline{g_0 f_2 + g_1 f_1} + g_2 f_0 + \cdots + g_{N-1} f_{-N+3} \\
&\vdots \\
h_n &= \underline{g_0 f_n + g_1 f_{n-1} + g_2 f_{n-2} + \cdots} + g_n f_0 + \cdots + g_{N-1} f_{-N+n+1} \\
&\vdots \\
h_{N-1} &= g_0 f_{N-1} + g_1 f_{N-2} + g_2 f_{N-3} + \cdots + g_{N-1} f_0
\end{aligned} \tag{3.27}$$

Each output h_i consists of an equal number of terms. The Fourier transform assumes that the functions g and f are periodic with period N. Therefore negative values of the index correspond to their positive periodic counterpart $f_{-i} = f_{N-i}$. The periodic placement of the samples produces periodic output affected by aliasing. This is also called the "wrap-around effect"; values of the signal or response functions far from the current index are taken into account as well due to the periodicity assumption, see also Fig.3.6. In our case, which is called *linear* convolution, aliasing is unwanted as indicated in the sums Eq. (3.27), wanted parts are underlined while unwanted parts are not. To transform the *circular* (periodic) convolution into a linear one, we see that the corresponding terms $g_k\, f_{n-k}$ have to vanish.

Aliasing does not occur if we append sequences of zeros to the input samples ('zero padding'). We can compute the linear convolution for n turns by choosing $N \geq 2n$ and setting all g_i and f_i to zero for $i > n$. This ensures that the corresponding terms $g_k\, f_{n-k} \equiv 0 \;\forall\; k \geq n$ vanish (the 'upper triangular matrix' in (3.27)) and we arrive at the correct sums h

$$\begin{aligned}
h_1 &= \frac{\langle x \rangle_0}{\sqrt{1 \cdot \tau_{rev.}}} \\
h_2 &= \frac{\langle x \rangle_0}{\sqrt{2 \cdot \tau_{rev.}}} + \frac{\langle x \rangle_1}{\sqrt{1 \cdot \tau_{rev.}}} \\
&\vdots \\
h_n &= \frac{\langle x \rangle_0}{\sqrt{n \cdot \tau_{rev.}}} + \frac{\langle x \rangle_0}{\sqrt{(n-1) \cdot \tau_{rev.}}} + \cdots + \frac{\langle x \rangle_{n-1}}{\sqrt{1 \cdot \tau_{rev.}}}.
\end{aligned} \tag{3.28}$$

Refer to Fig.3.7 and 3.8 for a schematic representation. Please note that we additionally had to set $f_0 \equiv 0$. This ensures that there is no immediate effect on the bunch itself. From another point of view it is simply the fact that the indices of our problem and the convolution are mismatched by one unit and setting $f_0 \equiv 0$ rectifies this situation. Furthermore it is necessary for the multi-bunch FFT convolution also, as will become apparent in section 3.5.2.

Specifically, if $g(k)$ is N_1 points long and $f(k)$ is N_2 points long, $g(k)$ may be *linearly* convolved with $f(k)$ as follows:

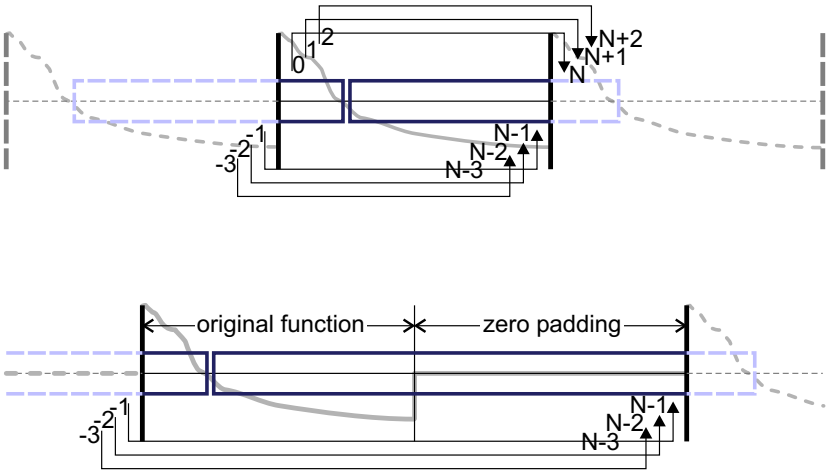

Figure 3.6: *Periodicity and the effect of zero padding: The function is assumed to be periodic, negative indices are wrapped around to the positive region and will therefore be erroneously used in the convolution. Zero padding breaks this effect by setting the "wrapped-around"part to zero. Especially, the convoluted part of the "original function"will be wrap-around-free while the corresponding zero padded part will be spoiled, which does not matter as it is not used. See also Fig.3.7 and 3.8.*

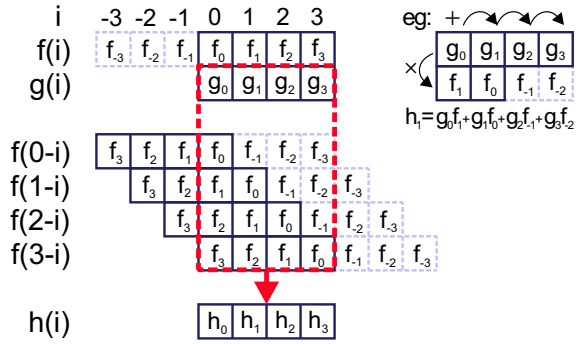

Figure 3.7: *Convolution visualized as suggested in [37]: g and f are the two functions to be convoluted. To find the output h_j, one computes the sum of products of overlapping samples g_i and f_{j-i}. This is shown as an separate example for h_1. Mind the periodic continuation of f that is introduced by the Fourier transform.*

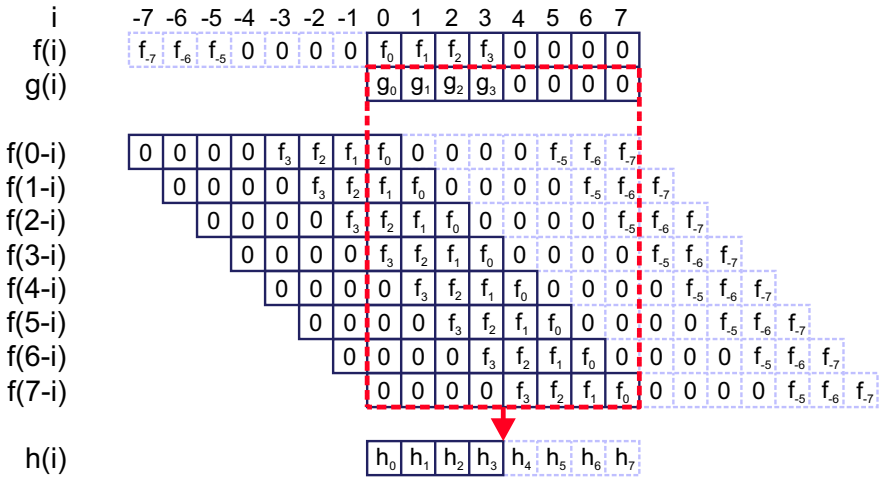

Figure 3.8: *Linear convolution realized by zero padding. The periodic continuation of f (introduced by the Fourier transform) is shifted into the extended part using the padding. This rectifies the sums such that they coincide with the sums in (3.28). Mind that $h_0, \ldots, h_3$ are wrap-around free while $h_4, \ldots, h_7$ are not.*

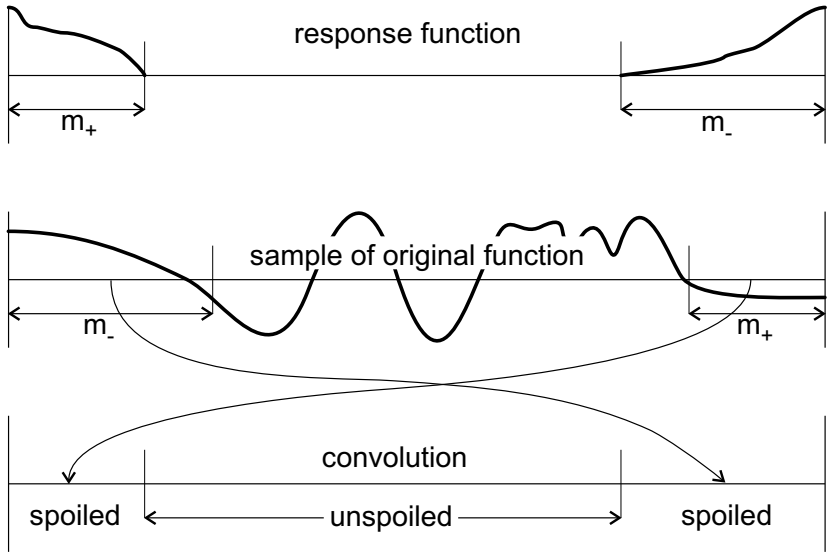

Figure 3.9: *The wrap-around effect as described in [32]: Not only must the response function wrap be viewed as cyclic, but so must the sampled original function. Therefore a portion at each end of the original function is erroneously wrapped around by convolution with the response function.*

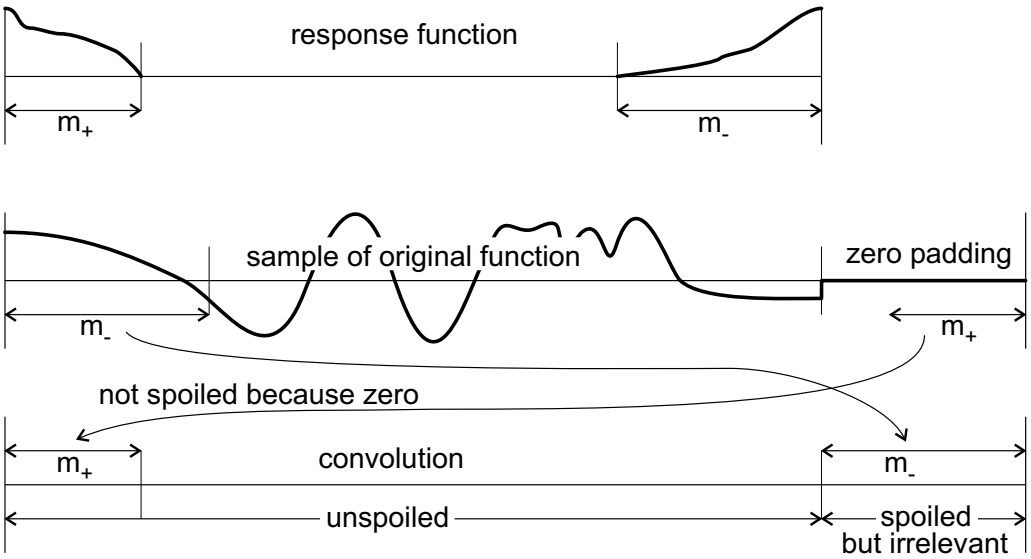

Figure 3.10: *Zero padding as solution to the wrap-around problem as described in [32]. The original function is extended by zero, serving a dual purpose: When the zeros wrap around, they do not disturb the true convolution; and while the original function wraps around onto the zero region, that region can be discarded.*

1. Pad the sequences $g(k)$ and $f(k)$ with zeros, so that they are of length $N \geq N_1 + N_2 - 1$.
2. Find the N-point DFTs of $g(k)$ and $f(k)$.
3. Multiply the DFTs to form the product $H(k) = G(k)F(k)$.
4. Find the inverse DFT of $H(k)$.

A note: The above described algorithm is called linear convolution using the DFT. Readers familiar with the topic might wonder why we do not use the Overlap-Add or Overlap-Save method to completely compute the double sum of (3.23) via the FFT convolution. The reason is very simple: The overlap method works if and only if the response function is of finite range. A wake function, the function f respectively, extends in principle to infinity or at least covers a very large finite range in time, hence the "overlap"would become infinite or very large as well, which makes these methods inapplicable.

The alert reader might further ask himself what we gained by this approach so far. Nothing, is the answer. In fact, the algorithm described was only the proof of principle, but is not meaningful for a single bunch: At each time step, i.e. at each turn n, we are only interested in the value h_n, but we also calculated the values $h_i, i = 1, \ldots, n-1$ and we do this at each turn. Hence an significant overhead is computed unnecessarily. *In general one should use the direct summation method for a single bunch.*

This changes as soon as more than one bunch is involved: Then the second term in (3.23) has to be computed only once at each turn and not N_b-times from scratch (which would scale as $\mathcal{O}(N_b^2/2+N_b/2)$). Also the inner sum in the first term of (3.23) has to be calculated only once per turn, whereas direct summation would result in N_b sums over N_b summands (thus scaling as $\mathcal{O}(N_b^2)$). How we can treat (3.23) is shown in the next section.

3.5.2 Multiple Bunches

Having shown the principle of the FFT method in the last section it can be used for the 'current turn'-part of sum (3.23). The sums

$$h_j = \Delta x'^j_n = const. \cdot \sum_{i=0}^{N_b-1} \frac{\langle x \rangle_n^i}{\sqrt{(j-i)\cdot\tau_{buc.}}} \tag{3.29}$$

at turn n can be computed via the FFT convolution as described in the last section. Applying zero padding results in the correct sums and thus we compute in ***one*** *convolution operation* the sum of kicks *for* ***each*** *bunch* $j = 0, \ldots, N_b - 1$.

The sum $\sum_{i=0}^{N_b-1} \frac{\langle x \rangle_k^i}{\sqrt{(n-k)\cdot\tau_{rev.}+(j-i)\cdot\tau_{buc.}}}$ from (3.23) for fixed n (current turn) and k (turn number) and any $j \in [0, N_b - 1]$ (bunch number) can be treated as well. The difference compared to the sums treated so far is the fact that these sums have a constant number of summands no matter what value of j, just like when no zero padding is used. But unlike this periodic convolution, no cyclic continuation of the values is desired but a linear one. Let us write down the sum more detailed to visualize what is meant by that. We express the revolution time $\tau_{rev.}$ as an integer multiple of the bucket spacing $\tau_{buc.}$ and rewrite the denominator to read

$$\underbrace{(n-k)}_{c} \cdot \underbrace{\tau_{rev.}}_{N_b\cdot\tau_{buc.}} + (j-i)\cdot\tau_{buc.} = (cN_b + j - i)\cdot\tau_{buc.}.$$

We get an expression that has the same structure for each bunch $j = 0, \ldots, N_b - 1$,

$$\begin{aligned}
&\sum_{i=0}^{N_b-1} \frac{\langle x \rangle_k^i}{\sqrt{(cN_b + j - i)\cdot\tau_b}} = \\
&= \frac{\langle x \rangle_k^0}{\sqrt{(cN_b + j)\cdot\tau_b}} + \frac{\langle x \rangle_k^1}{\sqrt{(cN_b + j - 1)\cdot\tau_b}} + \cdots + \frac{\langle x \rangle_k^{N_b-1}}{\sqrt{(cN_b + j - N_b + 1)\cdot\tau_b}} \qquad (3.30) \\
&= g_0 f(cN_b + j) + g_1 f(cN_b + j - 1) + \cdots + g_{N_b-1} f(cN_b + j - N_b + 1),
\end{aligned}$$

but it lacks the 'lower triangle matrix' layout as in (3.27). What is more important is the denominator f: Contrary to the one in (3.27) it is shifted by the amount cN_b and thus does not correspond to the wrapped-around values f_{-i}.

To render the correct sums via FFT convolution the algorithm has to be modified in the following sense. Before zero padding, the array f_i is extended to be twice as long

$$\text{size}f' = 2 \times \text{size}f = 2 \cdot N_b.$$

Let n be the current turn number and $k \in [1, n - n_{\text{mem}}]$ the turn number where we wish to sum the bunches within. Consequently $c = n - k = 1, 2, \ldots$ means one turn before, two turns before and so forth. The array f'^c for the corresponding operation should now be filled with values

$$f'^c_i = const. \cdot \frac{1}{\sqrt{((c-1)N_b + i) \cdot \tau_{buc.}}}, \qquad i = 0, \ldots, 2N_b - 1. \tag{3.31}$$

Hence, what we did is to start filling in values of one turn before the current one $(c-1)$. In principle this is the novelty in this approach. To actually see what is happening refer to Fig.3.11 for a visualization of this scheme.

The situation $n - k = 1$ is special as the denominator f'^1_0 would diverge. We have to set $f'^1_0 \equiv 0$, this ensures that the algorithm works correctly, as can also be deduced from Fig.3.11. We continue with the standard procedure for linear convolution:

- Zero padding of f (twice as long $= 2N_b$) and g ($3N_b$, three times as long because g was not extended before), where g refers to the offsets at turn k,
- individual FFT of f and g,
- multiplication of F and G that gives H,
- inverse FFT of H.

The output array h^c will then contain the following sums, where the underlined parts contribute to the sums while the other parts vanish due to zero padding,

$$\begin{aligned}
h_0 &= g_0 f_0 + g_1 f_{-1} + g_2 f_{-2} + \cdots + g_{4N_b-1} f_{-4N_b+1} \\
h_1 &= \underline{g_0 f_1} + g_1 f_0 + g_2 f_{-1} + \cdots + g_{4N_b-1} f_{-4N_b+2} \\
h_2 &= \underline{g_0 f_2 + g_1 f_1} + g_2 f_0 + \cdots + g_{4N_b-1} f_{-4N_b+3} \\
&\vdots \\
h_n &= \underline{g_0 f_n + g_1 f_{n-1} + g_2 f_{n-2} + \cdots} + g_n f_0 + \cdots + g_{4N_b-1} f_{-4N_b+n+1} \\
&\vdots \\
h_{N_b} &= \underline{g_0 f_{N_b} + g_1 f_{N_b-1} + g_2 f_{N_b-2} + \cdots + g_{N_b-1} f_1} + \cdots + g_{4N_b-1} f_{-3N_b+1} \\
h_{N_b+1} &= \underline{g_0 f_{N_b+1} + g_1 f_{N_b} + g_2 f_{N_b-1} + \cdots + g_{N_b-1} f_2} + \cdots + g_{4N_b-1} f_{-3N_b+2} \\
&\vdots \\
h_{2N_b-1} &= \underline{g_0 f_{2N_b-1} + g_1 f_{2N_b-2} + g_2 f_{2N_b-3} + \cdots + g_{N_b-1} f_{N_b-1}} + \cdots + g_{4N_b-1} f_{-2N_b} \\
&\vdots \\
h_{4N_b-1} &= g_0 f_{4N_b-1} + g_1 f_{4N_b-2} + g_2 f_{4N_b-3} + \cdots + g_{4N_b-1} f_0.
\end{aligned} \tag{3.32}$$

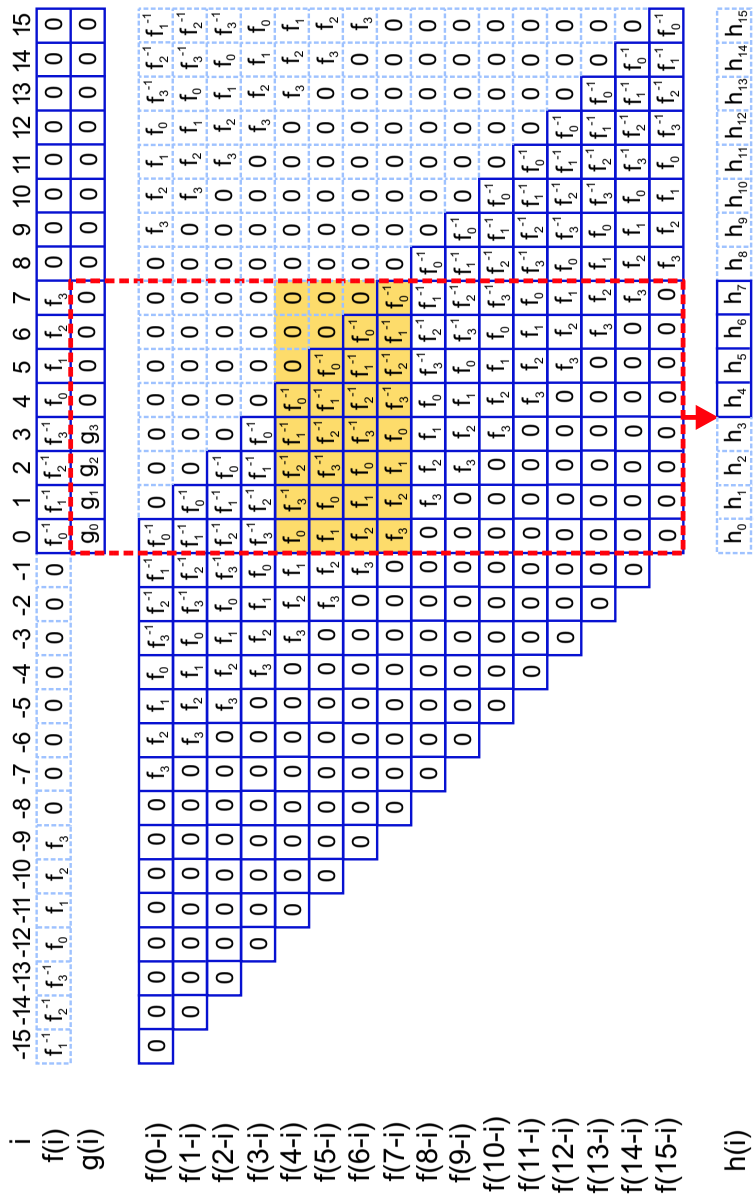

Figure 3.11: *Extension of the linear convolution scheme to allow correct multi-bunch summation. f^{-1} denotes values of the previous turn as described at (3.31). The sums coincide with those in (3.32).*

Also refer to Fig.3.11 for a visualization of this convolution scheme. The important difference consists now in taking the values

$$h_i^c : \quad i = N_b, \ldots, 2N_b - 1, \tag{3.33}$$

as these will now contain exactly the sums (3.30) for $j = 0, \ldots, N_b - 1$. Especially the ${f'}^c_{j-i+N_b}$ contain

$$\begin{aligned} {f'}^c_{j-i+N_b} &= const. \cdot \frac{1}{\sqrt{((c-1)N_b + (j-i+N_b)) \cdot \tau_{buc.}}} \\ &= const. \cdot \frac{1}{\sqrt{(cN_b + j - i) \cdot \tau_{buc.}}}, \qquad i, j = 0, \ldots, 2N_b - 1. \end{aligned} \tag{3.34}$$

Compare with (3.30) to see that both expressions for the denominator are the same.

Hence, using this modified version of the convolution scheme gives us also the multi-bunch multi-turn sums. Again we can compute in ***one*** *convolution operation* the sum of kicks *for* ***each*** *bunch* $j = 0, \ldots, N_b - 1$ at any previous turn k, where n is the current turn number and $c = n - k$

$$h^c_{j+N_b} = {\Delta x'}^j_{n,k} = const. \cdot \sum_{i=0}^{N_b-1} \frac{\langle x \rangle^i_k}{\sqrt{(n-k) \cdot \tau_{rev.} + (j-i) \cdot \tau_{buc.}}} \tag{3.35}$$

Note that each $h^c_{j+N_b}$ contains the effect of all bunches at a previous turn k. Consequently, we finally sum up all corresponding h values to get the multi-turn multi-bunch sum (3.23):

$$\Delta {x'}^j_n = \underbrace{\sum_{c=1}^{n_{\text{mem}}} h^c_{j+N_b}}_{\substack{\text{previous turns} \\ h^c_{j+N_b} \text{ from (3.35)}}} + \underbrace{h^{c=0}_j}_{\substack{\text{current turn} \\ h^{c=0}_j = h_j \text{ from (3.29)}}} \tag{3.36}$$

The FFT convolution algorithm for multi-turn multi-bunch wake kick summation can be summarized as follows:

1. Find the GCD (greatest common divisor) of the given bucket layout. This defines a new, equidistant bunch pattern, for which a bunch spacing τ_b can be defined as well as N_b, the number of possible bunch positions. Define a `mask` that maps the machine's bunch pattern onto the equidistant bunch pattern. The `mask` is used to set $g_i \equiv 0$ for unoccupied positions in the equidistant pattern and to retrieve only respective values from the output array.

2. Set up the arrays ${f'}^c$ of size $4N_b$ containing the appropriate values of the (wake, response) function. Those values remain fixed throughout the process, thus they can be precalculated. The superscript $c = n - k$ denotes the delay in number of turns to which the values of ${f'}^c$ refer to. $c = 0$ is the current turn,

$c = 1, \ldots, n_{mem}$ are the previous turns. We omit the dash $'$ in the following. Set

$$
\begin{aligned}
c = 0 \begin{cases} f_i^{c=0} = f(i \cdot \tau_b) & \forall\, i \in [1, N_b - 1] \\ f_i^{c=0} \equiv 0 & \forall\, i \in [N_b, 4N_b - 1] \\ f_0^{c=0} \equiv 0 & \end{cases} \\
c \geq 1 \begin{cases} f_i^{c\geq 1} = f\left([(c-1)N_b + i] \cdot \tau_b\right) & \forall\, i \in [0, 2N_b - 1] \\ f_i^{c\geq 1} \equiv 0 & \forall\, i \in [2N_b, 4N_b - 1] \\ f_0^{c=1} \equiv 0. & \end{cases}
\end{aligned}
\tag{3.37}
$$

Note that only $f_0^{c=1}$ is set to zero, it does not apply to $f_0^{c>1}$.

3. Precalculate FFTs of f^c for $c = 0, \ldots, n_{\text{mem}}$, this gives arrays $F^c = \mathcal{F}[f^c]$.

4. As another initialization step, zero pad an array g of length $4N_b$. Set $g_i \equiv 0\ \forall\, i \in [N_b, 4N_b - 1]$.

5. At turn n do the following:

   - Renumbering of arrays G^c: $G^{c=i} \longrightarrow G^{c=i+1}$, especially $G^{c=0}$ becomes $G^{c=1}$ and the array $G^{c=n_{\text{mem}}}$ is discarded.
   - Write (signal, offsets) to array g_i using the `mask`.
   - FFT of g. $G^{c=0} = \mathcal{F}[g]$.
   - Multiplication $\forall\, c \in [0, n_{\text{mem}}]:\ H^c = F^c \cdot G^c$.
   - Inverse FFT $\forall\, c \in [0, n_{\text{mem}}]:\ h^c = \mathcal{F}^{-1}[H^c]$.
   - Sum over n_{mem} turns to get the kicks, use the `mask`: $\Delta x'^j_n = \sum_{c=1}^{n_{\text{mem}}} h^c_{j+N_b} + h^{c=0}_j$.

In the next section we prove that this algorithm is indeed faster than direct computation of the linear convolution.

A note on implementation: Mind that the FFT only works for equidistant samples, this is why we have to use a mask. If the bunch pattern in the machine is not equidistant it is indicated to find the greatest common divisor of all bunch spacings. In the worst case (which hardly occurs) the number of possible bunch positions is given by the harmonic number h of the machine. Even for the LHC with $h = 35640$ this is computationally no problem.

There are optimized implementations of the FFT (e.g. the library FFTW [18, 17]). For the transform of purely real sequences rearranging of the samples might be needed. In usual accelerator applications however the complex FFT might have some advantages: Both transverse planes can be handled by assorting samples of the horizontal plane in the real part of g and samples of the vertical plane in the imaginary part of g. After performing the FFT convolution algorithm the real and imaginary parts of h will contain the corresponding output for each plane. An

important condition is however, that the "response"function f is the same for both planes. This works nicely for the resistive wall wake function in its classic form, even the Yokoya factors can be used. But as soon as the wake function takes a different form for each plane, which cannot be equalized and resolved by outsourcing the interfering terms to the sequence g, this approach does not work any more.

The interested reader might want to note that we could use a two-dimensional FFT convolution algorithm instead of the just presented one to serve in principle the same purpose. However, for the problem of wake kick summation, the algorithm presented here is easier to implement and possibly faster.

3.5.3 Speed Considerations

Consider the direct summation (3.23). At each turn this expression has to be evaluated for N bunches, hence

$$\begin{aligned}&\sum_{k=1}^{N}[n_{\mathrm{mem}}\cdot(N+N)+(k+k)]\\&=2n_{\mathrm{mem}}N^2+2\frac{N(N+1)}{2}=\\&=(2n_{\mathrm{mem}}+1)N^2+N\end{aligned}$$

operations have to carried out. Clearly one sees the quadratic nature of this expression.

Now for the FFT convolution algorithm, remember that only one new FFT per turn is needed, then multiplications of $n_{\mathrm{mem}}+1$ arrays of length $4N$ have to be carried out and also $n_{\mathrm{mem}}+1$ inverse FFTs. Finally we have to sum $N\cdot n_{\mathrm{mem}}+1$ values, thus

$$\begin{aligned}&4N\log 4N+4N(n_{\mathrm{mem}}+1)+4N\log 4N(n_{\mathrm{mem}}+1)+N(n_{\mathrm{mem}}+1)=\\&(n_{\mathrm{mem}}+2)4N\log 4N+(5n_{\mathrm{mem}}+5)N\end{aligned}$$

computation steps will be carried out.

3.6 Fourier Transform and Convolution Basics

We exploit the fact, that *multiplication* in the frequency domain corresponds to *convolution* in the time domain. Moreover multiplication in one domain is equivalent to convolution in the other domain and vice versa, but we only needed one of the directions.

This basic technique was known since the days of Fourier, but not used much before 1965, when the FFT (Fast Fourier transform) was developed. The task is transformed into the frequency domain using the discrete Fourier transform (DFT), there the summation reduces to a multiplication, and then it is transformed back into the time domain using the inverse DFT. By using the FFT algorithm to calculate the DFT, convolution via the frequency domain can be faster than directly convolving the time domain signals/functions.

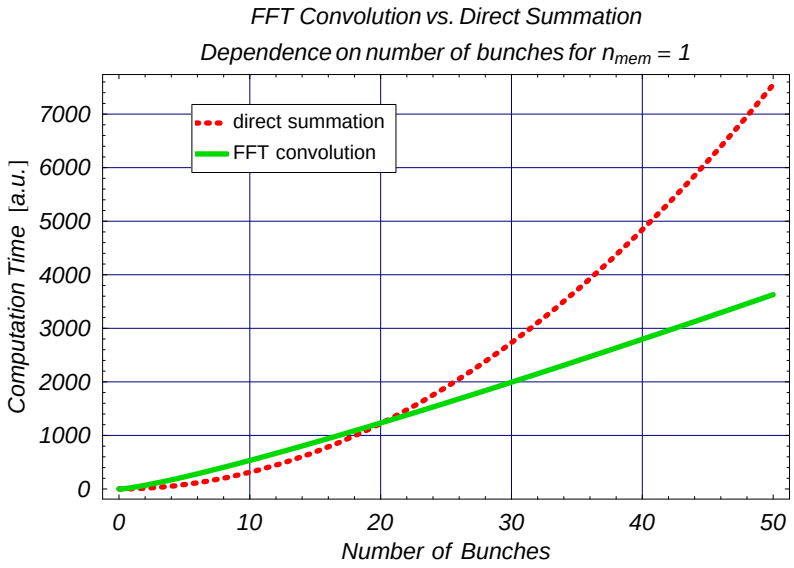

Figure 3.12: *When using the direct summation, the number of floating point operations (FLOPS) increases quadratically with the number of bunches, whereas the FFT convolution shows only a logarithmic dependence. If only 1 turn needs to be summed up and the number of bunches is little, the direct summation can be faster.*

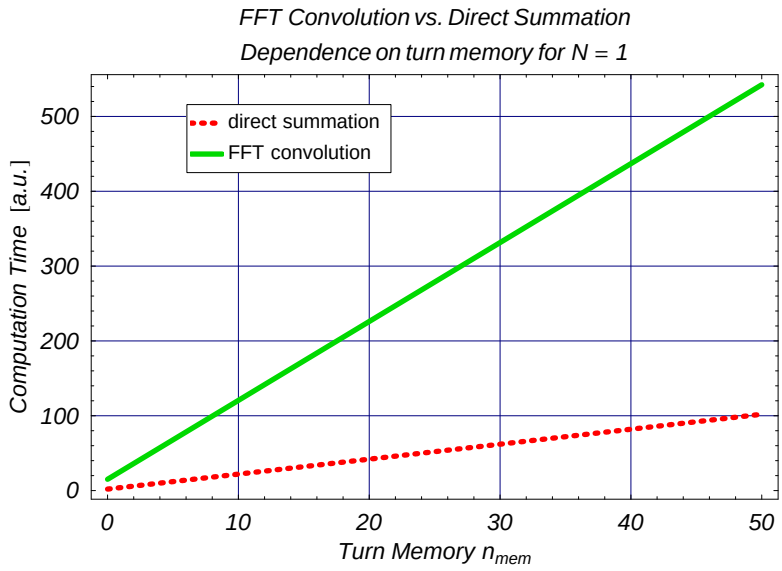

Figure 3.13: *For a single bunch, the direct summation is always faster than the FFT convolution algorithm.*

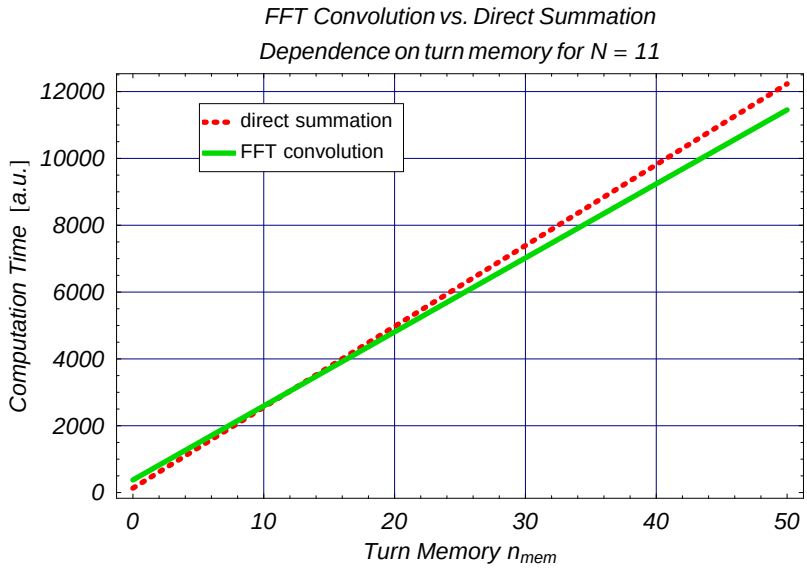

Figure 3.14: *In the present implementation of the FFT convolution algorithm, the break-even point is at 11 bunches.*

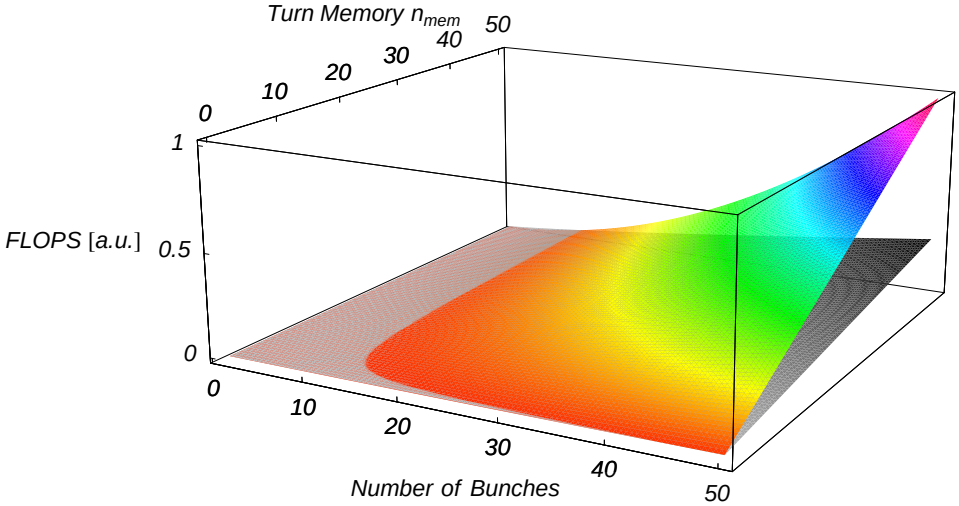

Figure 3.15: *The colored surface shows the quadratical behavior of the direct summation and the grey-scale surface the logarithmic behavior of the FFT convolution as function of number of bunches and amount of turn memory.*

3.6.1 Continuous Data

A convolution is an integral which expresses the amount of overlap of one function g as it is shifted over another function f. It therefore "mingles"or "blends"one function with another. The convolution is sometimes also known by its German name, Faltung ("folding").

Definition 3.6.1 (Convolution)
Abstractly, a convolution is defined as a product of functions f and g. Convolution of two functions $f(x)$ and $g(x)$ over a finite range $[0, t]$ is given by

$$h(t) = f * g \equiv \int_0^t d\tau \; f(\tau) g(t-\tau)\,, \tag{3.38}$$

where the symbol $*$ denotes convolution of f and g. Convolution is more often taken over an infinite range,

$$h(t) = f * g \equiv \int_{-\infty}^{\infty} d\tau \; f(\tau) g(t-\tau) = \int_{-\infty}^{\infty} d\tau \; g(\tau) f(t-\tau)\,. \tag{3.39}$$

Definition 3.6.2 (Fourier Transform)
The Fourier transform is an integral transform defined within the scope of this section as

$$F(\omega) = \qquad \mathcal{F}\left[f(t)\right] = \int_{-\infty}^{\infty} f(t)\, e^{-j\,\omega t}\; dt \tag{3.40}$$

$$f(t) = \quad \mathcal{F}^{-1}\left[F(\omega)\right] = \frac{1}{2\pi} \int_{-\infty}^{\infty} F(\omega)\, e^{j\,\omega t}\; d\omega\,, \tag{3.41}$$

where $\mathcal{F}$ is called the *forward* $(-j)$ and $\mathcal{F}^{-1}$ is called the *backward* (j) Fourier transform. The notation $\widetilde{f}(\omega)$ instead of $F(\omega)$ is also used for the inverse Fourier transform.

Let $f(t)$ and $g(t)$ be arbitrary functions of time t with Fourier transforms,

$$f(t) = \mathcal{F}^{-1}[\widetilde{f}(\omega)] = \frac{1}{2\pi} \int_{-\infty}^{\infty} d\omega \; \widetilde{f}(\omega) \exp\left(j\,\omega t\right), \tag{3.42}$$

$$g(t) = \mathcal{F}^{-1}[\widetilde{g}(\omega)] = \frac{1}{2\pi} \int_{-\infty}^{\infty} d\omega \; \widetilde{g}(\omega) \exp\left(j\,\omega t\right). \tag{3.43}$$

Then the convolution is

$$\begin{aligned} f * g &\equiv \int_{-\infty}^{\infty} g(\tau) f(t-\tau)\; d\tau \\ &= \int_{-\infty}^{\infty} g(\tau) \left[\int_{-\infty}^{\infty} \widetilde{f}(\omega) \exp\left(j\,\omega(t-\tau)\right)\; d\omega \right]\; d\tau\,. \end{aligned} \tag{3.44}$$

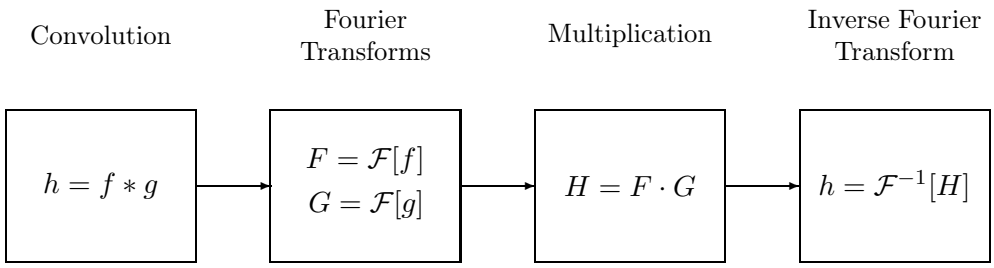

Figure 3.16: *The convolution theorem*

Interchange the order of integration,

$$\begin{aligned} f * g &= \int_{-\infty}^{\infty} \widetilde{f}(\omega) \left[\int_{-\infty}^{\infty} g(\tau) \exp\left(-j\,\omega\tau\right)\, d\tau \right] \exp\left(j\,\omega t\right)\, d\omega \\ &= \int_{-\infty}^{\infty} \widetilde{f}(\omega)\widetilde{g}(\omega)\, \exp\left(j\,\omega t\right)\, d\omega \\ &= \mathcal{F}^{-1}\left[\widetilde{f}(\omega)\widetilde{g}(\omega)\right]. \end{aligned} \tag{3.45}$$

Theorem 3.6.1 (Convolution Theorem)
Applying a Fourier transform to each side, we have

$$\begin{aligned} \mathcal{F}\left[f * g\right] = \mathcal{F}\left[\mathcal{F}^{-1}\left[\widetilde{f}(\omega)\widetilde{g}(\omega)\right]\right] = \widetilde{f}(\omega)\widetilde{g}(\omega) = \\ = \mathcal{F}[f]\mathcal{F}[g]\,. \end{aligned} \tag{3.46}$$

Hence, we arrived at the convolution theorem, *which states that the Fourier transform of the convolution of to functions f and g equals the product of the separate Fourier transforms of f and g. The convolution theorem also takes the alternate forms*

$$\mathcal{F}\left[fg\right] = \mathcal{F}\left[f\right] * \mathcal{F}\left[g\right] \tag{3.47}$$

$$\mathcal{F}^{-1}\left[\mathcal{F}[f]\mathcal{F}[g]\right] = f * g \tag{3.48}$$

$$\mathcal{F}^{-1}\left[\mathcal{F}[f] * \mathcal{F}[g]\right] = fg\,. \tag{3.49}$$

We use the convolution theorem in the form (3.48).

3.6.2 Discrete Data

In most cases we do not deal with continuous functions but with sampled data. The Convolution, the Fourier Transform and the Convolution Theorem can also be defined and derived for sampled data. Consider a sequence x_k with N samples of the form

$$x_0, x_1, x_2, \ldots, x_{N-1} \tag{3.50}$$

The FT will further assume that the series outside the range $0, \ldots, N-1$ is periodically continued, that is, $x_k = x_{k+N}$ for all k.

Definition 3.6.3 (Discrete Convolution)
The discrete convolution is defined as the sum of products of array-elements f_i and g_i. The arrays can directly be given as a sequence or result from the sampling of continuous data.

$$g * f = \sum_{k=-M/2+1}^{M/2} g_k \cdot f_{j-k} \tag{3.51}$$

$$h(n) = g * f = \sum_{k=0}^{N-1} g(k)\, f(n-k) = \sum_{k=0}^{N-1} g_k\, f_{n-k}\,, \tag{3.52}$$

Definition 3.6.4 (Discrete Fourier Transform)
The discrete Fourier transform is defined analogous to the continuous case, for a sequence $x(k)$ and its Fourier transform sequence $X(n)$

$$X(n) = \quad \mathcal{F}\left[x(k)\right] = \frac{1}{N} \sum_{k=0}^{N-1} x(k)\, e^{-j\ 2\pi n/N\, k} \quad \text{for } n = 0, \ldots, N-1 \tag{3.53}$$

$$x(k) = \quad \mathcal{F}^{-1}\left[X(n)\right] = \sum_{n=0}^{N-1} X(n)\, e^{j\ 2\pi k/N\, n} \quad \text{for } k = 0, \ldots, N-1, \tag{3.54}$$

where $\mathcal{F}$ is called the *forward* $(-j)$ and $\mathcal{F}^{-1}$ is called the *backward* (j) Fourier transform. The notation $\widetilde{f}(\omega)$ instead of $F(\omega)$ will also be used for the inverse Fourier transform.

Theorem 3.6.2 (Discrete Convolution Theorem)
The discrete version of the convolution theorem reads formally exactly the same as the continuous case.

3.7 An Alternative Phasor-Like Approach

To evaluate Eq. (3.21) one can find a recursive scheme to calculate the sum, by taking further assumptions into account. If we assume the $\langle x \rangle_k$ to be strictly given by a betatron oscillation with angular frequency ω_β, we can write:

$$\langle x \rangle_k = \mathrm{Re}\left[A \cdot e^{i(\omega_\beta\, k\, \tau_{rev.} + \theta)}\right] \tag{3.55}$$

But for simplicity, we do not write down Re for the Real part, but we just write:

$$\langle x \rangle_k = A \cdot e^{i(\omega_\beta\, k\, \tau_{rev.} + \theta)} \tag{3.56}$$

where $\tau_{rev.}$ is the revolution time, k is an integer index, θ is some starting phase and ω_β is defined by (where Q is the tune)

$$\omega_\beta = \frac{2\pi Q}{\tau_{rev.}} = \omega_0 Q \tag{3.57}$$

Therefore the summation of the kicks becomes:

$$\Delta x'_n = \sum_{k=0}^{n-1} \frac{\langle x \rangle_k}{\sqrt{(n-k)\tau_{rev.}}} = \sum_{k=0}^{n-1} \frac{A \cdot e^{i(\omega_\beta k \tau_{rev.} + \theta)}}{\sqrt{(n-k)\tau_{rev.}}} = S_n \tag{3.58}$$

And for the next turn we get:

$$\Delta x'_{n+1} = \sum_{k=0}^{n} \frac{\langle x \rangle_k}{\sqrt{(n+1-k)\tau_{rev.}}} = \sum_{k=0}^{n} \frac{A \cdot e^{i(\omega_\beta \, k \, \tau_{rev.} + \theta)}}{\sqrt{(n+1-k)\tau_{rev.}}} = S_{n+1} \tag{3.59}$$

It is now straightforward to find a relation between the sums S_n and S_{n+1}:

$$\begin{aligned}
S_{n+1} =& S_n \cdot e^{i\,\omega_\beta\,\tau_{rev.}} + \left. \frac{A \cdot e^{i(\omega_\beta \, k \, \tau_{rev.} + \theta)}}{\sqrt{(n+1-k)\tau_{rev.}}} \right|_{k=0} = \\
=& \left(\sum_{k=0}^{n-1} \frac{A \cdot e^{i(\omega_\beta \, k \, \tau_{rev.} + \theta)}}{\sqrt{(n-k)\tau_{rev.}}} \right) \cdot e^{i\,\omega_\beta\,\tau_{rev.}} + \left. \frac{A \cdot e^{i(\omega_\beta \, k \, \tau_{rev.} + \theta)}}{\sqrt{(n+1-k)\tau_{rev.}}} \right|_{k=0} \\
=& \sum_{k=0}^{n-1} \frac{A \cdot e^{i(\omega_\beta \, (k+1) \, \tau_{rev.} + \theta)}}{\sqrt{(n-k)\tau_{rev.}}} + \left. \frac{A \cdot e^{i(\omega_\beta \, k \, \tau_{rev.} + \theta)}}{\sqrt{(n+1-k)\tau_{rev.}}} \right|_{k=0} \\
=& \sum_{k=1}^{n} \frac{A \cdot e^{i(\omega_\beta \, k \, \tau_{rev.} + \theta)}}{\sqrt{(n+1-k)\tau_{rev.}}} + \left. \frac{A \cdot e^{i(\omega_\beta \, k \, \tau_{rev.} + \theta)}}{\sqrt{(n+1-k)\tau_{rev.}}} \right|_{k=0} \\
=& \sum_{k=0}^{n} \frac{A \cdot e^{i(\omega_\beta \, k \, \tau_{rev.} + \theta)}}{\sqrt{(n+1-k)\tau_{rev.}}} = S_{n+1}
\end{aligned} \tag{3.60}$$

In this way, the sum can be easily implemented in a computer code, but it is **un**physical, when the ω_β changes during the simulation and does not remain constant. Hence, large variations in ω_β do not allow the use of this phasor-like approach.

3.8 Simulation code MultiTRISIM

3.8.1 Equations of Motion

The approximations discussed in the previous sections are all used in the simulation code MultiTRISIM. The equations to describe the motion of the macro-particles follow the same formalism as in the predecessor TRISIM3D [42].

The longitudinal motion is described by the energy deviation ε and the time delay t with respect to a synchronous reference particle. For the transverse motion the horizontal and vertical positions x, y and divergences x', y' are used. The transverse coordinates are represented by a 4-dimensional vector

$$\mathbf{z} = \begin{pmatrix} x \\ x' \\ y \\ y' \end{pmatrix} \tag{3.61}$$

The transfer matrix is a 4×4 matrix $\mathbf{M}$. The different elements of the accelerator are taken into account by point-like interactions, i.e. kick is applied to the particle while the position remains the same. The effect of such a point-like element on the macro-particle can be written as

$$\mathbf{z}_i^* = \mathbf{z}_i + \delta\mathbf{z}_i \tag{3.62}$$
$$\varepsilon_i^* = \varepsilon_i + \delta\varepsilon_i \tag{3.63}$$
$$t_i^* = t_i \tag{3.64}$$

where $\delta\varepsilon_i$ is the londitudinal energy change and where

$$\delta\mathbf{z}_i = \begin{pmatrix} 0 \\ \delta x' \\ 0 \\ \delta y' \end{pmatrix} \tag{3.65}$$

corresponds to the horizontal and vertical kicks caused by the elements. For the drift sections between elements, a linear transfer matrix $\mathbf{M}$ is assumed

$$\mathbf{M} = \begin{pmatrix} M_{11} & M_{12} & 0 & 0 \\ M_{21} & M_{22} & 0 & 0 \\ 0 & 0 & M_{33} & M_{34} \\ 0 & 0 & M_{43} & M_{44} \end{pmatrix} \tag{3.66}$$

with components

$$M_{11}(\varepsilon_i^*) = \exp\left(-\frac{T_i}{\tau_x}\right)\sqrt{\frac{\beta_{x,i+1}}{\beta_{x,i}}}\cos\left(\Psi_i(\varepsilon_i^*)\right) \tag{3.67}$$
$$M_{12}(\varepsilon_i^*) = \sqrt{\beta_{x,i+1}\,\beta_{x,i}}\sin\left(\Psi_i(\varepsilon_i^*)\right) \tag{3.68}$$
$$M_{21}(\varepsilon_i^*) = \exp\left(-\frac{T_i}{\tau_x}\right)\frac{1}{\sqrt{\beta_{x,i+1}\,\beta_{x,i}}}\sin\left(\Psi_i(\varepsilon_i^*)\right) \tag{3.69}$$
$$M_{22}(\varepsilon_i^*) = \sqrt{\frac{\beta_{x,i}}{\beta_{x,i+1}}}\cos\left(\Psi_i(\varepsilon_i^*)\right) \tag{3.70}$$
$$M_{33}(\varepsilon_i^*) = \exp\left(-\frac{T_i}{\tau_y}\right)\sqrt{\frac{\beta_{y,i+1}}{\beta_{y,i}}}\cos\left(\Psi_i(\varepsilon_i^*)\right) \tag{3.71}$$
$$M_{34}(\varepsilon_i^*) = \sqrt{\beta_{y,i+1}\,\beta_{y,i}}\sin\left(\Psi_i(\varepsilon_i^*)\right) \tag{3.72}$$
$$M_{43}(\varepsilon_i^*) = \exp\left(-\frac{T_i}{\tau_y}\right)\frac{1}{\sqrt{\beta_{y,i+1}\,\beta_{y,i}}}\sin\left(\Psi_i(\varepsilon_i^*)\right) \tag{3.73}$$
$$M_{44}(\varepsilon_i^*) = \sqrt{\frac{\beta_{y,i}}{\beta_{y,i+1}}}\cos\left(\Psi_i(\varepsilon_i^*)\right) \tag{3.74}$$

The following definitions have been used:

$$u_i = (E_r + \varepsilon_i^*)\frac{Q_i}{1+Qi} \tag{3.75}$$

$$Q_i = U_i\frac{E_r+\varepsilon_i^*}{E_r^2} \tag{3.76}$$

$$\Psi_i(\varepsilon_i^*) = \Phi_i^0\left[1+\left(\frac{\xi_i-\eta}{E_r}\right)\left(\varepsilon_i^*-\frac{1}{2}u_i\right)\right] \tag{3.77}$$

The symbols used in the previous equations are summarized in the following list:

T_0 ... Revolution time in the reference particle,
T_i ... Transit time of the reference particle through sector i,
E_r ... Nominal energy of the particles,
σ_ε^0 ··· Natural RMS energy spread,
τ_ε ... Energy damping time,
τ_x, τ_y ... Horizontal resp. vertical damping time,
U_i ... Synchrotron radiation energy loss in the i-th sector,
ξ_i ... Chromaticity in the i-th sector, $\xi = (\delta Q/Q)/(\delta p/p) = Q'/Q$
α ... Momentum compaction factor: $\alpha = (\delta C/C)/(\delta p/p)$,
η ... Momentum slip factor $\eta = \alpha - 1/\gamma^2$,
Φ_i^0 ... Betatron phase advance of the reference particle in sector i,
$\beta_{x,i}$, $\beta_{y,i}$ ... horizontal and vertical β-function,
$\overline{\beta}_x$, $\overline{\beta}_y$ ... average horizontal and vertical β-function at the i-th element, $\overline{\beta} = R/Q$

(3.78)

The equations of motion for the drift sections between the elements can now be written as

$$\mathbf{z}_{i+1} = \mathbf{M}(\varepsilon_i^*)\cdot\mathbf{z}_i^* + \mathbf{R}_i \tag{3.79}$$

$$\varepsilon_{i+1} = \varepsilon_i^* - u_i + 2\sigma_\varepsilon^0\sqrt{\frac{T_0}{\tau_\varepsilon}}R_i^{(5)} \tag{3.80}$$

$$t_{i+1} = t_i^* + \alpha T_i\left[\frac{\varepsilon_i^*+E_r}{E_r}\frac{\ln(1+Q_i)}{Q_i} - 1\right] \tag{3.81}$$

where

$$\mathbf{R}_i = \begin{pmatrix} \sqrt{\frac{2\varepsilon_x\overline{\beta}_x T_0}{\tau_x}}R_i^{(1)} \\ \sqrt{\frac{2\varepsilon_x}{\overline{\beta}_x T_0\tau_x}}R_i^{(2)} \\ \sqrt{\frac{2\varepsilon_y\overline{\beta}_y T_0}{\tau_y}}R_i^{(3)} \\ \sqrt{\frac{2\varepsilon_y}{\overline{\beta}_y T_0\tau_y}}R_i^{(4)} \end{pmatrix} \tag{3.82}$$

takes into account the quantum excitation due to synchrotron radiation. All the options related to synchrotron radiation can be switched off if protons are simulated.

3.8.2 Machine Elements

RF cavity

To be able to simulate synchrotron motion of the macro-particles, a RF cavity is usually included in the simualtion setup. Using the defintions

$$V_i^{RF} \quad \ldots \quad \text{amplitude of the RF voltage,} \tag{3.83}$$
$$\omega_i^{RF} \quad \ldots \quad \text{angular frequency of the RF wave,} \tag{3.84}$$
$$\Phi_i^s \quad \ldots \quad \text{phase angle of the synchronous particle w.r.t. the RF wave,} \tag{3.85}$$
$$\delta\mathbf{z}_i,\, \delta\mathbf{z}_i \quad \ldots \quad \text{longitudinal and transverse kicks due to the wake field} \tag{3.86}$$

the interaction of macro-particles with a cavity can be written as

$$\mathbf{z}_i^* = \mathbf{z}_i + \delta\mathbf{z}_i \tag{3.87}$$
$$\varepsilon_i^* = \varepsilon_i + \delta\varepsilon_i + eV_i^{RF} \sin\left(\Phi_i^s + \omega_i^{RF} t_i\right) \tag{3.88}$$

Impedance (generic)

The interaction of the macro-particles of an impedance element is generally described as

$$\mathbf{z}_i^* = \mathbf{z}_i + \delta\mathbf{z}_i \tag{3.89}$$
$$E_i = \varepsilon_i + \delta\varepsilon_i \tag{3.90}$$

where $\delta\mathbf{z}_i$ and $\delta\epsilon_i$ are the longitudinal and transverse kicks due to the wake field.

Octupole

In order to include non-linearity effects, octupoles have been included in the code as well. The effect of the octupole on the macro-particles is given by

$$\begin{aligned} \delta x' &= \frac{k_3 \cdot l}{3!}\left(x^3 - 3\,x\,y^2\right) \\ \delta y' &= \frac{k_3 \cdot l}{3!}\left(3\,x^2\,y - y^3\right) \end{aligned} \tag{3.91}$$

where the octupole strength is given by

$$k_3 = \frac{e\,O_3}{p} \tag{3.92}$$

and l is the length of the magnet, O_3 its field gradient and p the average momentum of the particles.

Chapter 4

Resistive Wall Impedance Models

4.1 Introduction

Calculation of the transverse resistive wall impedance of a cylindrical pipe with (arbitrary) surface impedance have been performed by B. Zotter [47] and G. Nassibian and F. Sacherer [26]. L. Vos [41] has revised these studies, starting from a different ansatz, but finally arriving at the same results in case of a thin wall. The concept of so-called inductive bypass is the major novelty in this derivation. This has been found to be of major importance for LHC since the resulting resistive wall impedance is much weaker than the classical one giving hope for more beam stability.

More recently A. Burov and V. Lebedev [9] have calculated the transverse impedance for multi-layer round and flat chambers. A. Mostacci and F. Caspers [25] performed bench measurements to verify the behavior of the resistive wall impedance for low frequencies for standard beam pipe geometry and material, which agrees with above mentioned impedance formulae.

H. Tsutsui [39] used a field matching technique to compare numerical results obtained by the program HFSS for the LHC collimators.

Finally L. Vos [40, 41] derived the impedance of multi-layer vacuum chambers using transmission line theory and gives a closed analytic expression for the transverse resistive wall impedance of a vacuum chamber of finite thickness that is valid from zero frequency to infinity.

In this chapter we compile the various impedance formulae and show their behavior for some sets of the extreme parameters of the LHC collimators as well as for "standard"parameters. The purpose is to show that there is convergence of all formulae in the case of moderate, classical parameters but increasing divergence for more unusual ones, as for the LHC collimators.

Additionally the wake functions of the known impedance formulae are given as well as the "new"ones derived.

4.2 Review of various resistive wall formulae

4.2.1 Classical formulae

Various references [12, 16] show the derivation of the transverse resistive (thick) wall impedance in round pipes as well as the wake function. Therefore we give here only the expressions for the lowest dipole mode $m = 1$ (expressions for higher modes can be found in [13, p.204]) and recall the properties shortly:

$$Z_{m=1}^{\perp,\,\mathrm{thick}}(\omega) = (\mathrm{sgn}\,\omega + j)\,\frac{Z_0\,L\,\delta_0\,\mu_r}{2\,\pi\,a^3}\cdot\sqrt{\frac{\omega_0}{|\omega|}}, \tag{4.1}$$

$$Z_{m=1}^{\perp,\,\mathrm{thin}}(\omega) = \frac{c\,L}{\pi\,a^3\,\sigma_c\,d\cdot\omega}, \tag{4.2}$$

In the above formula c denotes the speed of light, L indicates the length over which the impedance is defined (e.g. $L = 2\pi R =$ the machine circumference), b is the vacuum chamber radius, μ_0 and μ_r denote the free space and relative permeability, respectively, and finally σ_c designates the conductivity of the vacuum chamber wall. In the second expression the quantities $\omega_0 = 2\pi/\tau_{rev}$, the angular revolution frequency, and $Z_0 = c\,\mu_0$, the free space impedance, were used. Consequently, δ_0 denotes the skin depth at the angular revolution frequency. Any expressions are given in *MKSA* units.

4.2.2 Resistive wall with inductive bypass

L.Vos gave a new procedure to obtain the transverse impedance of a cylindrical beam pipe from an arbitrary longitudinal surface impedance [41] by including a so-called "inductive bypass". Once the longitudinal wall impedance $Z_\parallel$ per unit length is known the transverse impedance $Z_\perp^{\mathrm{ibp}}$ is computed from

$$Z_\perp^{\mathrm{ibp}} = \frac{2c}{b^2\omega}\cdot\frac{Z_\parallel Z_{\mathrm{ind}}}{Z_\parallel + Z_{\mathrm{ind}}} \tag{4.3}$$

where the inductive bypass is given by $Z_{\mathrm{ind}} = j\,\omega\mu_0/4\pi$. Historically, applying this concept to (4.1) was used to get a more realistic impedance estimate for the LHC collimators (see also (4.7)).

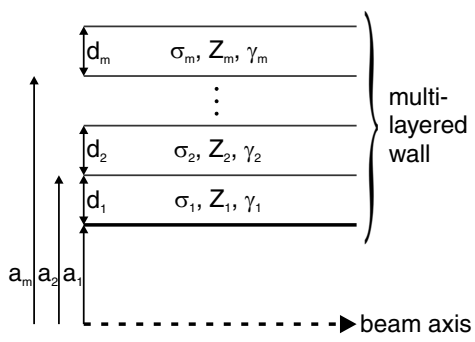

Additionally L.Vos proposed to compute the longitudinal impedance of multi-layer vacuum chambers using the theory of transmission lines [40], which implicitly takes into account Maxwell's equations with the proper boundary conditions.

Both formalisms combined give transverse impedance expressions for any number of concentric layers with any electric conductivity, magnetic permeability and dielectric constant. Furthermore, it results in only a

simple formula for the transverse resistive-wall impedance from zero frequency to infinity, without having to distinguish between the cases where the skin depth is smaller or bigger than the wall thickness.

The formalism for n layers assumes the outermost layer to extend to infinity, i.e. it loads the previous layer with its intrinsic impedance Z_n. Using for layer m its intrinsic impedance

$$Z_m = \sqrt{j\,\omega\mu_m / \left(j\,\omega\epsilon_m + \sigma_m\right)}, \tag{4.4}$$

its radial propagation constant

$$\gamma_m = \sqrt{j\,\omega\mu_m\left(\sigma_m + j\,\omega\epsilon_m\right) + \left(\omega/\beta c\right)^2} \tag{4.5}$$

and its thickness d_m, the input impedance $Z_{i,m}$ per unit length of each layer can be computed recursively

$$Z_{i,m} = Z_m \frac{Z_{i,m+1}\cosh\gamma_m d_m + Z_m \sinh\gamma_m d_m}{Z_m\cosh\gamma_m d_m + Z_{i,m+1}\sinh\gamma_m d_m}.$$

Finally the longitudinal impedance $Z_\parallel = Z_{i,1}/\left(2\pi b\right)$ is used to compute the transverse impedance as described before. Especially the case of a finite chamber wall ($n = 2$, where layer 2 is vacuum extending to infinity) gives

$$Z_{m=1}^{\perp,\mathrm{LV}}(\omega) \quad = \quad \frac{Z_0\,L}{2\,\pi\,b^2} \quad \cdot \quad \left[\frac{b\omega\mu_0}{2Z_0}\cdot\frac{1+\frac{Z_0}{Z_1}\tanh\gamma_1 d_1}{1+\frac{Z_1}{Z_0}\tanh\gamma_1 d_1} - j\right]^{-1}. \tag{4.6}$$

Taking the limit $|\gamma_1 d_1| \gg 1$ in (4.6) gives

$$Z_{m=1}^{\perp,\mathrm{thick,ibp}}(\omega) \;=\; (1 + j\ \mathrm{sgn}\,\omega)\ \frac{Z_0\,L}{2\,\pi\,b^2}\ \cdot\frac{1}{-\,j + \mathrm{sgn}\,\omega\left(1 + b\sqrt{\frac{\sigma_c\,\mu_0}{2\,\mu_r}}\,\sqrt{|\omega|}\right)}, \tag{4.7}$$

which can be obtained as well by applying the concept of inductive bypass to (4.1). Expression (4.7) was originally used for the impedance estimates of LHC collimators. Note that the assumption $d \to \infty$ does not entirely reflect the physics we want to model, however the formula gives good results for the parameters under consideration. Applying the concept of inductive bypass to (4.2) or on the other hand taking the limit $|\gamma_1 d_1| \ll 1$ in (4.6) gives

$$Z_{m=1}^{\perp,\mathrm{thin,ibp}}(\omega) = \frac{Z_0\,L}{2\,\pi\,b^2}\cdot\frac{1}{\frac{1}{2}\,b\,d\,\sigma\,\mu_0\cdot\omega - j}, \tag{4.8}$$

which is a known formula for thin metal walls already reported in [49].

The approach by L.Vos requires that the wave length of the oscillationsis large compared to the beam pipe radius $\beta c/\omega \gg b$. This is almost always satisfied in any accelerator. However, further limits of applicability are not specified in references [41, 40].

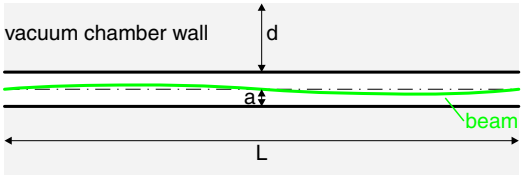

Figure 4.1: *Quasi-static beam model used by BL. For the structure in consideration the beam slope is negligible.*

4.2.3 Quasi-static beam model

Burov and Lebedev [9] follow a different approach to calculate the transverse resistive wall impedance. They use a quasi-static beam model, where the beam is represented by an electric plus a magnetic dipole (see Fig. 4.1). The solution is then accomplished by solving Poisson's equation for the electric dipole and computing the longitudinal vector potential associated with the the magnetic dipole.

Also this approach requires that the wave length of the oscillations is large compared to the beam pipe radius $\beta c/\omega \gg b$. Furthermore the assumption $L \gg b$ is needed, hence the structure is long compared to the aperture. This is in particular the case for the LHC collimators, where $L/b \approx 500$.

This formalism gives the transverse impedance for any number of concentric layers. By using the wave vector $\kappa_m = \sqrt{j\,\sigma_m \mu_{r,m} \mu_0\,\omega}$ and the medium parameter $\tilde{\kappa}_m = \kappa_m/\mu_{r,m}$ associated with layer m, the transfer from layer m to a layer $m-1$, with $2 \le m \le n-1$, is found as

$$T_{m-1} = -\frac{\mathrm{c}'_{m-1}(\kappa_{m-1}a_m) - T_m\tilde{\kappa}_{m,m-1}\mathrm{c}_{m-1}(\kappa_{m-1}a_m)}{\mathrm{s}'_{m-1}(\kappa_{m-1}a_m) - T_m\tilde{\kappa}_{m,m-1}\mathrm{s}_{m-1}(\kappa_{m-1}a_m)}, \tag{4.9}$$

where s and c, the basis sine and cosine hyperbolic Bessel solutions, and their derivatives are defined in [9]. Starting the recursion scheme with $T_n = 1$, letting $\tilde{\kappa}_{m,m-1} = \tilde{\kappa}_m/\tilde{\kappa}_{m+1}$ and $\tilde{\kappa}_n = 1/(b_n\mu_{r,n})$ for a non-conducting unbounded outermost layer, the impedance is finally given by

$$Z_\perp(\omega) = j\,\frac{Z_0 L}{2\pi b^2}\cdot\frac{2}{1-\tilde{\kappa}_1 b\,T_1} \tag{4.10}$$

The particular case of only two layers (one layer being the vacuum chamber wall of finite thickness and vacuum outside) gives the general expression for the transverse resistive-wall impedance,

$$Z^{\perp,\mathrm{BL}}_{m=1}(\omega) = j\,\frac{Z_0\beta L}{\pi b^2}\frac{\mathrm{s}'_1 + \tilde{\kappa}_{2,1}\mathrm{s}_1}{\mathrm{s}'_1 + \tilde{\kappa}_{2,1}\tilde{\kappa}_{1,0}\mathrm{c}_1 + \tilde{\kappa}_{2,1}\mathrm{s}_1 + \tilde{\kappa}_{1,0}\mathrm{c}'_1} \tag{4.11}$$

4.2.4 Field Matching

The transverse impedance of a vacuum chamber consisting of several concentric, annular layers[47], was originally found using a source model[23] consisting of an

oscillating, uniform, cylindrical beam of charged particles, where the transverse displacements are replaced by surface charges (and currents) [23]. The longitudinal electric and magnetic field components in any uniform region can be obtained by solving the wave equations with appropriate source terms. The transverse field components can then be found directly from Maxwell's equations, but again source terms need to be included.

Matching all 4 tangential field components E_z, E_θ, B_z, and B_θ on all boundaries between the layers permits determination of the fields in the beam region and hence of the (transverse) impedance.

More recently, another source model has been introduced[10, 19] which is better adapted to bunched and/or non-uniform beams: an infinitesimal ring whose charge density is modulated azimuthally by $\cos\theta$ and thus excites pure dipolar fields. The longitudinal field components are obtained from the homogeneous wave equations, and the transverse ones from Maxwell's equations without source terms. The beam excites not only TM modes, but also TE modes have to be added in order to properly fulfill the boundary conditions. This seems to have been omitted in ref.[8], where the restriction to the axial component of the vector potential simplifies matching considerably (only the vector potential and its derivative need to be continuous), but this excludes a longitudinal magnetic field component and hence TE modes.

Matching of all four tangential field components on each layer boundary yields a set of linear equations with an equal number of unknowns. In principle the solution is straightforward but it is complicated in practice as the system is "ill-conditioned" and hence numerical resolution can become (very) inaccurate.

Analytic solution of a system of 4 n linear equations - where n is the number of layers - is generally too complex to be done by hand and has to be done with algebraic computer codes such as Mathematica[45]. Still the results are very lengthy expressions and cannot be simplified easily. Numerical evaluation yields impedances which agree quite well with the previous models for reasonable parameters, but give considerably higher values for the LHC collimators with an extremely small beam hole and a thick wall of very high resistivity.

4.3 Calculation of Wake Functions

To be able to compute wake functions from impedances, we need to know some more basics about impedances.

Transverse impedances must fulfill certain properties [12, p.76], one of which requires the real part of the impedance to be anti-symmetric and the imaginary part to by symmetric.

$$\begin{aligned} \text{Re } Z_m^\perp(\omega) &= -\text{Re } Z_m^\perp(-\omega) \\ \text{Im } Z_m^\perp(\omega) &= \quad \text{Im } Z_m^\perp(-\omega) \end{aligned} \tag{4.12}$$

As a direct consequence of these properties, the sgn-function and the absolut value appear in the expressions. Identifying the cases $+\omega$ and $-\omega$ one can get rid of those functions in some cases, but generally not. (Hint: *Mathematica* and probably

other symbolic packages as well, have certain problems using discontinuous functions, especially in the routines for Fourier transforms. One way to overcome this, is to get rid of possible sgn and abs functions as mentioned before. Note however that one must be extremely careful about the definition of the sign of $\sqrt{-1}$ and how this is treated in the internal routines of the symbolic package.)

The transverse wake function at a time t behind a point charge is the Inverse Fourier transform of the impedance

$$W_m^{\perp}(t) = -\,j \int_{-\infty}^{+\infty} \frac{d\omega}{2\pi}\, Z_m^{\perp}(\omega)\, \exp\left(j\,\omega t\right) . \tag{4.13}$$

Note the additional factor $-\,j$ in the above formula, which describes the mere fact that the transverse force is 90° out of phase with the beam current [12, p.70]. Applying the Inverse Fourier transform to Eq. (4.1) leads to the classical transverse resistive thick wall wakefunction:

$$\begin{aligned} W_{m=1}^{\perp}(t>0) &= \frac{cL}{\pi^{3/2} b^3} \sqrt{\frac{\mu_o \mu_r}{\sigma_c}} \cdot \frac{1}{\sqrt{|t|}} \\ &= \frac{\mu_r\, Z_0\, L\, \delta_0}{\pi\, b^3\, \tau_{rev}} \cdot \sqrt{\frac{\tau_{rev}}{|t|}} \end{aligned} \tag{4.14}$$

Remind yourself that the resistive part $\mathrm{Re}\, Z_m^{\perp}(\omega)$ causes instability for negative resistance and damping for positive resistance, because of:

$$\underbrace{\Delta\Omega \propto j\, Z}_{\substack{\text{complex tuneshift} \\ \text{caused by impedance}}} \qquad \text{and} \quad \underbrace{x, y(t) \propto \exp j(\Omega + \Delta\Omega)t}_{\text{betatron motion}}$$

$$\Longrightarrow \qquad \underbrace{1/\tau}_{\text{growth rate}} = -\mathrm{Im}\,\Delta\Omega = -\mathrm{Re}\, Z \tag{4.15}$$

The complex tuneshift $\Delta\Omega$ is caused by the impedance Z, where $\Delta\Omega$ is directly proportional to Z (this follows from the equations of motion, Z is part of the force on the RHS). From the equations of motion it follows that a negative resistance corresponds to a positive real-valued growth rate $1/\tau$.

An instability in the above sense can be interpreted in frequency domain as follows: Wake fields due to the resistivity of the wall drive the beam unstable at a frequency where a line of the bunch spectrum happens to be in a region of large negative resistance.

Especially the $1/\sqrt{t}$ dependence of the wakefunction accounts for its importance concerning high intensity and/or multi-bunch machines. Due to the slow decay of the fields, successive bunches 'see' each other or even a single bunch may see itself over consecutive turns in the machine. Depending on the phase relation of the kick conveyed by the wake field and the motion of the particle in concern this will lead to amplification or attenuation of the particle betatron oscillation.

A direct consequence of the $1/\sqrt{t}$ dependence are furthermore long computation times in simulations, as there is no straight-forward way of summing up wake contributions over several turns form previous bunches in an efficient way. Fortunately a

smart algorithm for such summations has been found (see 3), that reduces drastically the time needed to execute the necessary summations.

Refer to Figure 4.3 and 4.4 (dashed lines) for plots of the transverse resistive wall impedance and wakefunction in the classical thick wall case.

4.3.1 Transverse resistive wall Impedance and Wakefunction with inductive bypass

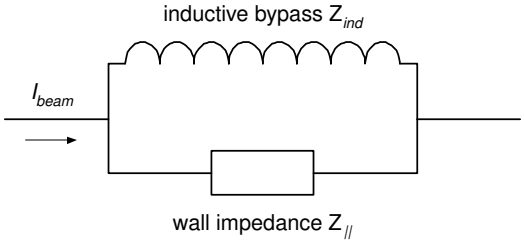

Figure 4.2: *Equivalent circuit to be used for computing the transverse impedance of a pipe of unit length with longitudinal impedance $Z_{\parallel}$ [41]*

First we will shortly recapitulate the concept of inductive bypass as described in [41]. If the wall current finds a path with less resistivity it will certainly take that one, thus lowering the impedance. Ref. [41] shows that such an alternative path acts like an inductance on the beam.

Figure 4.3.1 shows the (longitudinal) equivalent circuit that has to be used for computing the transverse impedance $Z_{\perp,\mathrm{ibp}}$ of a pipe of unit length with longitudinal impedance $Z_{\parallel}$.

$$Z_{\perp,\,\mathrm{ibp}}(\omega) = \frac{2c}{b^2\omega} \cdot \frac{Z_{\parallel} \cdot Z_{ind}}{Z_{\parallel} + Z_{ind}} \tag{4.16}$$

4.3.2 Thick Wall

We are now ready to use the above mentioned equivalent circuit (4.16) to find the transverse resistive wall impedance with inductive bypass for thick walls (wall thickness $t \gg \delta_{skin}$). The longitudinal resistive wall impedance $Z_{\parallel}$ is

$$\begin{aligned} Z^{\parallel}_{m=1}(\omega) &= (1 + j\ \mathrm{sgn}\,\omega)\ \frac{1}{\delta_{skin}\,\sigma_c}\ \frac{L}{2\pi b}\,, \\ \delta_{skin}(\omega) &= \sqrt{\frac{2}{\sigma_c \mu_0 \mu_r |\omega|}}\,, \end{aligned} \tag{4.17}$$

where δ_{skin} is the skin depth, L indicates the length over which the impedance is defined, b is the vacuum chamber radius, μ_0 and μ_r denote the free space and relative permeability respectively and σ_c designates the conductivity of the vacuum chamber wall material.

We take directly the inductive bypass given in Ref. [41], which has a constant inductance of value $\mu_0/4\pi$, namely

$$Z_{ind}(\omega) = j\,\omega \cdot \frac{\mu_0}{4\pi} \cdot L\,, \tag{4.18}$$

where the same definitions as above apply.

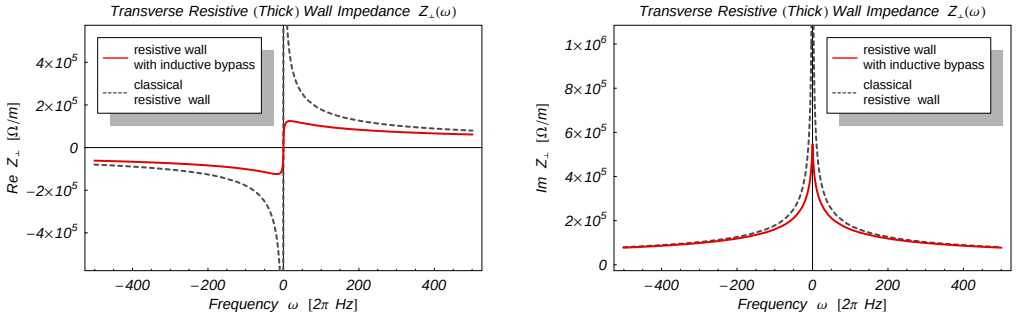

Figure 4.3: *Real and imaginary part of the transverse resistive thick wall impedance in the classical case (dashed) and with inductive bypass (solid)*

The next step is to insert these expressions (4.17–4.18) into (4.16) in order to get a formula for the impedance with inductive bypass, which leads us to

$$Z^{\perp}_{m=1,\,\mathrm{ibp}}(\omega) = (1 + j\ \mathrm{sgn}\,\omega)\ \frac{c\,\mu_0\,L}{2\,\pi\,b^2}\ \frac{1}{-\,j + \mathrm{sgn}\,\omega\left(1 + b\sqrt{\frac{\sigma_c\,\mu_0}{2\,\mu_r}}\ \sqrt{|\omega|}\right)}\,, \tag{4.19}$$

which is an already simplified expression where the properties (4.12) of the impedance are retained. Finally, to keep better track of the general form we introduce the constants c_1 and c_2,

$$Z^{\perp}_{m=1,\,\mathrm{ibp}}(\omega) = c_1 \cdot \frac{(1 + j\ \mathrm{sgn}\,\omega)}{\mathrm{sgn}\,\omega - j + c_2\ \mathrm{sgn}\,\omega\ \sqrt{|\omega|}}\,,$$

$$\begin{aligned} c_1 &= \frac{c\,\mu_0\,L}{2\,\pi\,b^2} = \frac{Z_0\,L}{2\,\pi\,b^2}\,, \\ c_2 &= b \cdot \sqrt{\frac{\sigma_c\,\mu_0}{2\,\mu_r}} = \frac{b}{\mu_r\,\delta_0\,\sqrt{\omega_0}}\,. \end{aligned} \tag{4.20}$$

Figure 4.3 shows the impedance with inductive bypass. The important difference is immediately visible:

$$\begin{aligned} \lim_{\omega\to 0}\ &\mathrm{Re}\ Z_{\perp,\,\mathrm{ibp}}(\omega) = 0 \\ \lim_{\omega\to 0}\ &\mathrm{Im}\ Z_{\perp,\,\mathrm{ibp}}(\omega) = \text{const.} = c_1 \\ \lim_{\omega\to\pm\infty}\ &Z_{\perp,\,\mathrm{ibp}}(\omega) = 0 \end{aligned} \tag{4.21}$$

For $\omega \to 0$ the imaginary part of the impedance approaches a finite value and what is even more important, the real part goes to zero for $\omega \to 0$. The effect is that the (multi-) bunch mode m which is closest to the origin (usually modes $0, -1, \ldots$) becomes stabilized now, and a higher mode, which is much harder to drive, will become the most unstable one. Hence, overall the beam will be more stable.

In order to find the wake function we have to apply the inverse Fourier transformation on Eq. (4.20). Although expression (4.20) seems to be harmless, the transformation is not straightforward, rather we have to split the impedance (4.20) into

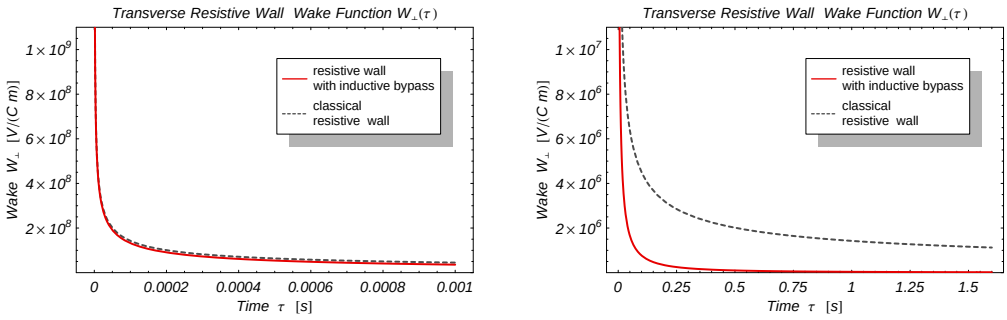

Figure 4.4: *Transverse resistive thick wall wakefunction in the classical case (dashed) and with inductive bypass (solid) for different time scopes*

two terms, which can be done by extending the denominator with a pseudo-complex conjugate form. We get

$$Z^{\perp}_{m=1,\,\mathrm{ibp}}(\omega) = -c_1\,\frac{2}{c_2^2\,\omega + 2\,j} \;+\; c_1\,c_2\,\frac{(\omega + j\;|\omega|)\;\sqrt{|\omega|}}{c_2^2\,\omega^2 + 2\,j\,\omega}\,. \tag{4.22}$$

Using this technique we can perform the inverse Fourier transformation on the two terms independently. The first term gives zero, only the second term contributes to the result (for $t > 0$):

$$W^{\perp}_{m=1,\,\mathrm{ibp}}(t>0) = \sqrt{\frac{2}{\pi}}\,\frac{c_1}{c_2\,\sqrt{|t|}} \;-\; \frac{2\,c_1}{c_2^2}\,\exp\left[\frac{2}{c_2^2}\,|t|\right]\cdot\left(1 - \mathrm{Erf}\,\frac{\sqrt{2\,|t|}}{c_2}\right) \tag{4.23}$$

After inserting the constants c_1 and c_2 we arrive at the final result, the transverse resistive thick wall impedance with inductive bypass,

$$\begin{aligned} W^{\perp}_{m=1,\,\mathrm{ibp}}(t>0) = {} & +\frac{cL}{\pi^{3/2}b^3}\,\sqrt{\frac{\mu_o\mu_r}{\sigma_c}}\cdot\frac{1}{\sqrt{|t|}} \\ & -\exp\left[\frac{4\mu_r}{b^2\sigma_c\mu_0}\,|t|\right]\;\frac{2cL\mu_r}{b^4\pi\sigma_c}\;\cdot\left(1 - \mathrm{Erf}\,\sqrt{\frac{4\mu_r}{b^2\sigma_c\mu_0}\,|t|}\right)\,. \end{aligned} \tag{4.24}$$

Thus we have found an expression where the first term reveals the classical result plus an additional term which defines the correction to it. This correction is active over the whole range $t \in [0, \infty]$, but at the limit $t \to 0$ it approaches a finite value, therefore it does not change the overall value of the wakefunction, which approaches infinity there. On the other hand, in the limit $t \to \infty$, the correction term vanishes. Thus the intermediate range is most interesting, where the correction term gives its dominant contribution.

Figure 4.4 shows the behavior of the wakefunction in comparison to the classical result. For small time distances the difference is marginal, but as soon as the time distance grows the effect of the inductive bypass becomes visible: The wake falls off much faster than $1/\sqrt{t}$ causing less effect on succeeding bunches. The course of the two wake functions (classical and with inductive bypass) is better seen in a logarithmic plot, see figure 4.5.

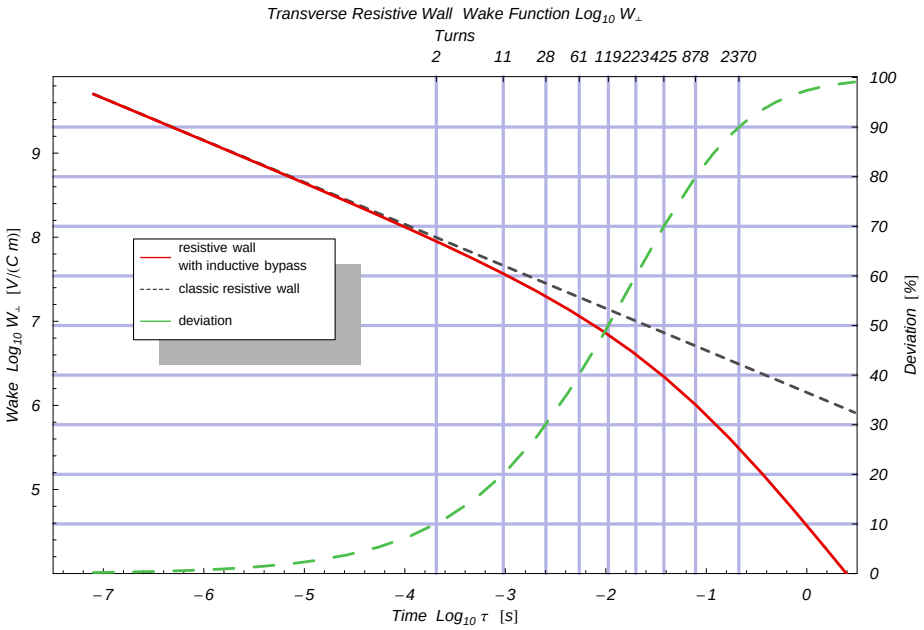

Figure 4.5: *Transverse resistive thick wall wakefunction in the classical case (dashed) and with inductive bypass (solid) in logarithmic scale. The relative difference is also drawn (long dashed).*

Table 4.1: *Parameters used for plotting Figures 4.3–4.6*

Symbol	Value	Quantity
b	$1 \cdot 10^{-2}\ m$	tube radius
σ_c	$18 \cdot 10^{8}\ (\Omega m)^{-1}$	conductivity
c	$3 \cdot 10^{8}\ ms^{-1}$	speed of light
L	$1\ m$	length for impedance definition
μ_0	$4\pi\, 10^{-7}\ Vs(Am)^{-1}$	permeability of free space
μ_r	1	relative permeability $\mu_r = \mu/\mu_0$
$\tau_{rev,\,LHC}$	$88.9245\, 10^{-6}\ s$	revolution time

4.3.3 Thin Wall

In the case of a thin wall, wall thickness $t_w < \delta_{skin}$, the same exercise can be conducted: We start with a simple thin wall formula, that can be found e.g. in [1]. This formula describes the physical situation, that all the wall current flows in the wall of cross-section $2\,\pi\,b\,t_w$:

$$Z^{\perp}_{m=1}(\omega) = \frac{c\,L}{\pi\,b^3\,\sigma_c\,t_w\cdot\omega} \tag{4.25}$$

Again c denotes the speed of light, L indicates the length over which the impedance is defined (e.g. $L = 2\pi R =$ the circumference), b is the vacuum chamber radius and σ_c designates the conductivity of the vacuum chamber wall. The vacuum chamber has the wall thickness t_w.

It is already stated in the above reference, that this expression is only valid for sufficiently low frequencies, $|\omega| < 2/\left(\sigma_c\,\mu_0\,\mu_r\,t_w^2\right)$. The introduction of the inductive bypass, by applying (4.16), rectifies (4.25) in the sense, that it becomes meaningful over the whole range of frequencies. Inclusion of the inductance from Ref. [41] gives

$$\begin{aligned} Z^{\perp}_{m=1}(\omega) &= \frac{c\,\mu_0\,L}{2\,\pi\,b^2}\cdot\frac{1}{\frac{1}{2}\,b\,t_w\,\sigma\,\mu_0\cdot\omega - j}\,, \\ &= \frac{Z_0\,L}{2\,\pi\,b^2}\cdot\frac{1}{\frac{b\,t_w}{\delta_0^2\,\mu_r}\,\frac{\omega}{\omega_0} - j}\,, \end{aligned} \tag{4.26}$$

which is a known thin metal wall formula, derived in various forms already early in the literature [47, 26, 48], but is not often used, for reasons unknown to the author.

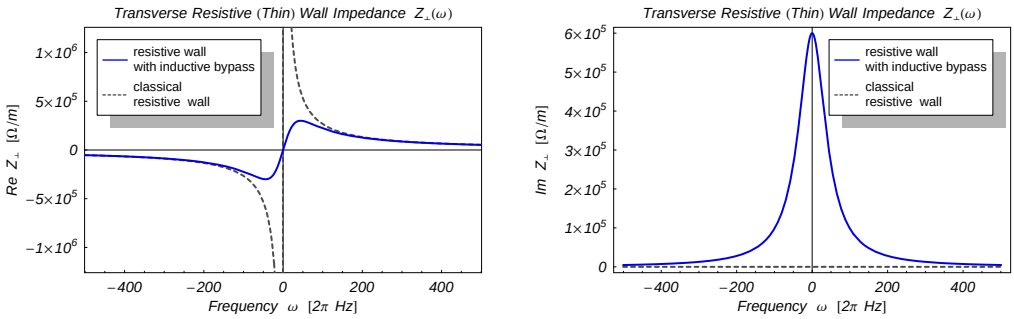

Figure 4.6: *Real and imaginary part of the transverse resistive thin wall impedance in the classical case (dashed) and with inductive bypass (solid)*

Applying the inverse Fourier transformation on this expression is straightforward. We get the resistive thin wall wakefunction

$$\begin{aligned} W^{\perp}_{m=1,\,\mathrm{ibp}}(t>0) &= \frac{c\,L}{\pi\,b^3\,\sigma_c\,t_w}\cdot\exp\left[-\frac{2}{b\,t_w\,\sigma_c\,\mu_0}\,|t|\right]\,, \\ &= \frac{\mu_r\,Z_0\,L\,\delta_0^2\,\omega_0}{2\,\pi\,b^3\,t_w}\cdot\exp\left[-\frac{\mu_r\,\delta_0^2}{b\,t_w}\,\omega_0\,|t|\right]\,. \end{aligned} \tag{4.27}$$

4.4 Comparison of the Models

The heuristic inclusion of the "inductive bypass" comes remarkably close to the result by Burov and Lebedev as can be seen qualitatively in Fig.4.8. This is why stability estimates established with (4.7) are in good agreement with results obtained with the Burov-Lebedev formula.

However, the LV approach has limitations that are inherent in transmission line theory. Hyperbolic tangents appear, which obviously refer to further assumptions that are not specified. This becomes apparent for the copper coated LHC collimator, where the LV result significantly differs from the BL impedance (see Fig.4.9). The BL approach is more rigid from the beginning and the limits of applicability are specified.

As can be seen from Figs. 4.8 and 4.9, the real part of the transverse impedance is largely reduced. Usually the condition $\delta_{\text{skin}} \leq b$ holds for all frequencies in consideration. The lower the frequency the larger the skin depth. Pair this with small aperture and we easily arrive at the condition $\delta_{\text{skin}} \gg b$, as in the case of the LHC collimators. Then the beam does not see the induced currents at the distance b any more, but instead sees them over the range $[b, \delta_{\text{skin}}]$, thus the effective aperture is in the order of $\delta_{\text{skin}} \gg b$ in this case [7].

The imaginary part at low frequencies is dominantly determined by the effect of the electric dipole. It is simply the image of the beam on the surface of the vacuum chamber. The surface is at fixed distance b, thus $\operatorname{Im} Z$ approaches a constant value for $\omega \to 0$. The magnetic dipole does not contribute at low frequencies, because the related electric field goes to zero, $j_z = \sigma E_z = \partial A_z / \partial t \propto \omega \to 0$; i.e. the chamber does not respond to the magnetic dipole.

Fig. 4.8 shows the impedance of an uncoated LHC collimator. At 8 kHz the real part of the impedance is reduced by a factor 100, which is consistent with the picture of effective aperture just explained.

Results for a copper coated LHC collimator, with 5 μm coating thickness, are portrayed in Fig. 4.9. Pay attention to the fact that in this case the real part of the impedance is increased below 1 MHz and reduced above as compared to the uncoated example. At high frequencies the induced current is more and more confined to the copper layer, hence the impedance is reduced. At low frequencies similarly a significant part of the current will flow in the copper layer with less resistivity. Then the effective aperture is reduced, thus the real part of the impedance increases accordingly. These results are consistent with HFSS simulations [39].

Note that each derivation presented results in only one formula from zero frequency up to $\omega \ll \beta c / b$, without the need to distinguish between cases where the skin depth is smaller or bigger than the wall thickness. In particular the characteristics of all presented impedances converge for the "standard" parameter range ($d < b$) (see [25]).

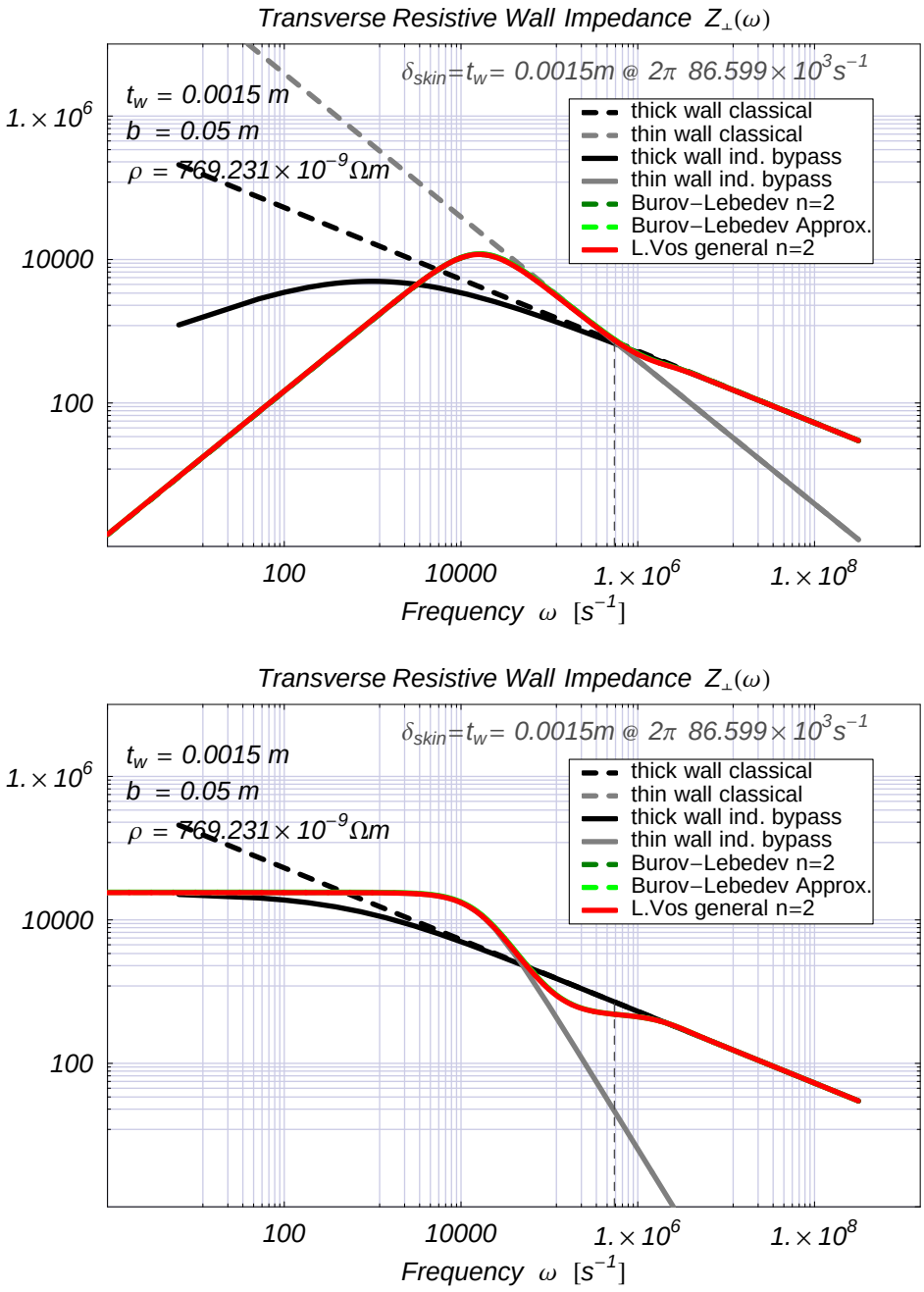

Figure 4.7: *Real and imaginary part of various different transverse resistive wall impedances for "standard"beam pipe parameters* $t_w = 1.5\text{mm}, b = 5\text{cm}$

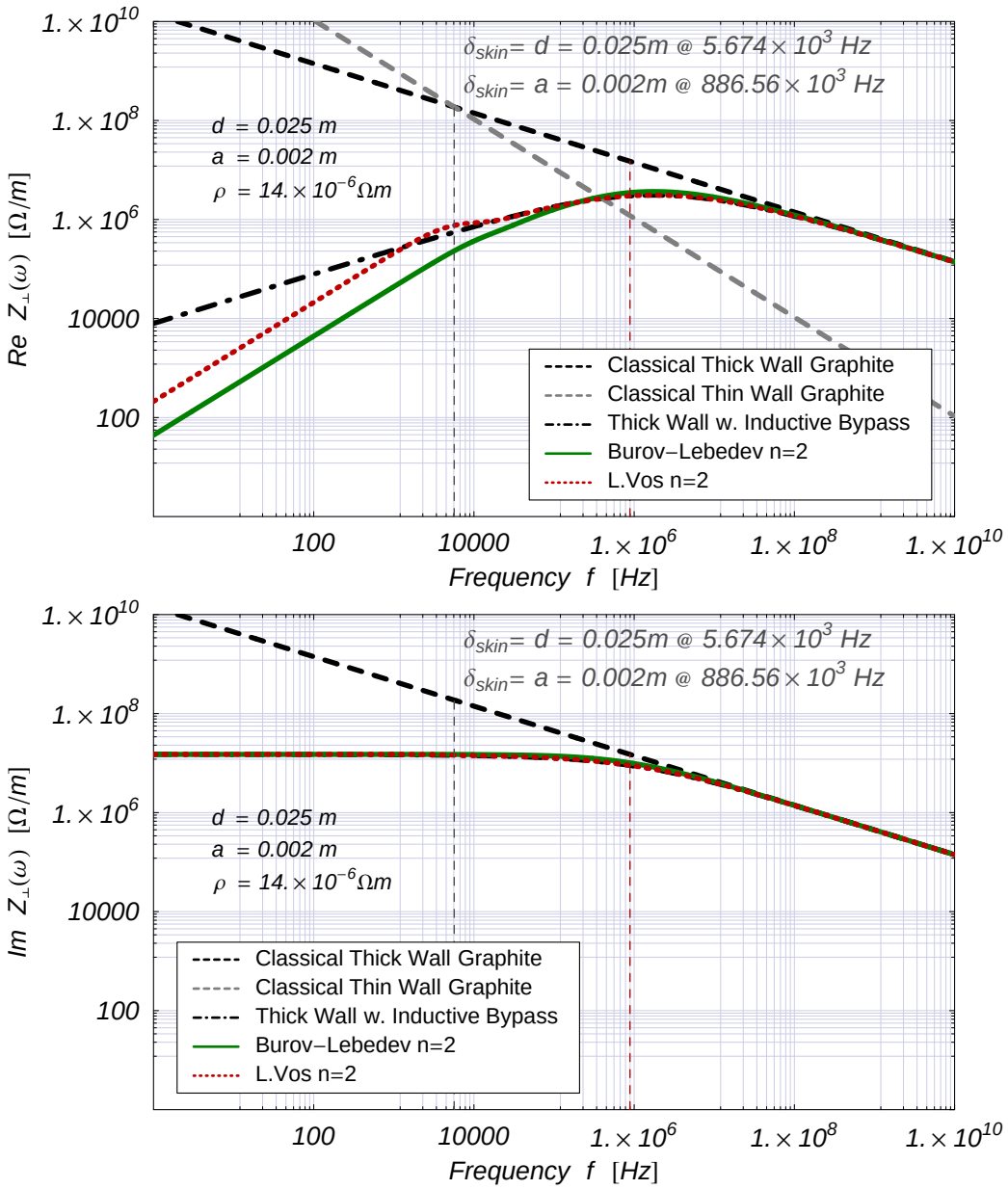

Figure 4.8: *Real and imaginary part of different formulae for the transverse resistive wall impedance for the case of an LHC collimator, $L = 1\,m$.*

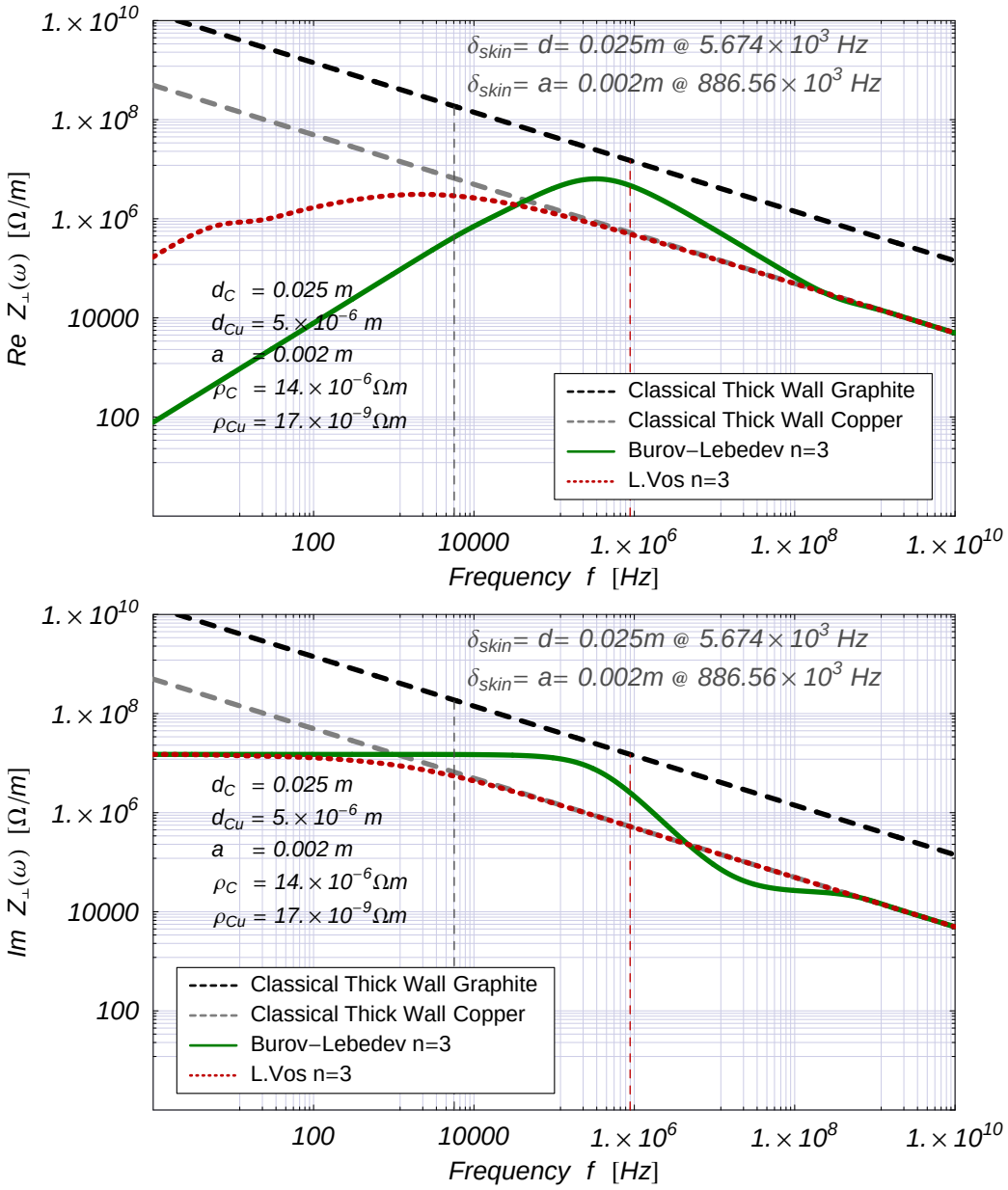

Figure 4.9: *Real and imaginary part of the transverse resistive wall impedance with copper coating (5 μm) for the case of an LHC collimator, $L = 1$ m.*

Chapter 5

SPS simulation and measurements

The validity of simulation results can be verified by comparison with experimental data. The goal of this thesis is mainly to study multi-bunch instabilities, in particular when caused by the resistive wall effect. To benchmark the simulation code, measurements of growth rates and tune shifts in both transverse planes were carried out in the SPS in 2003.

After the shutdown of LEP (Large Electron-Positron collider) in November 2000 and before the startup of LHC in 2007, the PS and SPS are the only high-energy accelerators remaining operational at CERN. The SPS was chosen because it is known to suffer dominantly from the resistive wall instability with the "Fixed Target" (FT) beam if no counter measures are taken.

In this chapter the results of resistive wall growth rate measurements in the SPS will be presented and compared to simulation results. Furthermore simulation results for the planned LHC collimator test in the SPS will be shown and discussed.

5.1 The SPS in general terms

Figure 5.1: *A view of the SPS tunnel.*

The Super Proton Synchrotron (SPS) is a multi-purpose circular accelerator. It was built originally to accelerate protons and continues to do so, but it has also operated as a proton-antiproton collider and as an electron/positron injector for LEP and has been operated with heavy ions as well.

From 2007 onwards it will serve as the injector for the LHC, accelerating 26 GeV/c protons from the PS to 450 GeV/c before extraction to LHC. Many changes have been or will be done to the existing SPS which are necessary before it can deliver the high brightness proton beams required by the LHC.

The general beam optics parameters of the SPS are summarized in Tab. 5.1 for injection and top energy. Some of these parameters change with special beam setups. Note that the PS can deliver a 14 GeV/c beam for injection to the SPS as well, which means to stay below transition. This is used for the Fixed Target (FT) beam.

Table 5.1: *SPS general parameters*

Parameter	Symbol	Unit	Value
Momentum at injection	$p_{\text{inj.}}$	[GeV/c]	(14) 26
Momentum at extraction	$p_{\text{extr.}}$	[GeV/c]	450
Machine circumference ($= 2\pi R$)	C	[m]	6911.5
Machine radius	R	[m]	1100.0
Revolution frequency at injection	f_0	[Hz]	43347.3
Revolution frequency at extraction	f_0	[Hz]	43375.4
Revolution time	T_0	[μs]	23.07
Lattice type			FODO
Number of lattice cells per arc			
Phase advance per cell	Φ	[°]	90
Dipole field at injection	B	[T]	0.120
Dipole field at extraction	B	[T]	2.025
Bending radius	ρ	[m]	741.257
Dipole length	l	[m]	6.26
Tunes Fixed Target (FT) Beam Q_H/Q_V			26.64 / 26.59
Tunes LHC Beam Q_H/Q_V			26.185 / 26.13
Maximum β-function H/V	$\beta_{\text{max.}}$	[m]	107.5/108.6
Minimum β-function H/V	$\beta_{\text{min.}}$	[m]	19.5/19.3
Average β-function ($= R/Q$)	$\langle\beta\rangle$	[m]	41.29/41.36
Gamma transition FT Beam	γ_T		23.23
Gamma transition LHC Beam	γ_T		23.83
Momentum compaction	α_c		1.856×10^{-3}
Harmonic number	h		4620
RF Frequency	f_{RF}	[MHz]	200.0
RF Voltage at injection	V_{RF}	[MV]	0.6-0.8
RF Voltage at extraction	V_{RF}	[MV]	3.0
Synchrotron tune	Q_s		$3 \cdot 10^{-3}$
Trans. emittance	$\epsilon_{H,V}$	[μm]	<10 / <7.5
Long. emittance	ϵ_L	[eVs]	0.2

The vacuum chamber dimensions and material properties become important for the resistive wall effect. The major part of the machine is composed of stainless steel vacuum chambers with oval cross sections. The exact dimensions are given in Fig. 5.2. The lengths of chambers with these corresponding different geometries were obtained using MADX, the numbers are given in Tab. 5.2. Note that the SPS has a rather flat vacuum chamber (with V/H ratios from 1/3 to 1/4 in the bending sections). This asymmetry enhances effects in the vertical, compared to the horizontal plane.

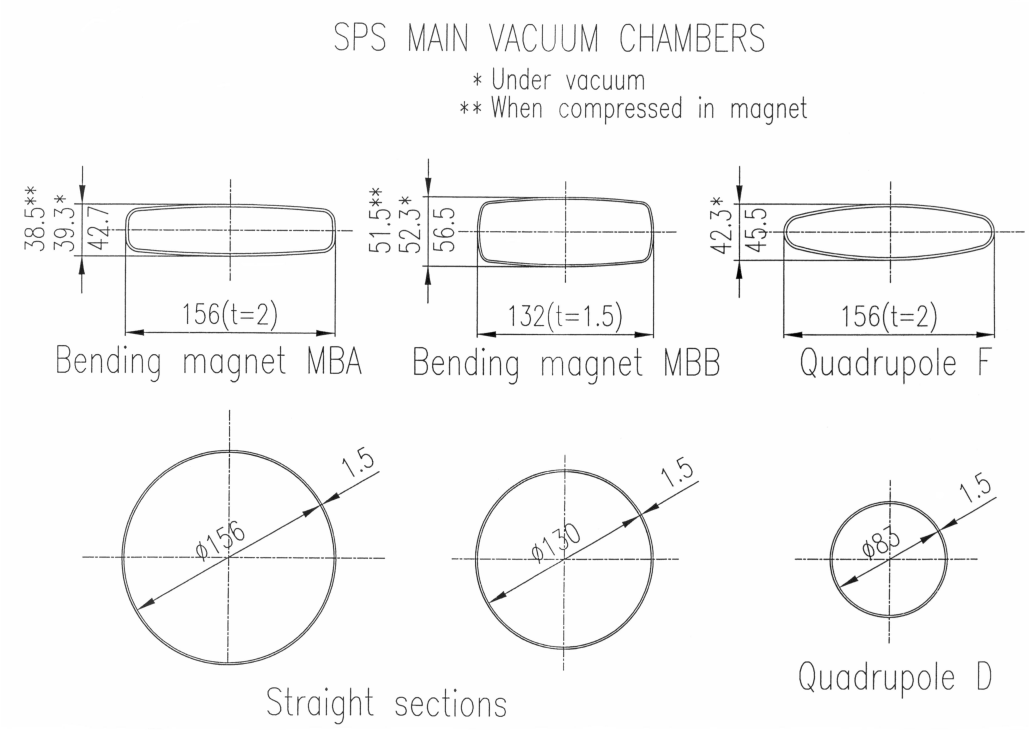

Figure 5.2: *The geometry of the SPS main vacuum chambers. The dimensions are given in millimeters. Note the variation of the vertical dimensions when the tubes are evacuated and compressed due to the magnetic fields of the dipole. The vacuum chamber thickness is denoted by t.*

Table 5.2: *SPS vacuum chamber parameters.* b_x *and* b_y *are the inner vacuum chamber radii, given in millimeters and extracted from the technical drawing given in Fig. 5.2. The lengths of the different section have been obtained with MADX and the proper SPS lattice file. The material of all major elements is assumed to be stainless steel with a conductivity of* $\sigma_{Stainless\ Steel} = 1.4 \cdot 10^6\ (\Omega m)^{-1}$.

Section	b_x [mm]	b_y [mm]	Length [m]	Percentage
Bending Magnets MBA	76.00	17.65	2253.6	32.61
Bending Magnets MBB	64.50	24.65	2403.8	34.78
Quadrupoles F	76.00	19.15	338.1	4.89
Quadrupoles D	41.50	41.50	338.8	4.90
Drift section type A	78.00	78.00	466.1	6.74
Drift section type B	65.00	65.00	497.2	7.19
Rest (Pick-Ups, Sextupoles, ...)			613.9	8.88

Table 5.3: *Fixed Target beam in CERN SPS*

Parameter	Symbol	Unit	Value
Momentum at injection	p	[GeV/c]	14
Revolution time	T_0	[μs]	23.07
Tune	Q_H		26.64
Tune	Q_V		26.59
Gamma transition	γ_T		23.23
Maximum number of batches			2
Number of bunches per batch			2100
Bunch Intensity	N_p		$4.8 \cdot 10^{9}$
Total Intensity	$N_{p,tot.}$		$1.0 - 2.0 \cdot 10^{13}$
Batch spacing		[ns]	1050
Bunch spacing		[ns]	5
Full bunch length		[ns]	4
Trans. emittance	$\epsilon_{H,V}$	[μm]	<10 / <7.5
Long. emittance	ϵ_L	[eVs]	0.2

5.2 Fixed Target Beam

The fixed target (FT) beam in the SPS shows dominantly the effect of the resistive wall. This is in particular true when the vacuum chamber wall has been conditioned before by scrubbing runs, such that the electron-cloud effect is insignificant. The main parameters of the so-called "SFTPRO" (SPS Fixed Target Proton) beam are summarized in Tab. 5.3.

The SFTPRO beam allows one or two batches of 2100 bunches each to be accelerated in the machine. This refers to $1 - 2 \cdot 10^{13}$ total particle intensity. The bunch spacing is $5ns$, that means that consecutive buckets are filled.

For the measurements (also called MD = machine development), the MD segment of the SPS supercycle was used. The timing set-up of the MD Fixed Target beam is summarized in Tab. 5.4. The SPS supercycle "SC 400" has an overall length of 16.8 s. All data were taken in the MD segment which starts at 11.225 s within that cycle.

5.3 Measured Resistive Wall Instability

In 2003, three days of machine development (MD) in the SPS were foreseen, where it was planned to measure multi-bunch growth rates and tune shifts. The MD was coordinated with the AB/RF group, who did tests on the transverse damper system in the SPS.

Water-leaks and problems with the data-acquisition reduced the time of actual possible MD time to one long afternoon. Particularly we could only measure with one BPM (beam position monitor) and not, as foreseen, with several around the machine. This limits the capabilities of data analysis dramatically, and does for example not

Table 5.4: *Timing configuration of the MD SFTPRO beam in SPS*

	time in super-cycle [ms]	time in MD segment [ms]	Number of Turns
MD segment start	11225	0	0
(Feedback Off – 1 batch)	11225	0	0
Injection 1^{st} batch	11225	0	0
Q_H/Q_V measurement (1 batch)	11225	0	0
(Feedback On – 1 batch)	11228	3	129
	11230	5	215
	11232	7	301
(Feedback Off – 2 batches)	11225	0	0
Injection 2^{nd} batch	12425	1200	52017
Q_H/Q_V measurement (2 batches)	12425	1200	52017
(Feedback On – 2 batches)	12428	1203	52146
	12430	1205	52232
Beam dumped	11225	1658	71870
MD segment end	15875	4650	201565

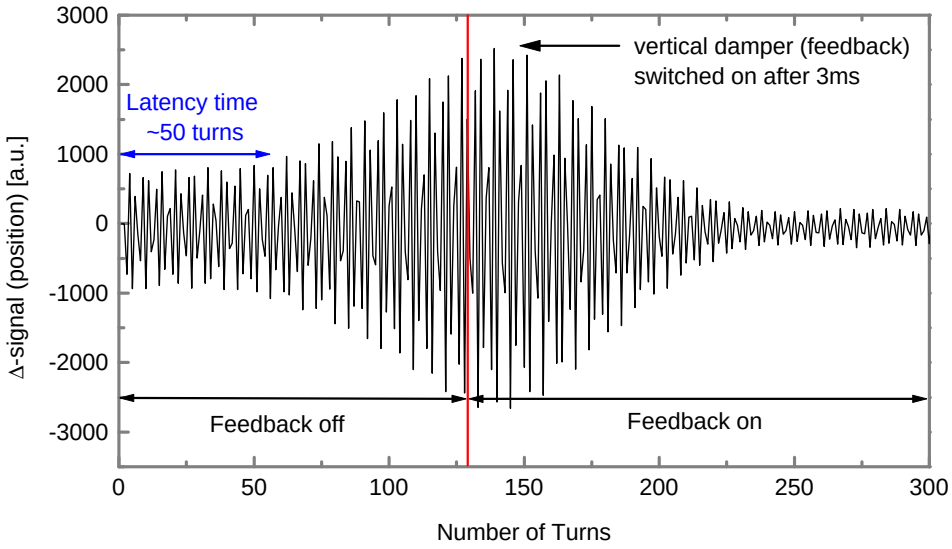

Figure 5.3: *Typical BPM readings for growth rate measurements in the SPS in the vertical plane for parameters given in Tab. 5.3. The signal starts directly at injection, where the feedback is switched off. After 3 ms (129 turns) the transverse damping system is switched on again. There is a latency period of about 50 turns after injection (no growth).*

Table 5.5: *Measurement results, SPS Fixed Target beam*

1 Batch (2100 bunches)	Growth rate $2\pi/\tau$ [turns]	Coherent tune Q
Vertical Plane	77 ± 4	0.5927 ± 0.0079
Horizontal Plane	183.5 ± 23.5	0.6180 ± 0.0029

allow to study coupled-bunch modes. Nevertheless growth-rates and coherent tunes could be determined and using the same kind of analysis on the simulated data, the results can be compared.

The machine was in the standard "SFTPRO" setup for the fixed target beam, refer to Tab. 5.3 for parameters. The MD segment of the SPS supercycle ("SC 400") was used. For the timing configuration refer to Tab. 5.4. The only change we requested for the MD, was the possibility to have one batch (2100 bunches) or two batches (4200 bunches) in the machine.

The measurement with 1 batch (2100 bunches) was carried out as follows: BPM was set to take data on the first 8192 turns after injection. The pick-up was gated such that it saw only one bunch. This bunch was one of the bunches in the second half of the batch, the exact timing parameter was not known. (This will become an issue in the comparison to simulated data, see below Sec. 5.5). The SPS BCT 3 (beam current transformer) took data from injection until the beam was dumped 1658 ms afterwards. The transverse dampers (either V or H, or both) were turned off at injection and switch on 3,5 and 7 ms after injection, respectively. Typical BPM data readings looked like the one depicted in Fig. 5.3.

A more detailed view on the data analysis is shown in Fig. 5.5. We measured growth rates for 1 batch (total intensity $1{\cdot}10^{13}$) in the machine of $\tau_{H,\text{turns}} = 183.5 \pm 23.5\,\text{turns}$ and $\tau_{V,\text{turns}} = 77 \pm 4\,\text{turns}$.

Please note that these are *amplitude* growth rates measured on one bunch. This is not the same as analytically determined *mode* growth rates. We will come back to this issue later in the comparison to simulated data, see Sec. 5.5.

There is a latency period of 50 turns visible after injection. In the framework of coupled-bunch modes this can be explained as follows: At injection the offsets of the bunches are such that they they form a superposition of unstable and stable modes. Stable modes will be damped and unstable modes will grow. Therefore, we expect to see zero amplitude growth if decreasing stable modes approximately compensate the unstable ones in the transient time period.

Unfortunately we could not measure with varying intensities, therefore no tune slope could be established. The measured coherent tunes were $Q_H = 0.6180 \pm 0.0029$ and $Q_V = 0.5927 \pm 0.0079$.

There was very little time to measure with as second batch as well. BPM was now set to take data on the first 1024 turns after injection of the second batch. The pick-up was gated such that it again saw only one bunch. This bunch was one of the bunches in the second half of the batch, the exact timing parameter was again not known. The BCT took continuously data. Contrary to the previous setting for

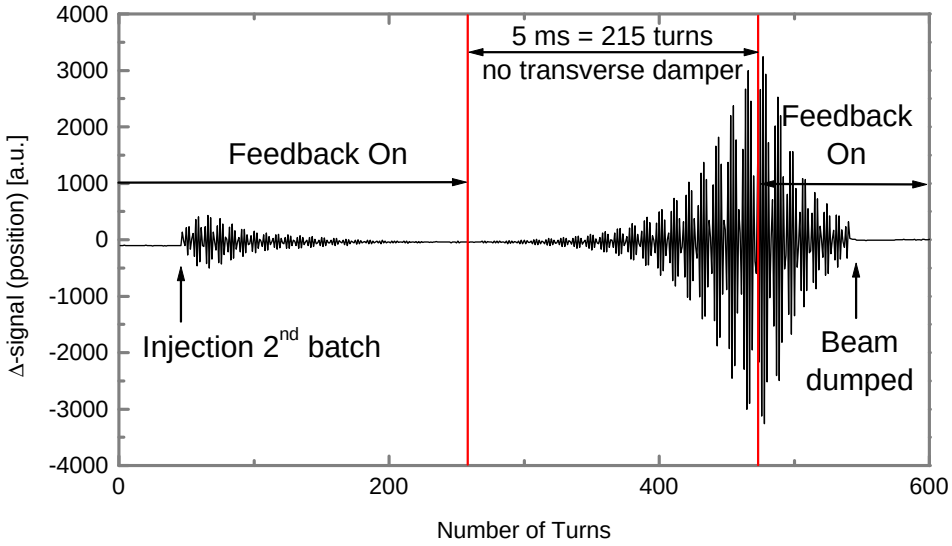

Figure 5.4: *BPM reading for growth rate measurement in the SPS in the vertical plane with 2 batches for parameters given in Tab. 5.3. The injection of the 2nd batch at turn 43 is visible, the feedback is still on at this stage. 5 ms later the damper is turned off and we see immediate growth arising from the noise level. After further 5 ms the feedback is switched on again.*

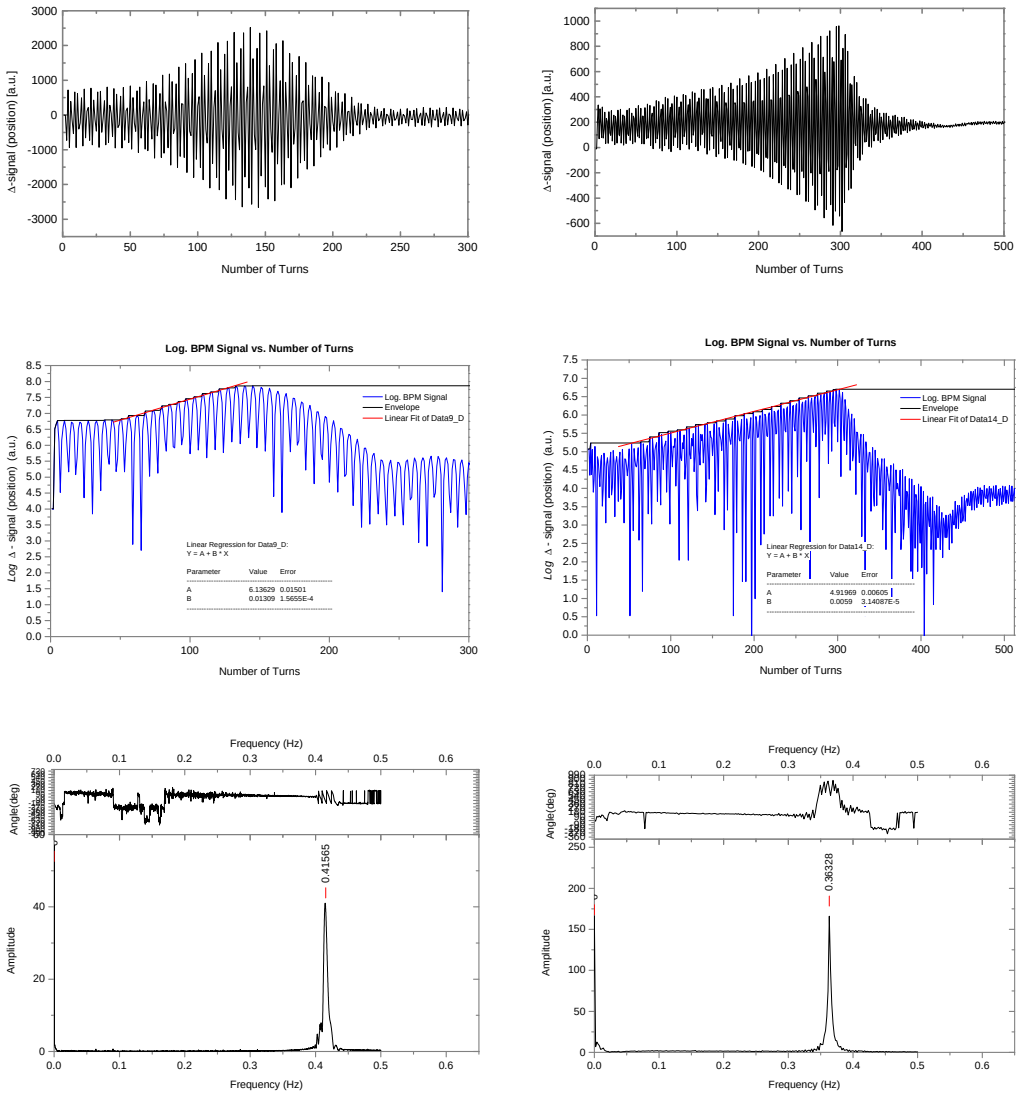

Figure 5.5: *Analysis of the SPS measured data (1 batch) in the vertical (left) and horizontal (right) plane. From top to bottom: BPM signal, logarithmic BPM signal with linear fit on its envelope (= amplitude growth rate) and finally FFT spectrum. The signal starts directly at injection, where the feedback is switched off. After 3 ms (129 turns) the transverse damping system is switched on again in the vertical plane. In the horizontal plane it is switched on after 7 ms (301 turns).*

Table 5.6: *Simple SPS Fixed Target beam simulation model*

Interaction Point	Location [°]	β_x [m]	β_y [m]	μ_x [rad]	μ_x [rad]
Injection and BPM	0	103.39	103.93	0	0
Accelerating Cavity	180	41.2913	41.3689	13.32	13.295
Resistive Wall Impedance	185	41.2913	41.3689	13.69	13.6643

one batch, the transverse dampers (V or H) were working at injection of the second batch. 5 ms afterwards, the feedback (either V or H) was switched off. Another 5 ms later the dampers were powered again. One successful BPM data reading with 2 batches looked like the one depicted in Fig. 5.4. A proper measurement with the second batch was not possible, therefore no result will be presented.

However, Fig. 5.4 shows some interesting physics. First, there is no obvious latency period recognizable at the injection of the second batch, rather there is immediate growth which is then counteracted by the feedback. This indicates that we obviously hit an unstable mode directly at injection.

After the feedback has damped any oscillations we can further see that the instability rises from the noise level. It is very important to retain this behavior. Not the injection oscillations drive the beam unstable, instability already arises from noise. However small the initial amplitudes, the beam will always become unstable if no countermeasures are taken.

5.4 SPS Simulation Model

To simulate the FT beam we use the general parameters of the SPS given in Tab. 5.1. The beam parameters of the FT beam (bunch pattern, bunch intensities, tunes) are given in Tab. 5.3. Refer to Chap. 3 for more details on the simulation process.

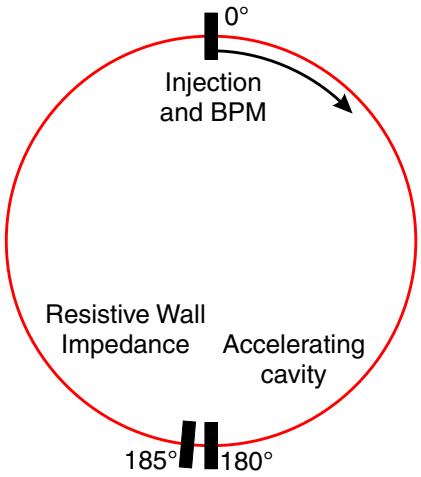

Figure 5.6: *SPS simulation model.*

A simple ring consisting of 3 elements is used, see Fig. 5.6. The first element is the machine start, were injection occurs and also where we measure the bunch positions on consecutive turns. The second element is the accelerating cavity, which acts on the longitudinal coordinates, which will not be considered in this study. But of course an energy spread will also have an effect on the transverse coordinates as we use an energy-dependent phase-advance in the equations of motion. The third, and most important element is the resistive wall IP (interaction point). Here the bunches see the concentrated effect of the distributed SPS vacuum chamber wall, the parameters are given in

Tab. 5.2. The wall has been assumed to be made of stainless steel with a conductivity of $\sigma = 1.4 \cdot 10^6\ (\Omega m)^{-1}$ all around the machine. The simulation code automatically computes and uses the Yokoya factors, which take into account the asymmetry of the vacuum chamber geometry.

The location, beta values and phase advance for each element is given in Tab. 5.6. For the resistive wall impedance we assume the average beta value of the machine, which is a reasonable choice regarding the allocation of its effect all around the machine. Between IPs a linear phase advance is presumed.

As starting conditions we choose to inject bunches with a fixed offset of $x, y =$ 0.1 mm and zero deflection angle $x', y' = 0.0$ rad.

Resistive Wall Turn Memory Another important parameter in the simulation is the resistive wall memory, that is the number of turns over which we have to sum the wake contributions from previous turns. It is given by the time τ_{mem} (or equivalently the distance $D = c \cdot \tau_{\mathrm{mem}}$, with c the speed of light) that the fields need to penetrate the vacuum chamber wall. It can be estimated by the formula from [11, Eq. (12)], which follows from equating two wake field expressions, one describing the $1/\sqrt{D}$ behavior (for small D) and the other one describing the exponential decay $\exp(-D)$ (large D) of the wake

$$x\, e^{-2x} = \frac{t}{\pi r b}, \quad \text{where } \; x = \pi\, \frac{\delta_0^2}{r\, b\, t}\, \left|\frac{D}{C}\right|. \tag{5.1}$$

Here t denotes the wall thickness and b the vacuum chamber inner radius, δ_0 the skin depth at the revolution frequency and C the circumference of the accelerator. The parameter r is defined as $r = 1 + b^2/d^2$ for a perfect magnet and $r = 1 - b^2/d^2$ for a perfect conductor at radius $d > b + t$.

Unfortunately, using this approach the solution is not unique: We get two points of intersection using Eq. 5.1. In the vertical plane with $b \approx 22.5\,\mathrm{mm}$, the first solution corresponds to 0.1 turns and the other one to 18 turns. Comparison of simulation results with the measurement basically indicate to rule out the first solution.

A second method to estimate the required memory comes from the decay length (in number of turns) given in the same reference [11, Eq. (11)],

$$\frac{b\, t\, r}{\pi\, \delta_0^2}. \tag{5.2}$$

This expression yields a decay length of 7 turns.

There is strong argument for using a higher number of turns for the resistive wall memory: The resistive wall impedance models described in Chap. 4 were especially developed to improve the predictive power for low frequencies ω. Low frequencies correspond to long periods in time domain and thus the models should be correct also if we include the wake contributions for a large number of turns. In that sense, only summation over a too small number of turns should alter the simulation results.

Hence we will show the results obtained with the turn memory set to

$$\tau_{\mathrm{mem}}/T_0 = 30\,\mathrm{turns}, \quad \text{where } T_0 \text{ revolution time.}$$

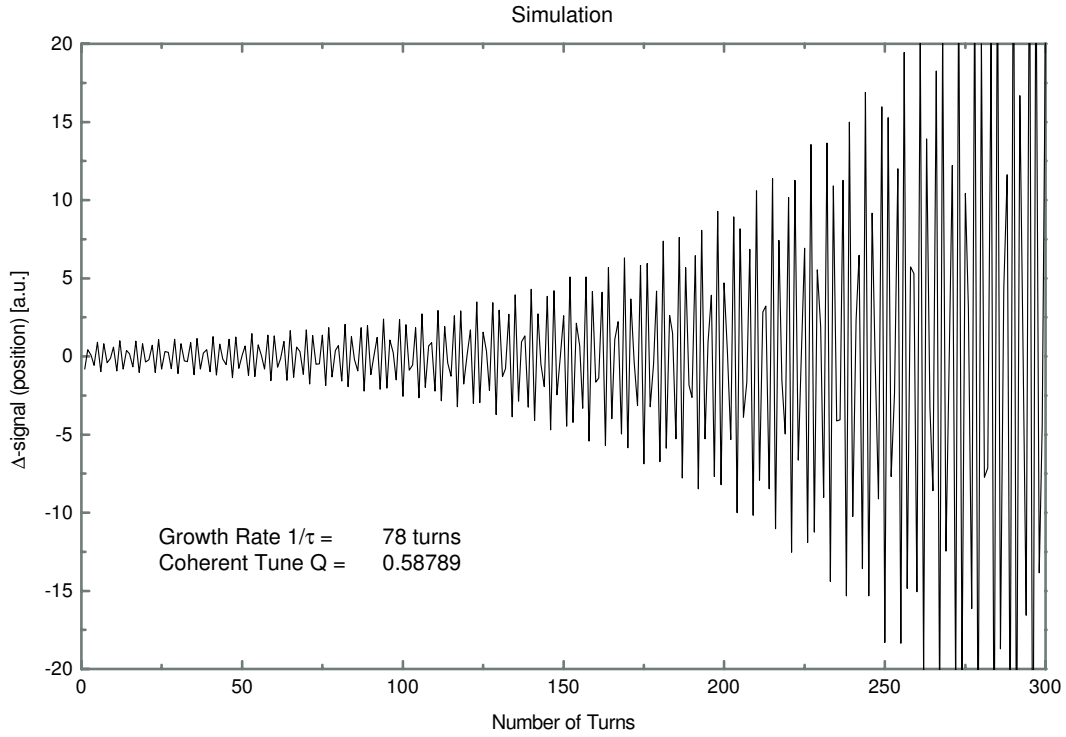

Figure 5.7: *Typical simulation result of resistive wall instability. Vertical BPM signal (offsets) of the last bunch in the batch (2100 bunches). Simulation of the SPS FT beam with resistive wall impedance according to Tab. 5.2.*

5.5 Simulated Resistive Wall Instability

For the simulation only the resistive wall effect (with 'inductive bypass') was considered, no other impedance elements have been used. First we will discuss simulation results for 1 batch (2100 bunches) in the machine and then the case of two batches (4200 bunches). The simulation model was presented in Sec. 5.4.

5.5.1 5/11–filling

One batch of 2100 bunches (every bucket filled) make up for exactly 5/11 (=2100/4620) of the machine's complete filling. Most of the measurement data was obtained with this kind of beam conditions.

The simulated data allows for more detailed analysis compared to the measurement of Sec. 5.3. We will first investigate the amplitude growth rates of individual bunches, then analyze their coherent tune behavior and finally take a look at coupled-bunch modes.

Amplitude Growth

First, and most important for the comparison to the measured data, we can analyze the amplitude growth rates along the batch. Fig. 5.8 shows the amplitudes of the

Vertical Plane

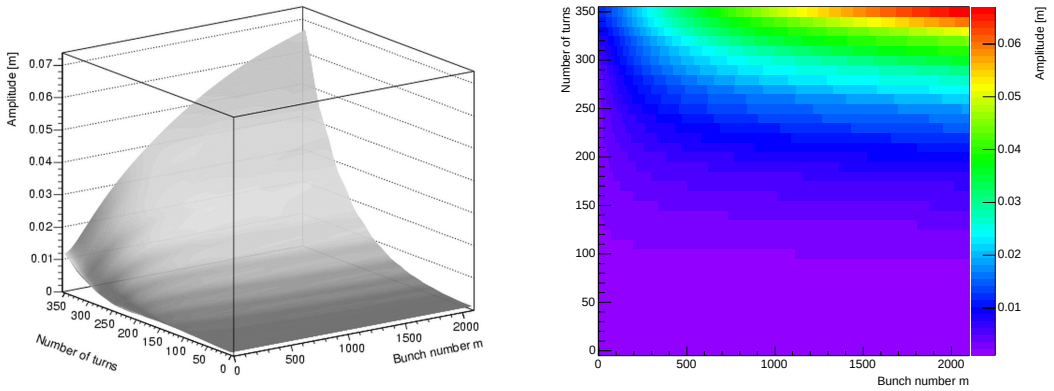

Figure 5.8: *Vertical amplitudes of bunches along the batch as function of number of turns. SPS FT beam, n_b = 2100 bunches, resistive wall impedance according to Tab. 5.2.*

Horizontal Plane

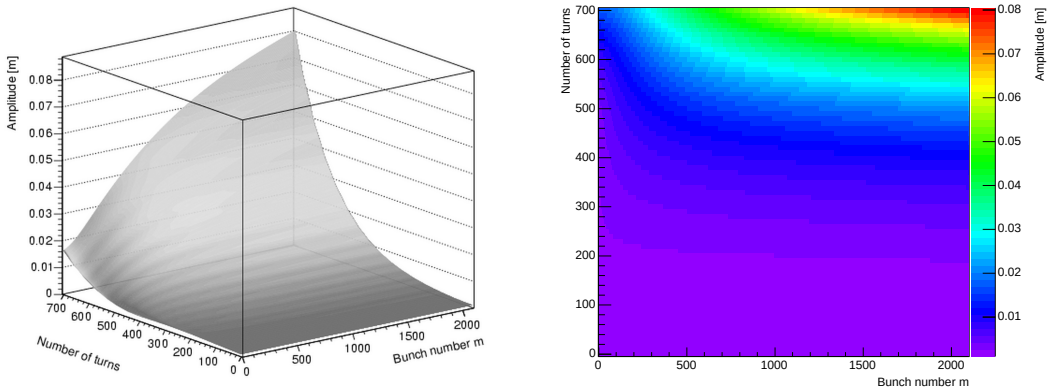

Figure 5.9: *Horizontal amplitudes of bunches along the batch as function of number of turns. SPS FT beam, $n_b = 2100$ bunches, resistive wall impedance according to Tab. 5.2.*

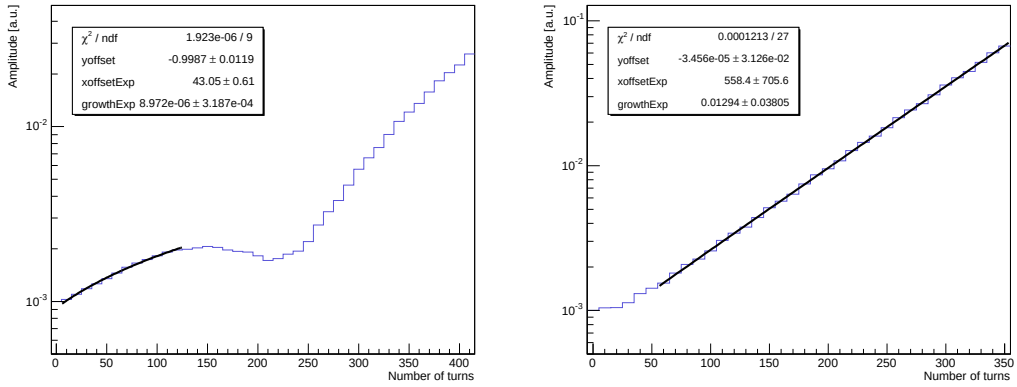

Figure 5.10: *Vertical amplitude growth rate of the first (left) and last (right) bunch in the batch. SPS FT beam, $n_b = 2100$ bunches, resistive wall impedance according to Tab. 5.2.*

bunches in the batch as function of turns in the vertical plane. One clearly sees that the head of the batch is affected much less than the end of the batch. This is due to the large gap (6/11 of the machine), where the wake fields have time to decay. But this should not lead to the conclusion that this is a 1-turn effect!

In fact, the bunches at the beginning of the batch become unstable too, as can be seen from Fig. 5.10. While the last bunch in the batch has a rather constant growth right from injection, the first bunch grows in amplitude over the first 130 turns, is then damped slightly and has then a growth rate comparable to the one of the last bunch, see also Fig. 5.10.

The conditions for the horizontal plane are depicted in Fig. 5.9 and Fig. 5.11. It is apart from the quantitative numbers exactly the same behavior as in the vertical plane.

The total variation in amplitude growth rate along the batch in the vertical plane is given in Fig. 5.12. One can see that the variation of the growth rates in the second half of the batch is below 8.5%. Similar results are obtained in the horizontal plane, see Fig. 5.13. The total variation is slightly higher, it is 10.9%. This corresponds to the maximum error due to the uncertainty in the measurement of the exact timing of the BPM. This uncertainty error will be taken into account when we compare to the measurement data.

Significance Level Significant results of the simulation are defined in the context of this study if the error is at the 20% level or below. Hence to be confident with the simulation results we want to estimate the final errors such that they are the *largest possible*. Doing so and obtaining errors that still stay below the 20% level, gives most significant results and we can decide to trust the simulation model.

For the simulation analysis we use the amplitude growth rate of the last bunch. This gives largest errors compared to the measurement, because we know that we did not measure the last bunch in the batch.

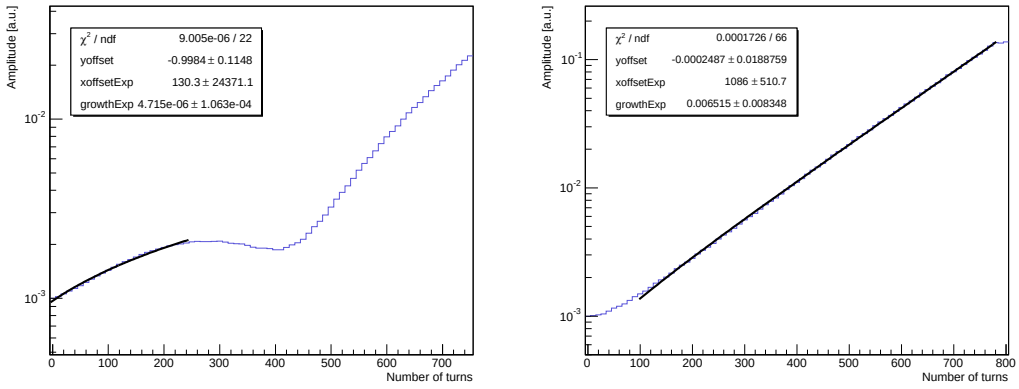

Figure 5.11: *Horizontal amplitude growth rate of the first (left) and last (right) bunch in the batch. SPS FT beam, $n_b = 2100$ bunches, resistive wall impedance according to Tab. 5.2.*

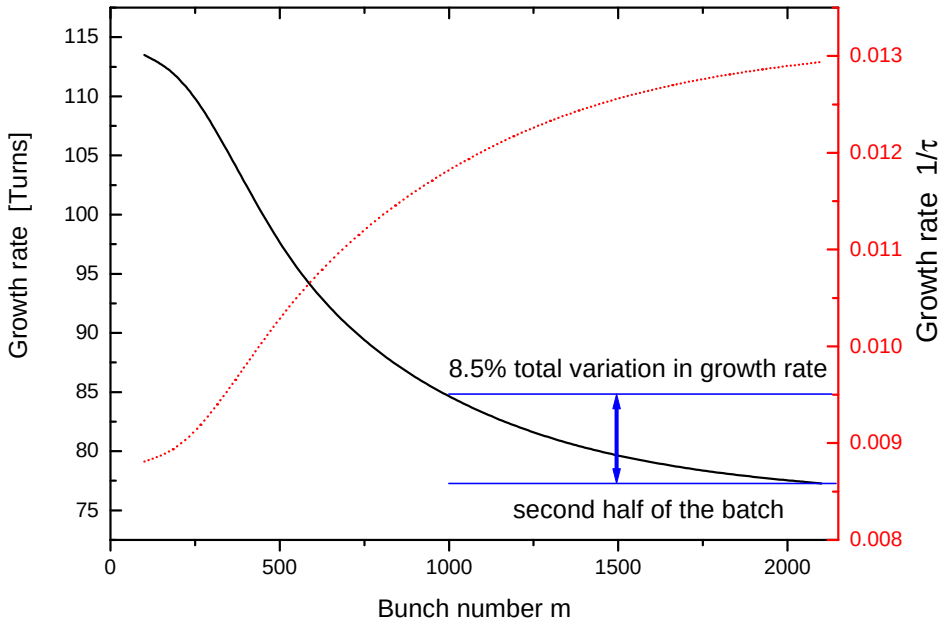

Figure 5.12: *Vertical amplitude growth rate variation along the batch. The total variation in the second half of the batch ($n_b = 2100$ bunches) is below 8.5 %. The growth rates for the first 100 bunches are not drawn as they can not be determined uniquely. Simulation of the SPS FT beam with resistive wall impedance according to Tab. 5.2.*

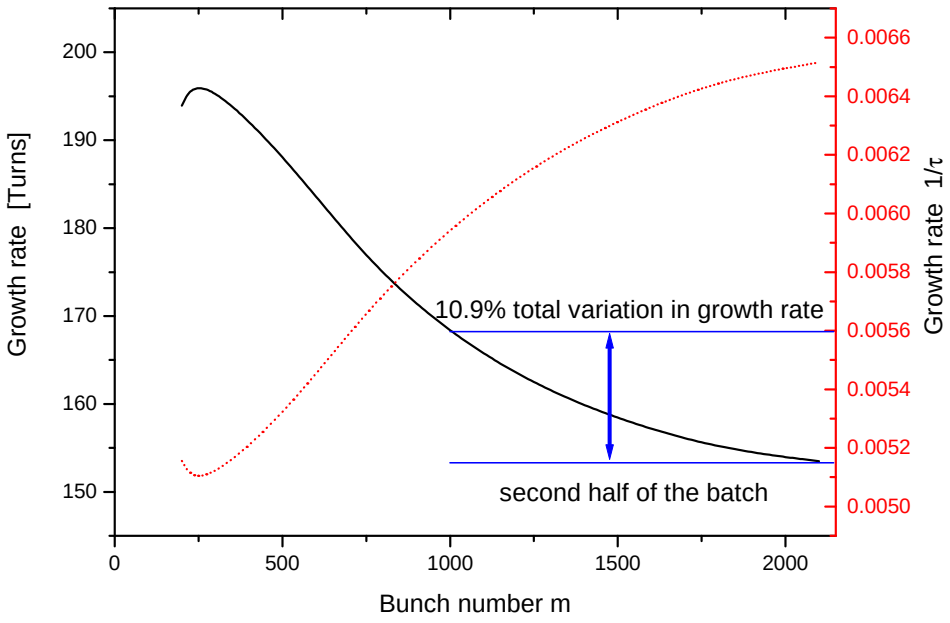

Figure 5.13: *Horizontal amplitude growth rate variation along the batch. The total variation in the second half of the batch ($n_b = 2100$ bunches) is below 10.9 %. The growth rates for the first 150 bunches are not drawn as they can not be determined uniquely. Simulation of the SPS FT beam with resistive wall impedance according to Tab. 5.2.*

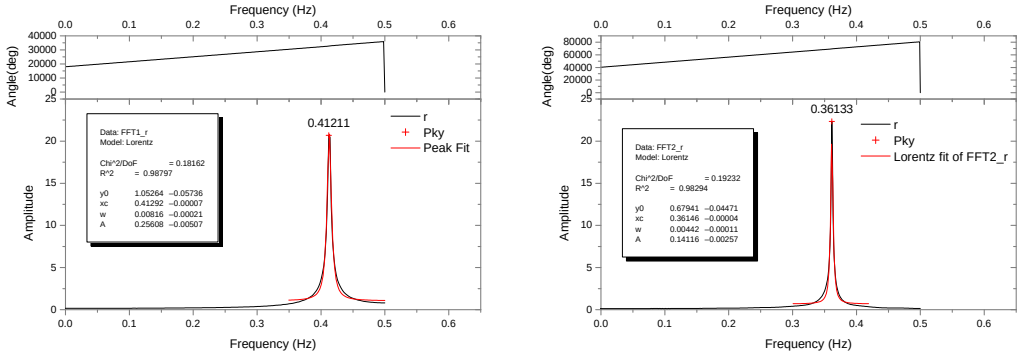

Figure 5.14: *Simulated vertical (left) and horizontal (right) coherent tune. SPS FT beam, $n_b = 2100$ bunches, resistive wall impedance according to Tab. 5.2.*

Growth rates found by simulation are $\tau_{H,\text{turns}} = 150\,\text{turns}$ in the vertical plane and $\tau_{H,\text{turns}} = 78\,\text{turns}$ in the horizontal plane.

Coherent tune

The coherent tunes obtained by the simulation are $Q_H = 0.63854$ and $Q_V = 0.58708$, see also Fig. 5.14. The tune shifts are $\Delta Q_H = 0.00146$ and $\Delta Q_V = 0.00292$. As expected for the resistive wall impedance, tune shifts and growth rates are of the same order of magnitude.

Coupled-Bunch Modes

In the simulation we also have the possibility to analyze the evolution of coupled-bunch modes and determine their growth rates. This is important, as analytic methods compute the mode growth rates and not the amplitude growth rates.

If there is strictly only one coupled-bunch mode present in the beam, one can deduce directly that the coupled-bunch mode growth rate $1/\tau_{\text{Mode}}$ has to be the same as the amplitude growth rate $1/\tau_{\text{Amp}}$. In practice there will always be several modes present in the beam and hence the amplitude growth rate will only approximately equal the strongest mode growth rate,

$$\max\left[1/\tau_{\text{Mode}}\right] \approx 1/\tau_{\text{Amp}}.$$

Coupled-bunch modes and partial filling At this stage it is appropriate to make a remark about the way the data is analyzed to obtain the coupled-bunch modes. Refer also to Sec. **??** for details on the coupled-bunch mode analysis used in MultiTRISIM.

In general the theory of instabilities as described by Sacherer [35] only treats equidistant (complete) fillings of the machine. M equidistant bunches can oscillate in M different eigen-modes $n = 0, \ldots, M-1$, and for mode n there is a constant

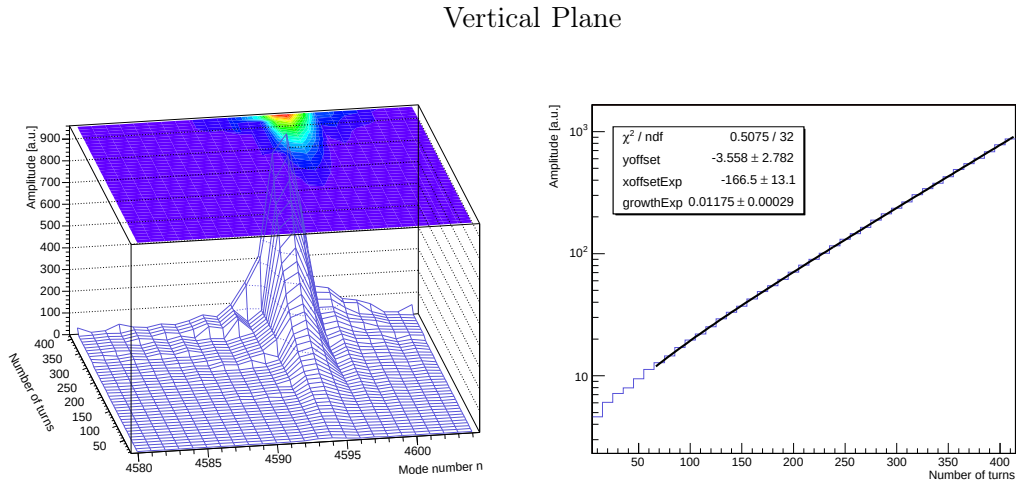

Figure 5.15: *Coupled-bunch modes of the FT beam (5/11 filling) in the vertical plane. The most dominant mode is n = 4595 in the EFEM system.*

phase relation between adjacent bunches of $\Delta\Phi = 2\pi n/M$. We call this eigen-mode system "EFEM", the equidistant filling eigen-mode system [31].

In partially filled machines a corresponding eigen-mode system exists as well. It is difficult to obtain it analytically. Hence we will always analyze coupled-bunch modes in the EFEM system.

Since the EFEMs are not the orthogonal basis for a non-equidistant pattern of oscillating bunches we expect to see distributions of modes rather than sharp, isolated modes.

Fig. 5.15 shows the evolution of the most dominant coupled-bunch modes in the vertical plane. The growth rate of the strongest mode with number 4595 is $2\pi/\tau = 0.01175 \pm 0.00029$, which refers to 85.1 ± 2.1 turns. The growth is smaller as compared to the amplitude growth rate of the last bunch in the batch, which was discussed before. Also note the distribution of modes around the strongest mode 4595. This is due to the partial filling of the machine.

The horizontal plane is shown in Fig. 5.16. There, the growth rate of the strongest mode with number 4595 is $2\pi/\tau = 0.00589 \pm 0.00019$, which refers to 169.7 ± 5.5 turns. The growth is again smaller as compared to the amplitude growth rate of the last bunch in the batch, because there is a distribution of modes around the strongest mode 4595.

Actually mode 4595 is the strongest mode in the end of the simulation, where the beam becomes unstable. At injection different modes are present and there is a transition from the injected modes to the most unstable one. This is shown in Fig. 5.17 and Fig. 5.18.

Horizontal Plane

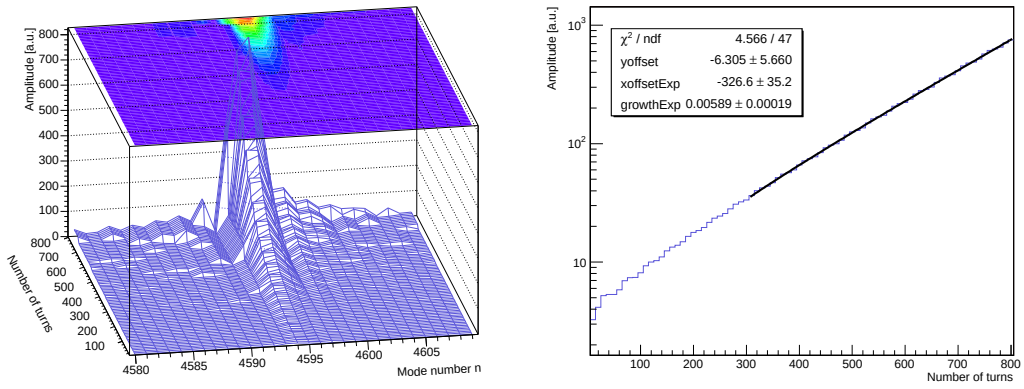

Figure 5.16: *Coupled-bunch modes of the FT beam (5/11 filling) in the horizontal plane. The most dominant mode is n = 4595 in the EFEM system.*

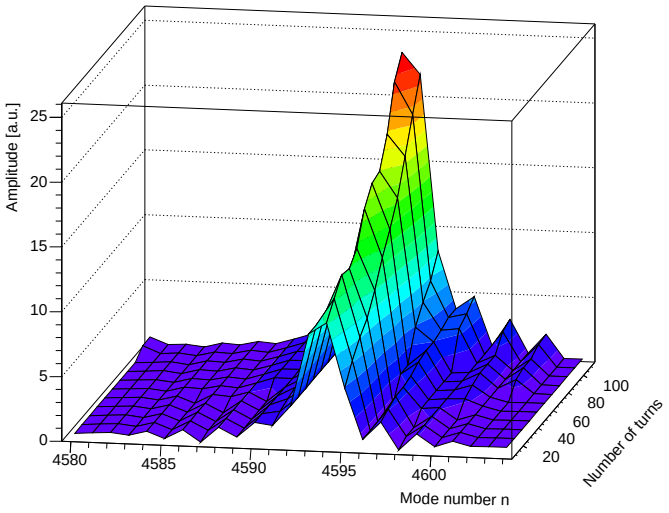

Figure 5.17: *Coupled-bunch modes of the FT beam (5/11 filling) in the vertical plane over the first 100 turns. The dominant mode changes from modes 4592-4593 to mode 4595, see also Fig. 5.15.*

Table 5.7: *Simulation results, SPS Fixed Target beam*

1 Batch (2100 bunches)	Growth rate $2\pi/\tau$ [turns]	Coherent tune Q
Vertical Plane	78 ± 2	0.58708 ± 0.0001
Horizontal Plane	150 ± 5	0.63854 ± 0.0001

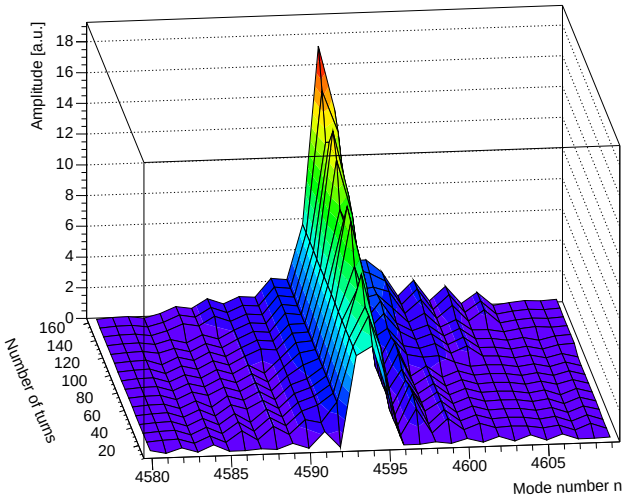

Figure 5.18: *Coupled-bunch modes of the FT beam (5/11 filling) in the horizontal plane over the first 100 turns. The dominant mode changes from modes 4592-4593 to mode 4595, see also Fig. 5.16.*

5.5.2 10/11–filling

Only few measurements have been made with 2 batches in the SPS and thus did not allow for a complete analysis of the data. However it is interesting to take a look at the differences compared to one batch in the simulation.

Two batches of 2100 bunches each (consecutive buckets filled) make up for 10/11 (=4200/4620) of the machine's complete filling. This comes already very close to the complete filling. In the measurements only sample data could be taken with this filling, as the beam was less stable and only little time left in the MD session.

In analogy to the previous section we will first investigate the amplitude growth rates of individual bunches, then analyze their coherent tune behavior and finally take a look at coupled-bunch modes. We will restrict the analysis to the vertical plane only.

Amplitude Growth

Fig. 5.19 shows the amplitude growth along the batch as function of turns in the vertical plane. It is clearly visible that there is less amplitude variation along the second batch, also the average amplitude in the second batch is slightly less than in the first batch. Overall, the second batch appears more homogenous in its amplitude growth in the simulation.

The difference compared to the first batch can be explained by the following argument: There are no wake fields prior to injection, the wakes build up in the first turn after injection. Therefore bunch 1 (first bunch of first batch) does not see any wake fields at all on the first turn in the machine, while bunch 2101 (first bunch

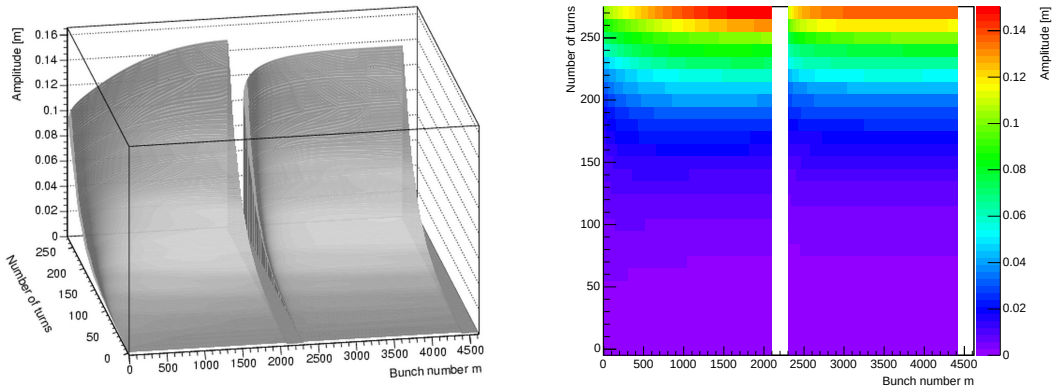

Figure 5.19: *Vertical amplitudes of bunches along the two batches as function of number of turns. SPS FT beam, $n_b = 4200$ bunches, resistive wall impedance according to Tab. 5.2.*

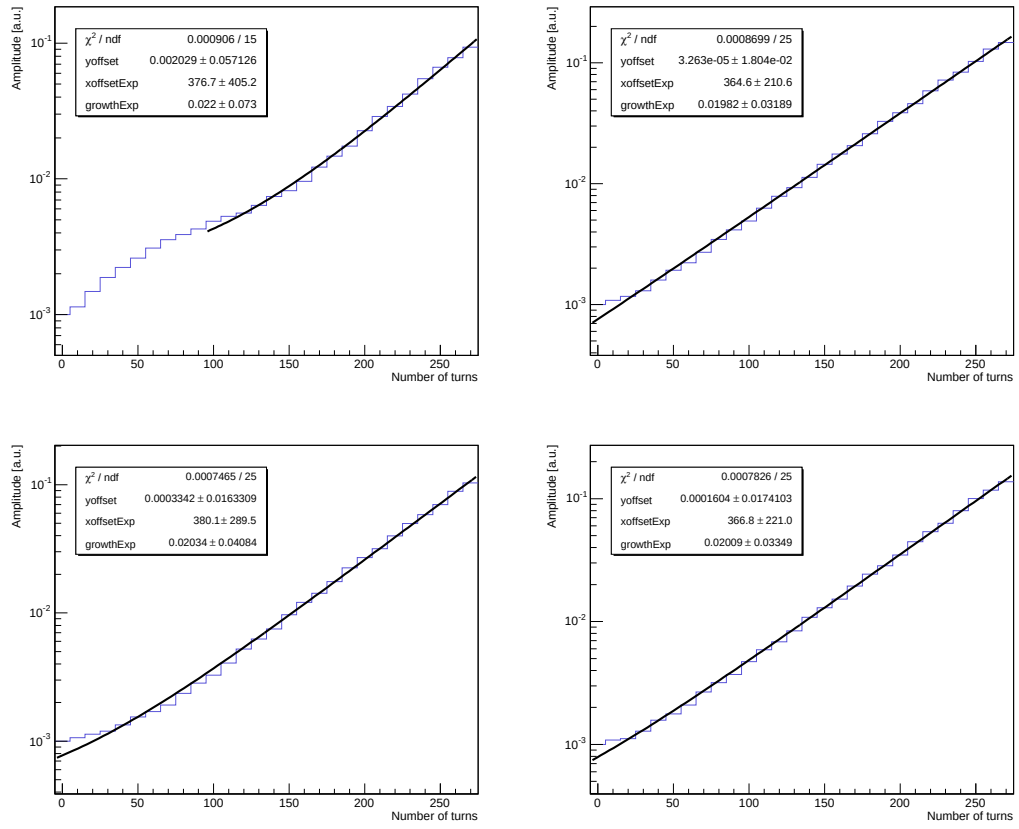

Figure 5.20: *Vertical amplitude growth rate of the first (top left) and last (top right) bunch in the first batch and of the first (bottom left) and last (bottom right) bunch in the second batch. SPS FT beam, $n_b = 4200$ bunches, resistive wall impedance according to Tab. 5.2.*

of second batch) already sees the wakes left behind by the preceding batch. This difference in behavior is visible in the simulation.

In an actual measurement (MD) this cannot occur in this way, since feedback is required to keep the first batch stable. When feedback is switched off (after injection oscillations die down), the first batch see the same wake as the second one.

The evolution of individual amplitudes for the first and last bunch in each batch is depicted in Fig. 5.20. Apart from the first bunch in the first batch, all bunches have similar growth rates and also growth behavior. The reason was already explained above.

Coherent tune

The coherent tunes obtained by the simulation are $\mathrm{Re}\, Q_H = 0.63799$ and $\mathrm{Re}\, Q_V = 0.58607$. The tune shifts are $\mathrm{Re}\, \Delta Q_H = 0.00201$ and $\mathrm{Re}\, \Delta Q_V = 0.00393$.

Coupled-Bunch Modes

It is interesting to look at the differences in the coupled-bunch mode behavior for the 5/11 filling and the nearly complete 10/11 filling.

To tie in with the considerations on the EFEM analysis we assume in case of an almost complete filling to see not distributions of modes in the mode spectrum, but more clear, sharp pronounced peaks, because now the EFEM system better fits to the actual eigen-mode system.

Fig. 5.21 shows the coupled-bunch mode spectrum for the 10/11 filling scheme. Compared to the spectrum of the 5/11 filling, see Fig. 5.15, the spectrum shows now much sharper peaks, as was expected. The strongest mode is now $n = 4594$, compared to $n = 4595$ with 5/11 filling. But it is a clear single peak, the neighboring modes 4593 and 4595 are stable and do not grow at all.

For an incomplete filling the assignment of modes is of course not unique, but results can nevertheless be well compared to analytical calculations. It is obvious from the presented results, that for the 5/11 filling the spread in modes is not very large and hence using the EFEM system to analyze the data is justified.

The most dominant coupled-bunch mode $n = 4594$ has a growth rate of $2\pi/\tau = 0.01823 \pm 0.00995$, which refers to 55 ± 29 turns. There is a large error on the fit because of very few number of turns available for the fit.

Fig. 5.22 shows the first turns after injection. For the 10/11 filling we see that the most unstable mode ($n = 4594$) is present directly at injection.

5.6 Comparison of Results

In addition to the error in the growth rate determination, there is an error due to the uncertainty in the exact timing of the measured data along the batch, see Figs. 5.13–5.12.

Tab. 5.8 summarizes the comparison between the data taken in the MD with the fixed target beam and the corresponding simulation data obtained with Multi-TRISIM. The uncertainty error is given as additional error on the measured data.

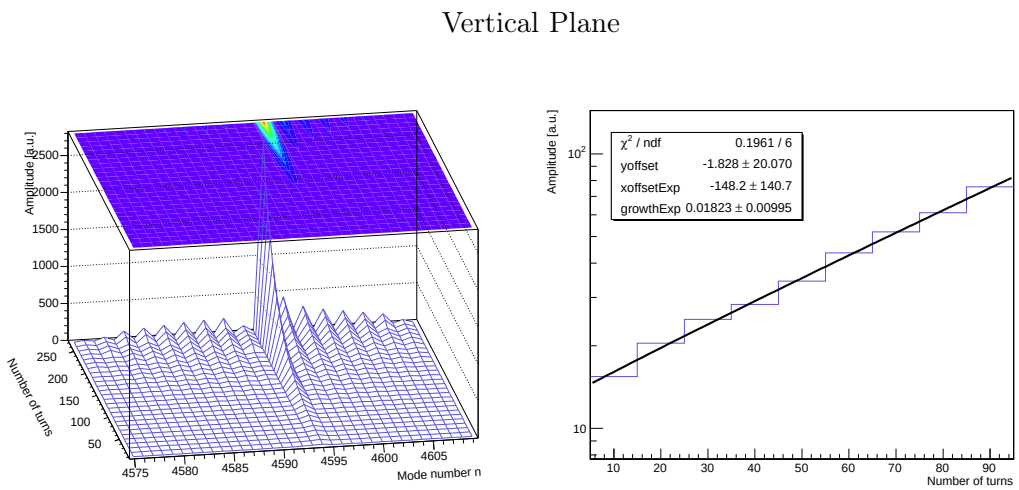

Figure 5.21: *Coupled-bunch modes in the vertical plane. The most dominant mode is n = 4594. Sharp mode peaks occur because the 10/11 filling is almost a complete filling, which corresponds to the EFEM system. Simulation of the SPS FT beam (2 batches, $n_b = 4200$) with resistive wall impedance according to Tab. 5.2.*

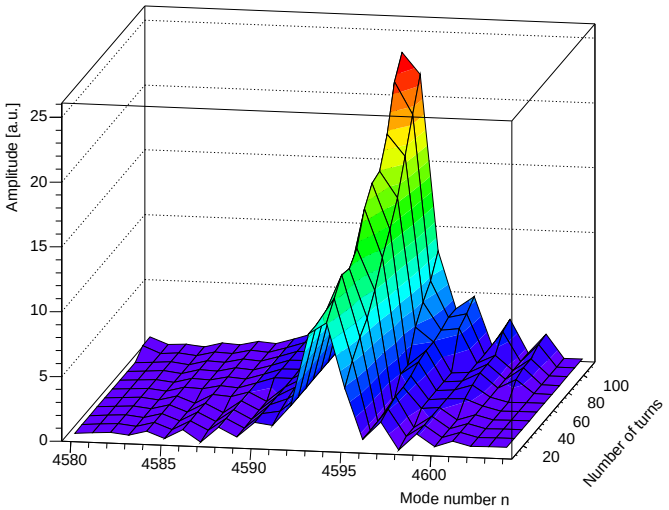

Figure 5.22: *Coupled bunch modes in the vertical plane at injection. The most unstable mode n = 4594 is hit already at injection, see also Fig. 5.21. Simulation of the SPS FT beam (2 batches, $n_b = 4200$)*

Table 5.8: *Measurement compared to Simulation, SPS Fixed Target beam*

	Coherent Tune $\mathrm{Re}\,\Delta Q$	Growth rate $2\pi\,\mathrm{Im}\,\Delta Q$	Growth rate $(2\pi\,\mathrm{Im}\,\Delta Q)^{-1}$ [turns]
Vertical Plane	0.5927 ± 0.0079	$0.012987\pm$	$77 \pm 4 \pm 8.5\%$
Horizontal Plane	0.6180 ± 0.0029	$0.005449\pm$	$183.5 \pm 23.5 \pm 10.9\%$
Vertical Plane	0.5871 ± 0.0001	0.01294 ± 0.0003	78 ± 2
Horizontal Plane	0.6385 ± 0.0001	0.00652 ± 0.0002	150 ± 5
Vertical Plane	0.5861 ± 0.0001	0.02009 ± 0.0100	50 ± 25

Table 5.9: *Simulation results – mode growth rates*

	Mode	Mode growth rate $2\pi/\tau_{\mathrm{Mode}}$ [1/turns]	Mode growth rate $(2\pi/\tau_{\mathrm{Mode}})^{-1}$ [turns]
Vertical Plane	4595	0.01175 ± 0.00029	85.1 ± 2.1
Horizontal Plane	4595	0.00589 ± 0.00019	169.7 ± 5.5
Vertical Plane	4594	0.01823 ± 0.00995	55 ± 29

Tab. 5.9 additionally summarizes the simulation results concerning the coupled-bunch modes.

The simulated values for the growth rates are in excellent agreement with the measured quantities within a few percent, i.e. least below or near the defined significance level of 20%. Especially in the horizontal plane the agreement could be better, but due to dispersion the measurements in the horizontal plane are always worse than those in the vertical plane.

Also the coherent tunes are given in Tab. 5.8.

Since we were not able to determine the tune slope for the measured data, the actual tunes of the machine could not be determined by extrapolation to zero current and no common tune reference is available to compare with the simulation.

We conclude to get good agreement and the simulation model is validated.

5.7 SPS Collimator Test

In October 2004 a prototype of the LHC collimator will be installed and tested in the SPS. This is mainly to measure the collimation properties and the mechanical durability of the proposed design. Furthermore tune shift and growth rate measurements can be carried out to measure the collimator impedance.

A simulation of the measurement of the LHC collimator impedance in the SPS was envisaged. The beam conditions and collimator parameters foreseen for this test are given in Tab. 5.10.

Table 5.10: *Conditions for LHC collimator test in CERN SPS*

Parameter	Symbol	Unit	Value
Momentum	p	[GeV/c]	270
Tune	Q_H		26.185
Tune	Q_V		26.130
Maximum number of batches			4
Number of bunches per batch			72
Bunch Intensity	N_p		$1.1 \cdot 10^{11}$
Maximum total Intensity	$N_{p,tot.}$		$3.2 \cdot 10^{13}$
Batch spacing		[ns]	250
Bunch spacing		[ns]	25
Collimator conductivity	σ	$[(\Omega m)^{-1}]$	$7.14 \cdot 10^4$
Collimator opening	b	[mm]	0.5-60
Collimator length	l	[m]	1.0

Two resistive wall impedance models were tested, the classical thick-wall formula and the one with inductive bypass, refer to Chap. 4 for details. The simulation results for the two impedance models are given in Tab. 5.11.

Table 5.11: *Growth rates and coherent tunes obtained by simulation for the LHC collimator test in the SPS. Beam conditions of Tab. 5.10*

Classic Resistive Wall Impedance

Conditions	Growth Rate	Tune ($Q_0 = 0.13$)	Tuneshift
Collimator N/A	$1/\tau = 410$ Turns	$Q = 0.12988$	$\Delta Q = 0.00097$
Collimator @ 2 mm	$1/\tau = 116$ Turns	$Q = 0.12891$	

Resistive Wall Impedance with Inductive Bypass

Conditions	Growth Rate	Tune ($Q_0 = 0.13$)	Tuneshift
Collimator N/A	$1/\tau = 467$ Turns	$Q = 0.12988$	$\Delta Q = 0.00049$
Collimator @ 2 mm	$1/\tau = 438$ Turns	$Q = 0.12939$	

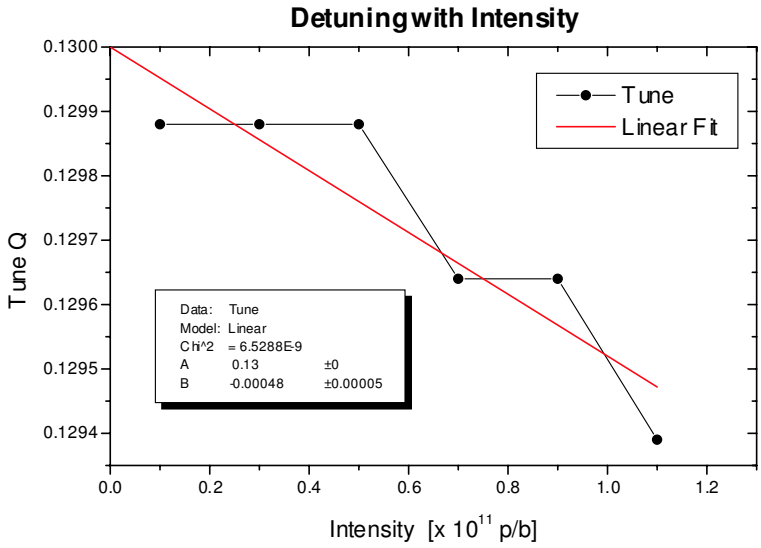

Figure 5.23: *Simulated detuning with intensity for the LHC Collimator test in the SPS.*

By varying the intensity from $0.1 - 1.1 \cdot 10^{11}$ p/b the tune slope was established for the above mentioned parameters. Fig. 5.23 shows the results. Mind the steps due to the bad resolution of the FFT.

Concerning the impedance models and their verification in measurements with the collimator in the SPS, the results can be summarized as follows:

- If the inductive bypass effect is NOT present, tuneshift and growth rate measurements should clearly indicate it.
- If the inductive bypass model is valid, growth rate measurements with varying collimator gap would be the appropriate tool of verification.
- Also the tuneshift variation with collimator gap variation should show a visible difference for the two impedance models.

5.8 A Note on Equidistant Filling and the Effect of Gaps and Injection Oscillations

Only equidistant filling patterns can be analyzed by analytical methods. In reality the bunch layout will always have a gap in the filling scheme, because it is needed by the injection or extraction kicker due to its finite kicker rise time.

A perfect injection into the machine would imply that all bunches get the same offset (coordinate x) and zero deflection (coordinate $x' = dx/ds$) at the injection position. In reality this can never be achieved due to kicker ripples and already present oscillation of the bunches in the transfer line [20].

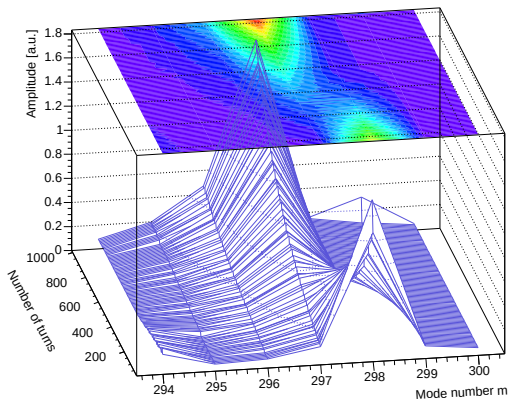

Figure 5.24: *Most stable mode damped, most unstable growing.*

In the following, a connection will be made between the most unstable coupled-bunch mode (for the special case of the resistive wall instability) and the coupled-bunch mode the beam possesses due to injection into machine.

Coupled-Bunch Modes A bunched beam with M equally-spaced bunches can have M coupled-bunch modes, named $n = 0, \ldots, M-1$. The according multi-bunch spectrum has lines at frequencies

$$\omega = (p\,M + n + Q) \cdot \omega_0, \qquad (5.3)$$

with $p \in [-\infty, \infty]$, Q the transverse tune and ω_0 the angular revolution frequency.

Resistive Wall Impedance and Instability For the classical resistive wall impedance decreasing with $1/\sqrt{\omega}$, the real part of the impedance has its largest negative values for frequencies ω just below zero. Hence the most unstable coupled-bunch mode will be the one with the first negative spectral line. The most unstable mode number n is given by

$$\max\left[\,p\,M + n + Q < 0\,\right], \quad n = 0, \ldots, M-1. \qquad (5.4)$$

In other words this will give the coupled bunch mode n

$$n \text{ most unstable: } n + Q < 0 \quad \Longrightarrow \quad n \approx -Q. \qquad (5.5)$$

(A numerical example: $Q = 26.59$, $M = 4620$, $n \approx -27 = 4620 - 27 = 4593$).

Identifying Coupled-Bunch Modes at a BPM Given a certain coupled-bunch mode number n, the beam position signal at a fixed location will be proportional to

$$\Delta_{\mathrm{BPM}} \propto \mathrm{Re}\left[\exp j(n+Q)\omega_0 t\right]. \qquad (5.6)$$

This follows from the definition of coupled-bunch modes. At the BPM we will see the tune Q shifted by the coupled-bunch mode number n.

Injection When bunches are injected fixed offset into the machine, it means that the beam position signal at the injection point will be a constant

$$\Delta_{\text{BPM, inj.}} = const.. \tag{5.7}$$

The BPM signal given by 5.6 can be only a constant if $n + Q = 0$, or

$$\Longrightarrow n \approx -Q. \tag{5.8}$$

Hence injection with a fixed offset excities always the most unstable mode for a resistive impedance.

Which coupled-bunch mode does this correspond to? Which coupled- bunch mode is present in the machine right after injection? The answer comes directly from the above formulae:

$$\begin{aligned} \Delta_{\text{BPM, inj.}} &\stackrel{!}{=} const. \propto \text{Re}\left[\exp j(n+Q)\omega_0 t\right] \\ &\Longrightarrow n \approx -Q. \end{aligned} \tag{5.9}$$

This is exactly the most unstable mode as pointed out above!

Conclusion Concerning the resistive wall impedance the following conclusion can be drawn: Due to the nature of the injection process, the most unstable coupled-bunch mode will always be present in the machine after injection. This result is obtained for an equidistant filling of the machine.

Gaps in the filling scheme as well as non-perfect injection can only improve the situation, i.e. such beams will be more stable. Refer to Figs. 5.25–5.27 for simulation results confirming this behavior.

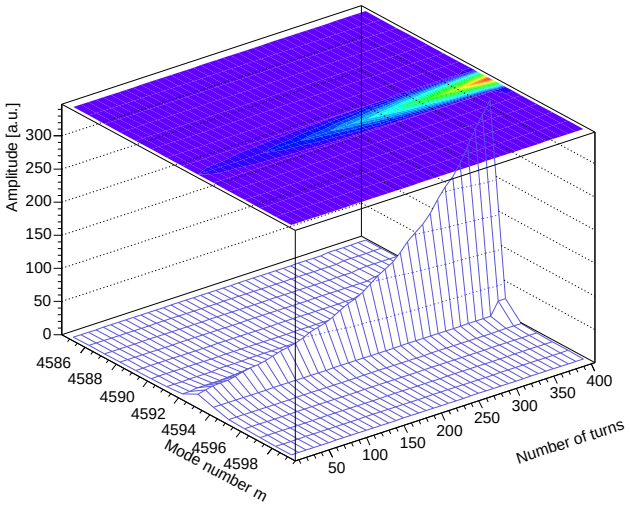

Figure 5.25: *Coupled-bunch mode spectrum over time in the vertical plane. Mode-range 4585-4600. Simulated was a complete filling in the SPS with parameters* $Q_y = 26.59$, $M = 4620$. *The injection mode* $n \approx -27 = 4620 - 27 = 4593$ *equals the most unstable mode.*

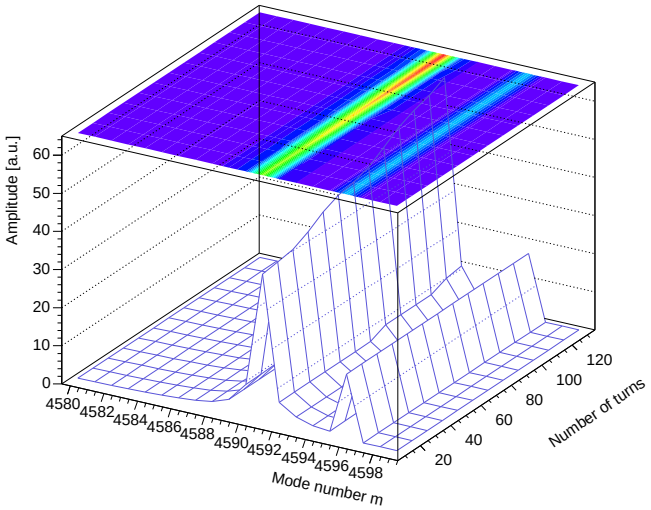

Figure 5.26: *Coupled-bunch mode spectrum evolution over time in the vertical plane. Mode-range 4580-4600. Simulated was a complete filling in the SPS with parameters* $Q_y = 26.59$, $M = 4620$. *The injection was such that modes 4591 and 4596 were present at injection. The most unstable mode* $n \approx -27 = 4620 - 27 = 4593$ *is not present for the first 100 turns but starts to grow later than in the case of Fig. 5.25.*

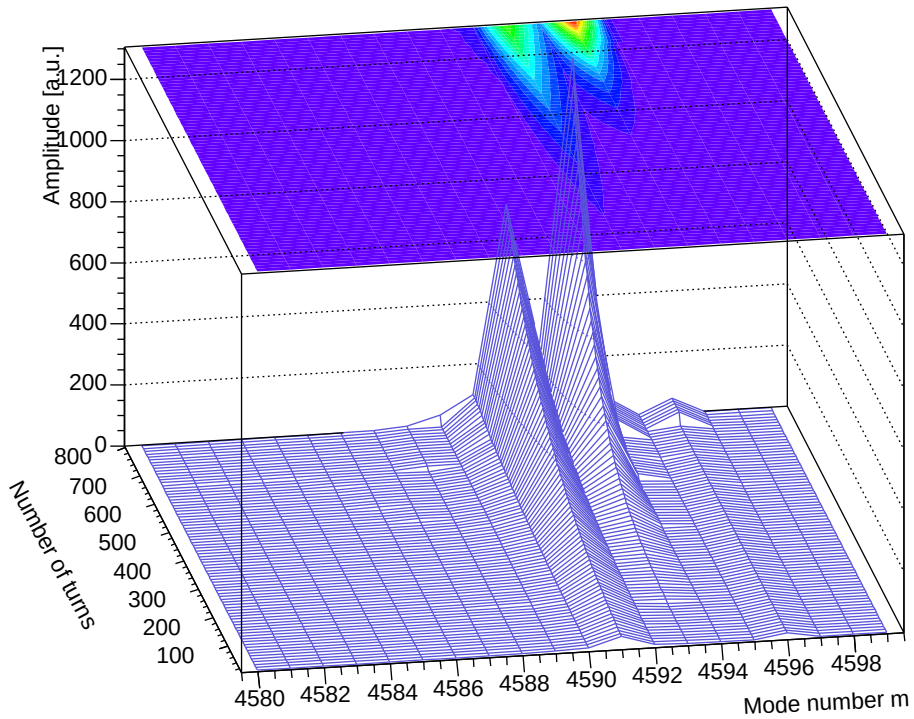

Figure 5.27: *Coupled-bunch mode spectrum over time in the vertical plane. Mode-range 4580-4600. Simulated was a complete filling in the SPS with parameters* $Q_y = 26.59$, $M = 4620$. *The injection was such that modes 4591 and 4596 were present at injection. The most unstable mode* $n \approx -27 = 4620 - 27 = 4593$ *starts to grow later than in the case of Fig. 5.25. Note that also mode 4591 is unstable.*

Chapter 6

Results for LHC

The Large Hadron Collider (LHC) is a two-ring accelerator, using superconducting magnet technology to provide center-of-mass collisions with energies of up to 14 TeV. It will be installed in the 27 km long LEP tunnel. After its scheduled start-up in 2007 it will aim at the discovery of the Higgs particle and the study of other rare events.

High bunch repetition rates and high bunch intensities could cause several (collective) instabilities in the machine. A very good summary of all collective effects concerning LHC can be found in [33]. Due to the challenging parameters of the LHC, multi-bunch and/or multi-turn instabilities become an issue. One of it is the long-range effect of Higher Order Modes (HOMs) of cavities and the other is the resistive wall instability. The latter aroused particular interest, as in 2001 it was decided to fabricate the LHC collimators of graphite. They have a very high resistivity and are expected to come very close to the beam.

The simulation code MultiTRISIM was developed to study such instabilities, where particular emphasis was put on the resistive wall impedance. Starting with the parameters of LHC, this chapter will consist in showing and discussing the simulation results obtained for LHC.

6.1 The LHC in parameters

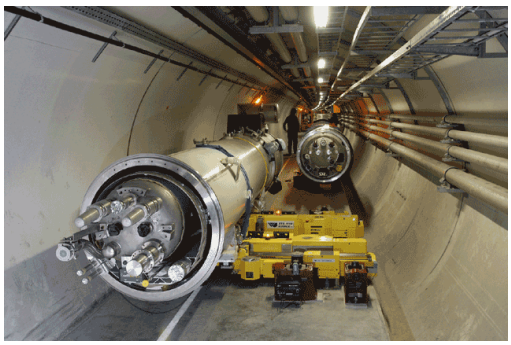

Figure 6.1: *View of the LHC tunnel (2004).*

The LHC will collide proton or heavy-ion beams of high intensities. The performance goals are mainly determined by the physics experiments requirements in their quest for the Higgs particle.

What matters for the physics experiments is the event rate N_{event}, which is related to the machine luminosity L through

$$N_{\text{event}} = L\,\sigma_{\text{event}} \tag{6.1}$$

where σ_{event} is the cross section for the physics event under study. The machine luminosity L assuming Gaussian bunches is given by

$$L = \frac{N_p^2 \, n_b \, f_0 \, \gamma_r}{4 \, \pi \, \varepsilon_n \, \beta^*} \tag{6.2}$$

where N_p is the number of particles per bunch, n_b the number of bunches per beam, f_0 the revolution frequency, γ_r the relativistic gamma factor, ε_n the normalized transverse beam emittance and β^* the beta function at the collision point (IP).

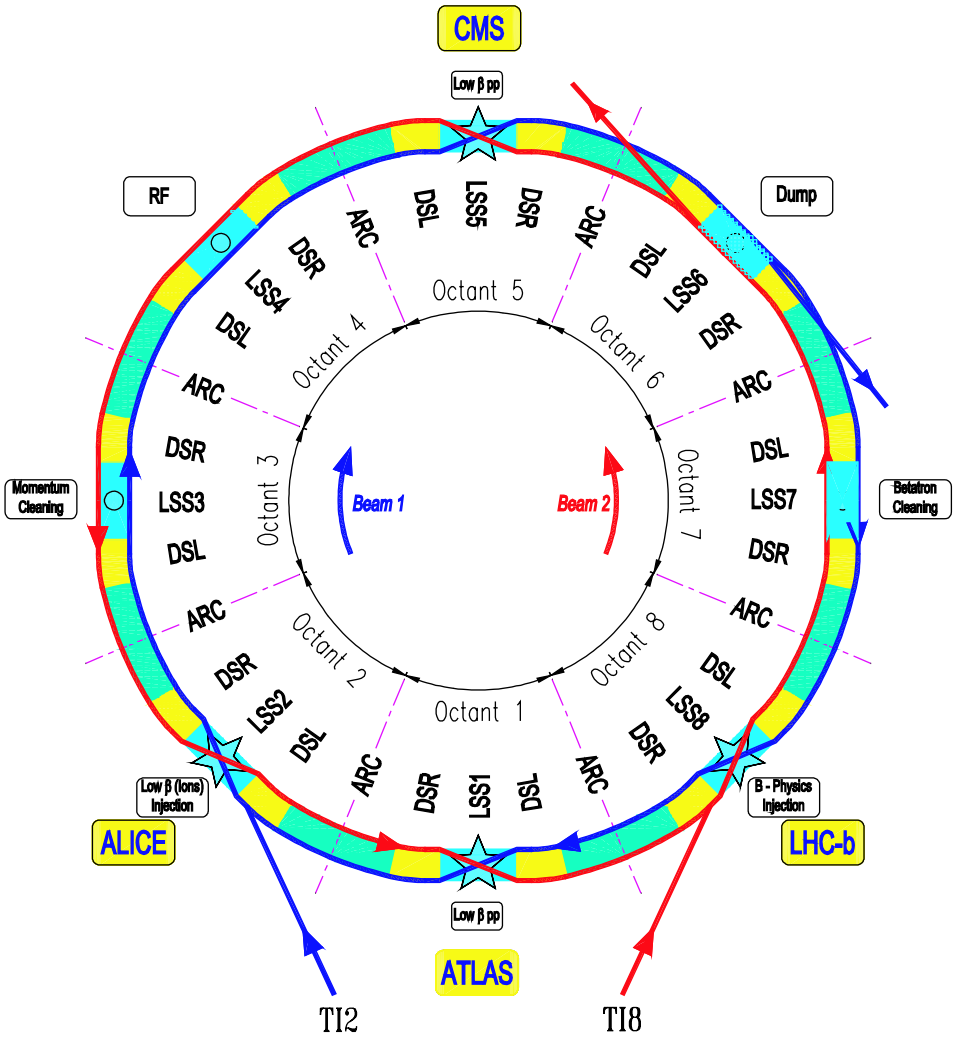

Figure 6.2: *Schematic layout of the LHC. The ring is divided into octants and there are four interaction points (IP), the experiments ATLAS, CMS, LHCb and ALICE. The two counterrotating beams have separate vacuum beam pipes and only meet at the four IPs.*

The two major LHC experiments, ATLAS and CMS, are high luminosity experiments designed for a peak luminosity of $L = 10^{34}\,\text{cm}^{-2}\text{s}^{-1}$.

The necessity of a large number of bunches with high bunch intensities follows immediately from Eq. 6.2. The γ_r is limited by present superconducting magnet technology and the revolution frequency f_0 is given by the dimension of the LEP tunnel. The values of β^* and ε_n can be tuned but cannot fall below certain threshold values. The requirements in terms of beam parameters (bunch intensity N_p and number of bunches n_b) follow immediately. LHC will be operated with $n_b = 2808$ bunches, each with an intensity of $N_p = 1.15 \cdot 10^{11}$. The ultimate intensity goal is $N_p = 1.7 \cdot 10^{11}$ particles per bunch.

Fig. 6.2 shows the schematic layout of the LHC. The general beam optics parameters of the LHC are summarized in Tab. 6.1 for injection and top energy (collision).

Table 6.1: *LHC general parameters*

Parameter	Symbol	Unit	**Injection**	**Collision**
Momentum	p	[GeV/c]	450	7000
Machine circumference ($= 2\pi R$)	C	[m]	26658.883	
Machine radius	R	[m]	4242.890	
Revolution frequency	f_0	[Hz]	11245.5	
Revolution time	T_0	[μs]	88.93	
Lattice type			FODO, 2-in-1	
Number of lattice cells per arc			23	
Phase advance per cell	Φ	[°]	90	
Dipole field	B	[T]	0.535	8.33
Bending radius	ρ	[m]	2803.95	
Main Dipole length	l	[m]	14.3	
Horizontal Tune			64.28	64.31
Vertical Tune			59.31	59.32
Maximum β-function H/V (cell)	$\beta_{\text{max.}}$	[m]	177/180	
Minimum β-function H/V (cell)	$\beta_{\text{min.}}$	[m]	30/30	
Average β-function ($= R/Q$)	$\langle\beta\rangle$	[m]	66/72	
Maximum dispersion H/V (cell)	$D_{\text{max.}}$	[m]	2.018/0.0	
Gamma transition	γ_T		55.678	
Momentum compaction	α_c		0.3225×10^{-3}	
Harmonic number	h		35640	
RF Frequency	f_{RF}	[MHz]	400.8	
RF Voltage	V_{RF}	[MV]	8.0	16.0
Synchrotron frequency	f_s	[Hz]	23.0	63.7

Concerning the resistive wall effect, the vacuum chamber dimensions and material properties are needed. The major part of the machine which the beam sees is the copper-coated stainless steel "beam screen". The beam screen is needed to protect the super-conducting magnets (at 1.9° K) against the heat deposited in the wall by synchrotron radiation. Hence the beam screen is an additionally cooled inlay in the stainless steel cold bore of the dipole magnets. The exact dimensions are given in

Table 6.2: *LHC vacuum chamber parameters.* b_x *and* b_y *are the inner vacuum chamber radii, given in millimeters. The relative length is given as fraction of the circumference* $C = 26658.9$ *m.*

Section	b_x [mm]	b_y [mm]	Length [m]	Length [%]
Cold part (beam screen)	22.0	19.0	24478.9	91.823
Warm part	22.0	22.0	2160.0	8.102
Collimator	0.5-60.0	0.5-60.0	20.0	0.075

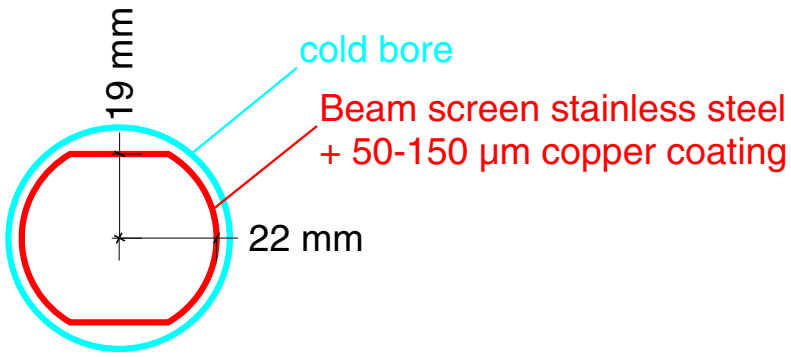

Figure 6.3: *Cross section of the LHC beam pipe. The copper coated beam screen is needed to protect the superconducting magnets (at cryogenic temperature of 1.9° K) from power deposition (heating) due to synchrotron radiation. The beam screen is a 1 mm thick Cu-coated stainless steel inlay.*

Fig. 6.3. The beam screen will be at temperatures of 4.2° K up to 20° K and thus its resistance is given for this value. Furthermore the effect of magneto-resistance has to be taken into account [14].

Tab. 6.2 lists the vacuum chamber dimensions and relative lengths in LHC. Note that the LHC has almost round vacuum chambers, hence we do not expect any asymmetry effects. The corresponding material properties are given in Tab. 6.3. LHC was designed already with special care on the resistive wall instability, hence the resistivities are kept extremely low. In the initial design the collimators were not considered, but in 2001 the collimator layout and its material graphite were chosen. Its implications on beam stability due to the rather large resistivity of graphite gave rise to renewed interest.

The beam parameters for LHC are summarized in Tab. 6.4. There is the nominal and the ultimate intensity beam. For the start-up of the machine, an intensity of 40% of the nominal one is panned.

Fig. 6.4 shows the nominal bunch pattern layout. There will be batches of 72 bunches, which will be grouped into 2, 3 or 4-batch units. Those form a bunch train of 39 batches in total which gives the total bunch number of 2808 ($= 39 \cdot 72$).

Table 6.3: *LHC vacuum chamber material parameters. The assumed temperatures T are given in Kelvin, ρ and σ_c denote the resistivity and conductivity. At top energy the magnetic field of $B = 8.65$ Tesla increases the resistivity due to the magneto-resistance effect.*

Section	Material	T [° K]	ρ [Ωm]	σ_c [$(\Omega\mathrm{m})^{-1}$]
Beam screen	Stainless steel$_{75\ \mu\mathrm{m\ Cu\ coating}}$	4.2	$2.8 \cdot 10^{-10}$	$3.6 \cdot 10^{9}$
	+ magneto-resistance$_{B=8.54\ T}$	4.2	$5.5 \cdot 10^{-10}$	$1.8 \cdot 10^{9}$
Warm part	Copper 2 mm thickness	293.15	$1.7 \cdot 10^{-8}$	$5.9 \cdot 10^{7}$
Collimators	Carbon (graphite)	293.15	$1.4 \cdot 10^{-5}$	$7.1 \cdot 10^{4}$

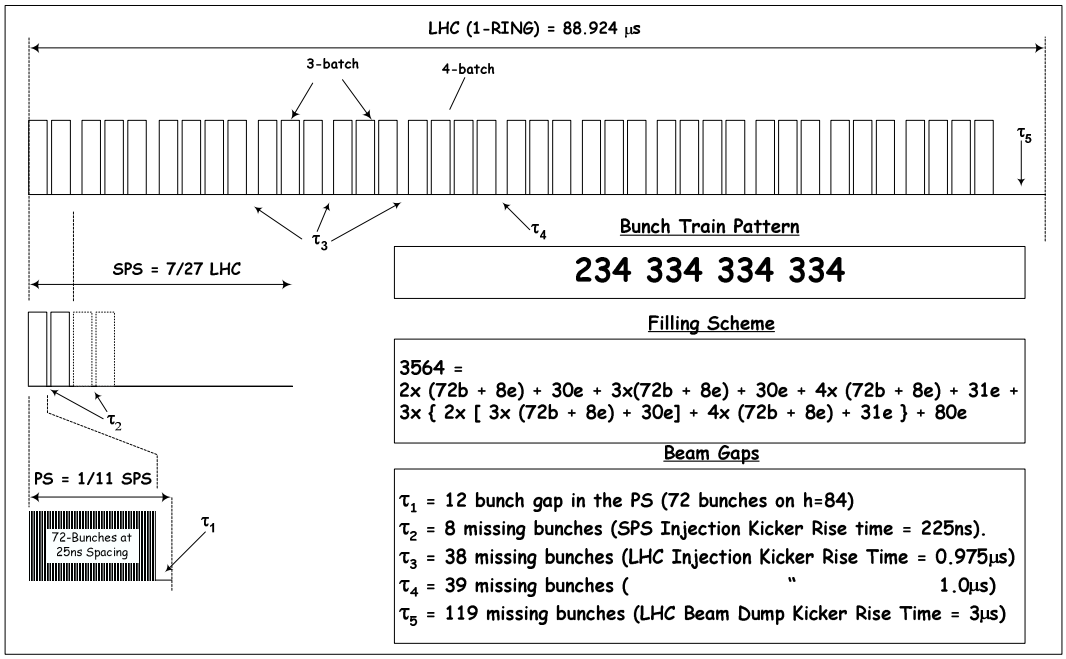

Figure 6.4: *Nominal proton bunch pattern in the LHC for 25 ns spacing.*

Table 6.4: *LHC performance parameters*

Parameter	Symbol	Unit	**Nominal**	**Ultimate**
Number of particles per bunch	N_p	$[10^{11}]$	1.15	1.67
Number of bunches	n_b		2808	
Bunch harmonic number	h		3564	
Filling time per ring	τ_{Fill}	[min]	4.3	
Bunch spacing	τ_{sp}	[ns]	25.0	
Total number of particles	N_{tot}	$[10^{14}]$	3.23	4.7
Total DC beam current	I	[A]	0.582	0.85
Stored energy per beam	E	[MJ]	366	531
Long. emittance at 450 GeV	ϵ_s	[eVs]	1.0	
Long. emittance at 7 TeV	ϵ_s	[eVs]	2.5	
Normalized trans. emittance (r.m.s.)	ϵ_n	$[\mu\text{m}]$	3.75	
Max. trans. beam size in arc at inj. (r.m.s.)	$\sigma_{x,y}$	[mm]	1.19	
Max. trans. beam size in arc at 7 TeV	$\sigma_{x,y}$	[mm]	0.3	
Trans. beam size at IP (r.m.s.) at 7 TeV	$\sigma_{x,y}$	$[\mu\text{m}]$	16.63	15.9
Trans. beam divergence at IP (r.m.s.)	$\sigma_{x',y'}$	$[\mu\text{rad}]$	30.23	31.7
β-function at IP	β	[m]	0.55	0.5
Maximum β-function in triplet	β_{max}	[m]	4705	
Luminosity	L	$[\text{cm}^{-2}\text{s}^{-1}]$	$1.0 \cdot 10^{34}$	$2.3 \cdot 10^{34}$
Events per crossing			19	44
Total crossing angle		$[\mu\text{rad}]$	285	400
Vacuum beam lifetime		[h]	84	100
Total luminosity lifetime		[h]	13.9	8.6
Energy loss per turn	U_0	[keV]	7	
Total radiated power per beam	P	[kW]	3.8	5.5
Long. emittance damping time (at 7 TeV)		[hours]	13	
Trans. emittance damping time (at 7 TeV)		[hours]	26	
Voltage of 200 MHz RF system at 450 GeV	V_{RF}	[MV]	3	
RMS bunch length at injection	σ_s	[cm]	11.24	
Relative rms energy spread at inj.		$[10^{-4}]$	4.716	
RMS bunch length at 7 TeV	σ_s	[cm]	7.55	
Relative rms energy spread at 7 TeV		$[10^{-4}]$	1.129	

Table 6.5: *LHC simulation model*

Interaction Point	Location [°]	β_x [m]	β_y [m]	μ_x [rad]	μ_x [rad]
Injection and BPM	0.0	103.4	103.4	0	0
Accelerating Cavity	180.0	69.9	71.5	32.155	29.660
Resistive Wall Impedance	185.0	69.9	71.5	33.048	30.484
Higher Order Modes (HOM)	335.0	69.9	71.5	59.844	55.201
Arc octupole	22.5	180.0	40.0	4.019	3.708
Arc octupole	67.5	40.0	180.0	12.058	11.123
Arc octupole	112.5	180.0	40.0	20.097	18.538
Arc octupole	157.5	40.0	180.0	28.136	25.953
Arc octupole	202.5	180.0	40.0	36.174	33.368
Arc octupole	247.5	40.0	180.0	44.213	40.783
Arc octupole	292.5	180.0	40.0	52.252	48.198
Arc octupole	337.5	40.0	180.0	60.291	55.613

6.2 LHC Simulation Model

To simulate the LHC, the general parameters given in Tab. 6.1 are used. The beam parameters for the nominal and the ultimate LHC proton beam are summarized in Tab. 6.4. The LHC simulation uses the bunch pattern of Fig. 6.4.

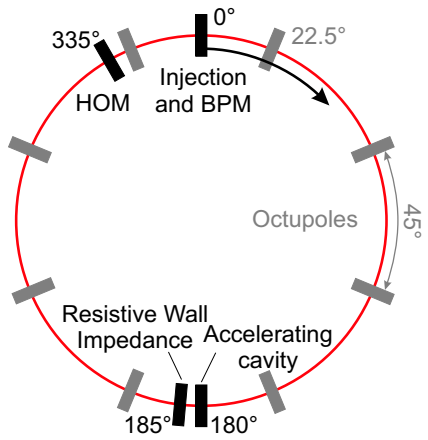

Figure 6.5: *LHC simulation model.*

A simple ring consisting of 4 to 12 elements is used, see Fig. 6.5. The first element is the machine start, were injection occurs and also where we measure the bunch positions on consecutive turns. If octupoles are included in the simulation, there is one octupole element at each arc (octant). Furthermore we include an accelerating cavity, the resistive wall IP (interaction point) and another IP where kicks due to the Higher Order Modes (HOM) are applied. The location, beta values and phase advance for each element is given in Tab. 6.5. For the resistive wall impedance we assume the average beta value of the machine, which is a reasonable choice regarding the allocation of its effect all around the machine. Between IPs a linear phase advance is presumed.

The geometry and material parameters used for the resistive wall computation are given in Tab. 6.2 and 6.3. As starting conditions we choose to inject bunches with a fixed offset of $x, y = 0.1$ mm and zero deflection angle $x', y' = 0.0$ rad. According to the almost circular-symmetric geometry in LHC, only the vertical plane will be shown in the analysis, although both planes were simulated.

Resistive Wall Turn Memory Using Eq. 5.1 or 5.2 we can estimate the number of turns for the resistive wall memory in the simulation. With the wall thickness $t = 75 \cdot 10^{-6}$ m, the vacuum chamber inner radius $b = 19 \cdot 10^{-3}$ m, the skin depth $\delta_0 = 112 \cdot 10^{-6}$ m at the revolution frequency and the parameter $r = 1$ (perfect conductor outside) we find again two solutions corresponding to 0.04 turns and 146 turns. The second method to estimate the required memory yields a decay length of 36 turns.

The simulation program currently supports summations of up to 100 turns, hence the results for LHC were obtained with the turn memory set to

$$\tau_{\mathrm{mem}}/T_0 = 100\,\mathrm{turns}, \quad \text{where } T_0 \text{ revolution time.}$$

Coupled-bunch mode analysis The analysis of the coupled-bunch modes is done in the same way as described already in Sec. 5.5.1. We use the EFEM system, the equidistant filling eigen-mode system. Hence for LHC with 3564 bunches possible in a complete filling we have 3564 coupled-bunch modes.

6.3 Resistive Wall Instability in the LHC

First we will consider the resistive wall effect in the LHC *without* collimators included. Already the resistivity of the beam screen alone can cause instable beam behavior. The growth is especially important at top energy, where only the beam-beam effect and the octupoles will provide Landau damping and no feedback will be used.

It is interesting to compare the two resistive wall wake functions which we have at our disposal, see also Chap. 4. Simulations were done with the classical thick-wall formula (Eq. 4.14) and the resistive thick-wall formula with inductive bypass (Eq. 4.24).

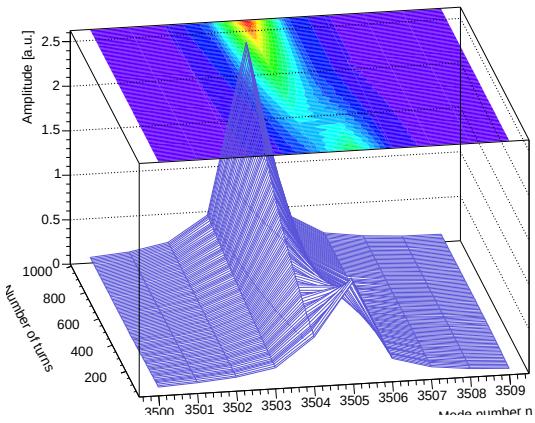

Figure 6.6: *Coupled-bunch mode spectrum of simulation with classical resistive wall wake function and* ***no*** *collimators considered. The most dominant coupled-bunch mode is always* $n = 3504$*. Its growth rate is purely defined by the beam energy and intensity.*

Classical Resistive Wall Impedance Simulation results using the classical thick wall formula (Eq. 4.14) show the behavior depicted in Figs. 6.7–6.8. Coupled-bunch mode $n = 3504$ is always most unstable and the growth rate only depends on the beam energy and its total intensity. Hence for injection energy the growth is faster than for top energy. Nominal intensity gives slightly smaller growths than ultimate intensity.

The values for the growth rate found by simulation are 659±9 turns and 454± 7 turns at injection energy for nominal and ultimate intensity, respectively. At top energy we found growth rates of 10074 ± 1030 turns and 9191 ± 524 turns for nominal and ultimate intensity.

Table 6.6: *LHC collimators, Phase 1 design.*

Collimator Name	Angle [rad]	β_H [m]	β_V [m]	Half Gap [m]	Length [m]
TCP.D6L7.B1	1.571	155.48	80.049	0.001204	0.2
TCP.C6L7.B1	0.0	150.51	82.777	0.0016509	0.2
TCP.B6L7.B1	2.3562	145.64	85.585	0.0014469	0.2
TCP.6L3.B1	0.0	132.552	143.46	0.00387	0.2
TCSG.A6L7.B1	2.469	39.883	226.96	0.0016652	1.0
TCSG.B5L7.B1	2.56	160.0	166.54	0.001998	1.0
TCSG.A5L7.B1	0.706	185.97	145.95	0.0020417	1.0
TCSG.D4L7.B1	1.571	332.5	69.046	0.0013045	1.0
TCSG.B4L7.B1	0.0	139.71	130.97	0.0018557	1.0
TCSG.A4L7.B1	2.368	128.63	141.27	0.0018227	1.0
TCSG.A4R7.B1	0.772	118.24	152.19	0.0018225	1.0
TCSG.B5R7.B1	2.339	121.89	267.55	0.0022048	1.0
TCSG.D5R7.B1	1.01	213.96	158.54	0.0020722	1.0
TCSG.E5R7.B1	2.144	241.5	136.11	0.0020294	1.0
TCSG.6R7.B1	0.008	335.9	47.36	0.0028772	1.0
TCSG.5L3.B1	0.0	54.3454	299.319	0.00294	1.0
TCSG.4R3.B1	0.0	26.3391	393.832	0.00206	1.0
TCSG.A5R3.B1	2.97404	36.5848	341.341	0.00272	1.0
TCSG.B5R3.B1	0.198968	46.4995	310.055	0.00305	1.0

From the Figs. 6.7–6.8 it can be seen that the amplitudes are distributed very smoothly and homogeneously along the bunch train, i.e. the amplitudes vary little within a batch and also very little along the whole bunch train.

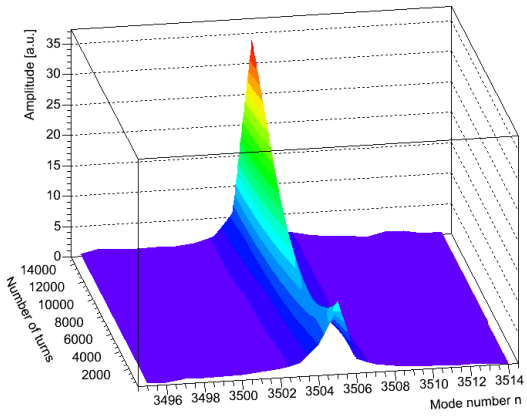

Figure 6.10: *Coupled-bunch mode spectrum of simulation with resistive wall (**inductive bypass** formula) and **no** collimators considered. Most dominant coupled-bunch mode is always $n = 3504$.*

Resistive Wall Impedance with inductive bypass Using the resistive wall impedance model with inductive bypass in the simulation gives slightly lower growth rates but the overall growth behavior does not change as compared to the results obtained with the classical formula. Again mode $n = 3504$ is the most unstable coupled-bunch mode. Fig. 6.9 shows typical results. It is worth to compare these results to Figs. 6.6–6.8, the similarity is very formidable. The agreement is was expected and follows directly from the impedance models.

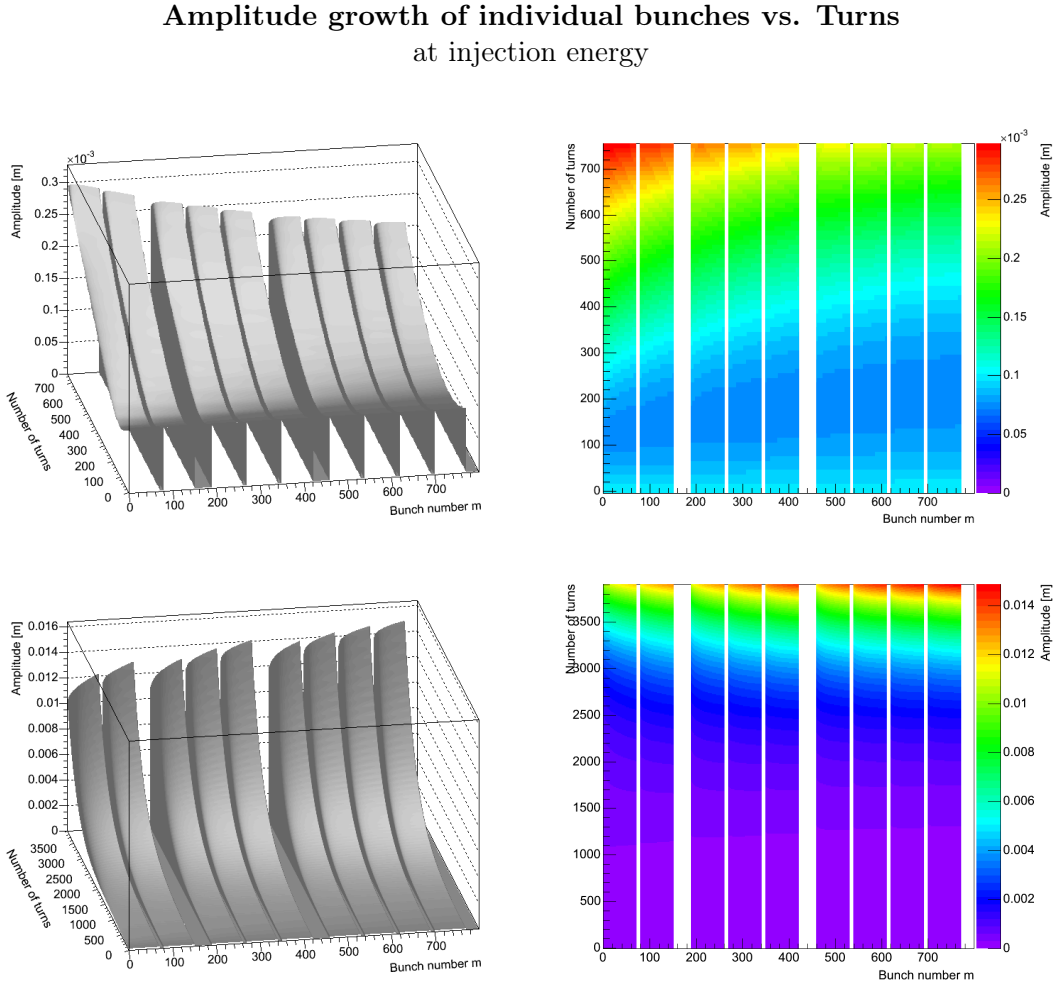

Figure 6.7: *Vertical amplitudes of bunches along the first 9 batches as function of number of turns. Simulation of resistive wall impedance (classical),* ***no*** *collimators included. The top plots show the first 700 turns, where the first batch has largest amplitudes, this changes as can be seen from the lower plots, which show a longer time period.*

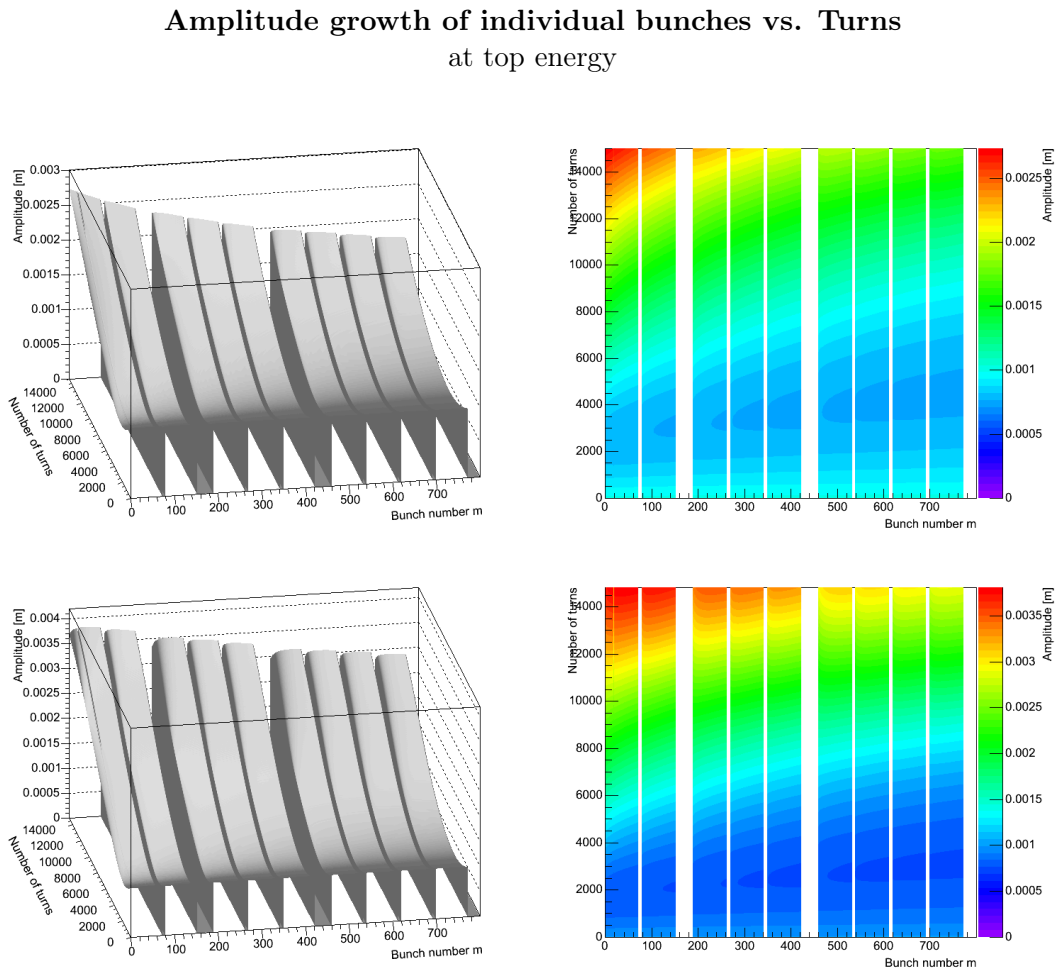

Figure 6.8: *Vertical amplitudes of bunches along the first 9 batches for nominal (top) and ultimate (bottom) intensity as function of number of turns. Simulation of resistive wall impedance (classical),* ***no*** *collimators included. Note the smooth distribution of amplitudes along the bunch train.*

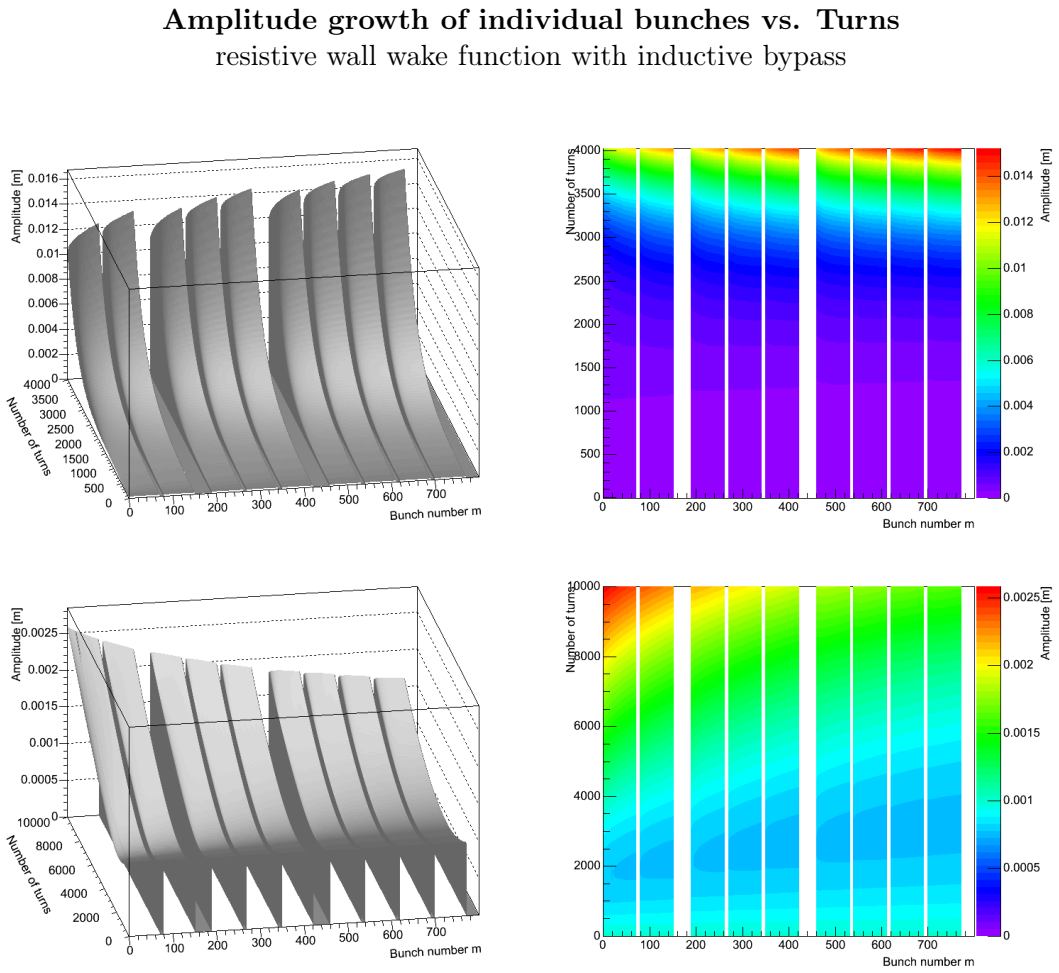

Figure 6.9: *Vertical amplitudes of bunches along the first 9 batches as function of number of turns. Simulation of resistive wall impedance (**inductive bypass** formula), **no** collimators included. The top and bottom plots show the result for nominal/injection and ultimate/top intensity/energy respectively.*

6.4 Collimators

The collimator impedance for a layout with 20 collimators in IR7 and 7 collimators in IR3, has been discussed in the new LHC Design Report [2]. The resistive wall impedance for a single graphite collimator has been estimated analytically [3] and numerically using the code HFSS [39].

The present baseline for Phase 1 given in Tab. 6.6 includes only 4 primary and 15 secondary collimators per beam and the impedance is therefore reduced by about 30%, compared to the references mentioned before. It has been estimated that at 7 TeV, about 60% of the nominal LHC beam intensity can be stabilized using the Landau octupoles [2, Chap.5].

The inclusion of the collimators change the simulation results dramatically.

Classical Resistive Wall Impedance At injection energy of 450 GeV the beam is lost within less than 10 turns for nominal and within less than 7 turns for ultimate intensity if the classical resistive wall wake is assumed. Still the mode $n = 3504$ is the most unstable one.

For top energy (7 TeV) the growth rates of mode $n = 3504$ are found to be $\tau_{turns} = 44.4$ turns and $\tau_{turns} = 29.3$ turns for nominal and ultimate intensity, respectively. The corresponding amplitude growth of bunches is depicted in Fig. 6.11. There, it can also be seen that the amplitudes are still rather smoothly distributed along the bunch train and also inside the batches.

Resistive Wall Impedance with inductive bypass Assuming the thick-wall formula with inductive bypass gives complete different results: Much lower growth rates are obtained in this case. Furthermore, different modes appear in the coupled-bunch mode spectrum. The amplitudes of individual bunches start to show a very strong variation inside the batches. Bunches in the first quarter of the batch show very high amplitudes compared to the rest of the batch. This effect is enhanced with increasing intensity.

This is in contrast to the previous results. The collimators, although only constituting 0.075% of the whole LHC, have a massive impact on the beam stability and on the coupled-bunch modes being driven.

Figs. 6.12–6.15 summarize the results obtained with the collimators included in the simulation model. The strongest coupled-bunch mode at injection energy is $n = 3241$ with growth rates of $\tau_{turns} = 158.6$ turns and $\tau_{turns} = 109.7$ turns for nominal and ultimate intensity, respectively. For top energy mode $n = 3465$ appears to be the strongest one, with growth rates of $\tau_{turns} = 6451$ turns and $\tau_{turns} = 4464$ turns for nominal and ultimate intensity, respectively. However, it should be noted that the error bar on this fitted growth rates is rather large, see also Tab. 6.7.

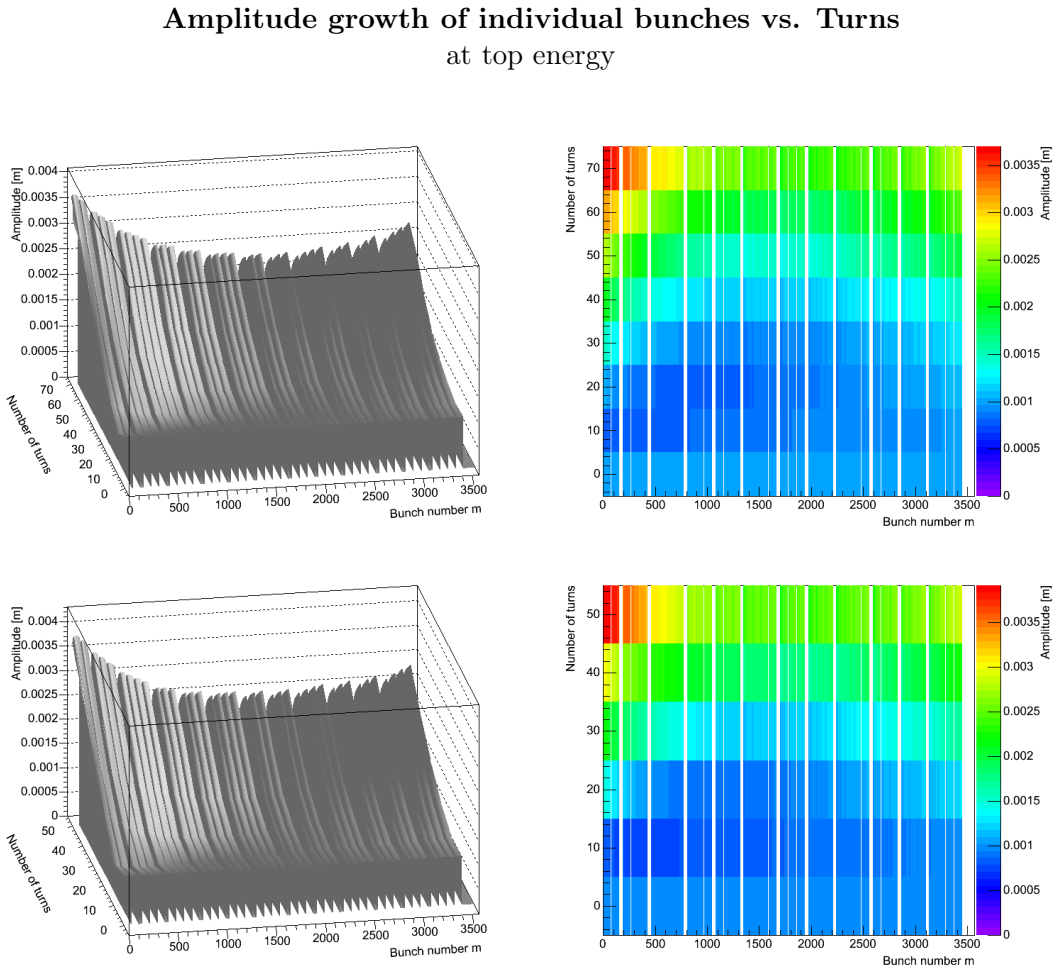

Figure 6.11: *Vertical amplitudes of bunches in the bunch train for nominal (top) and ultimate (bottom) intensity as function of number of turns. Simulation of resistive wall impedance (classical),* ***collimators included****. Note the still smooth distribution of amplitudes along the bunch train!*

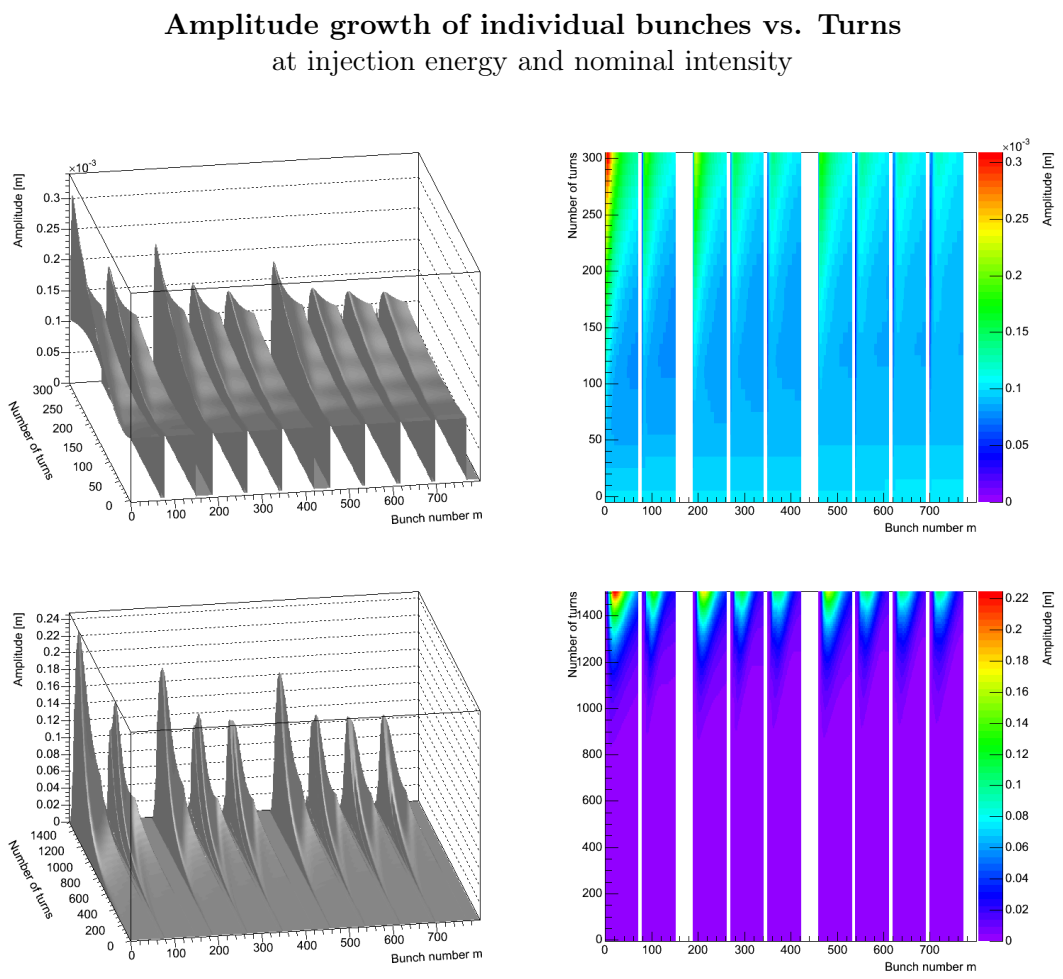

Figure 6.12: *Vertical amplitudes of bunches in the bunch train for the first 300 turns (top) and 1500 turns (bottom). Simulation of resistive wall impedance (**inductive bypass** formula), **collimators included**. Note the strong amplitude variation in the first quarter of each batch!*

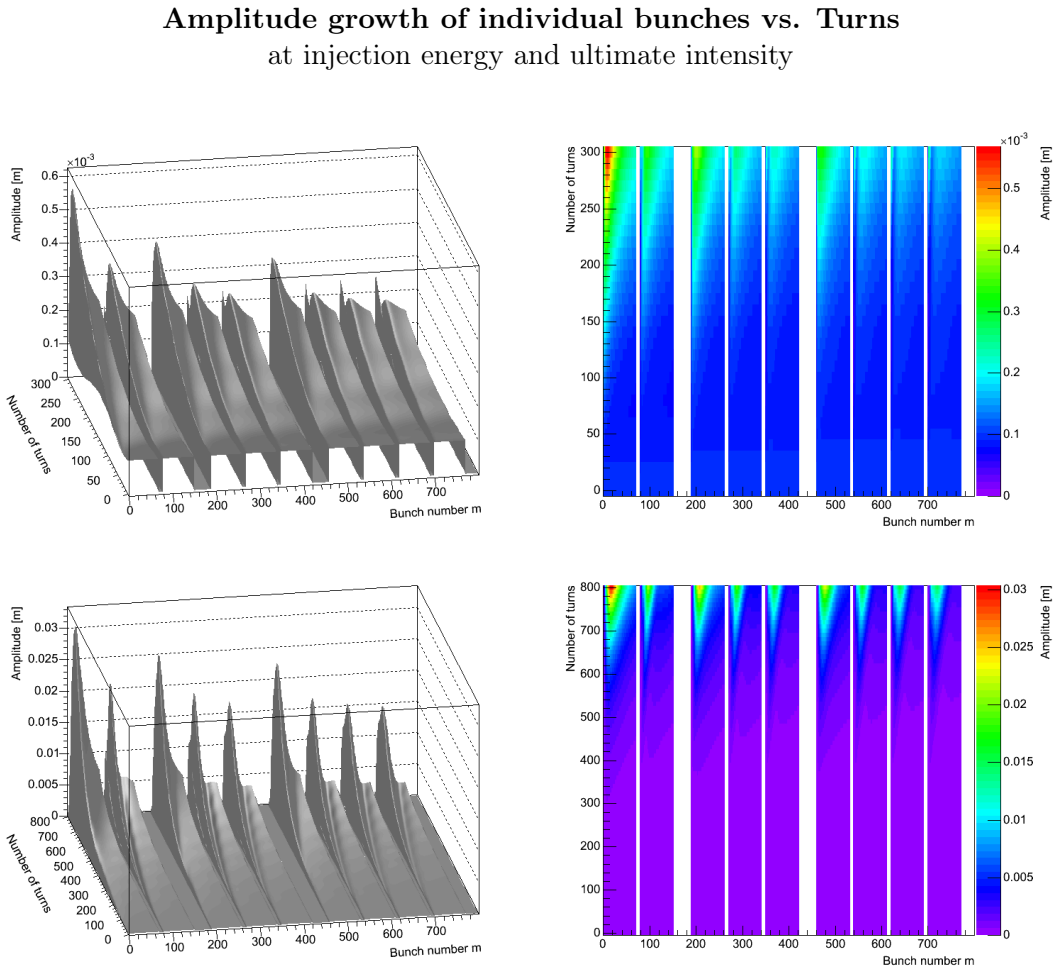

Figure 6.13: *Vertical amplitudes of bunches in the bunch train for the first 300 turns (top) and 800 turns (bottom). Simulation of resistive wall impedance (**inductive bypass** formula), **collimators included**. Higher intensity enhances the amplitude variation in the first quarter of each batch.*

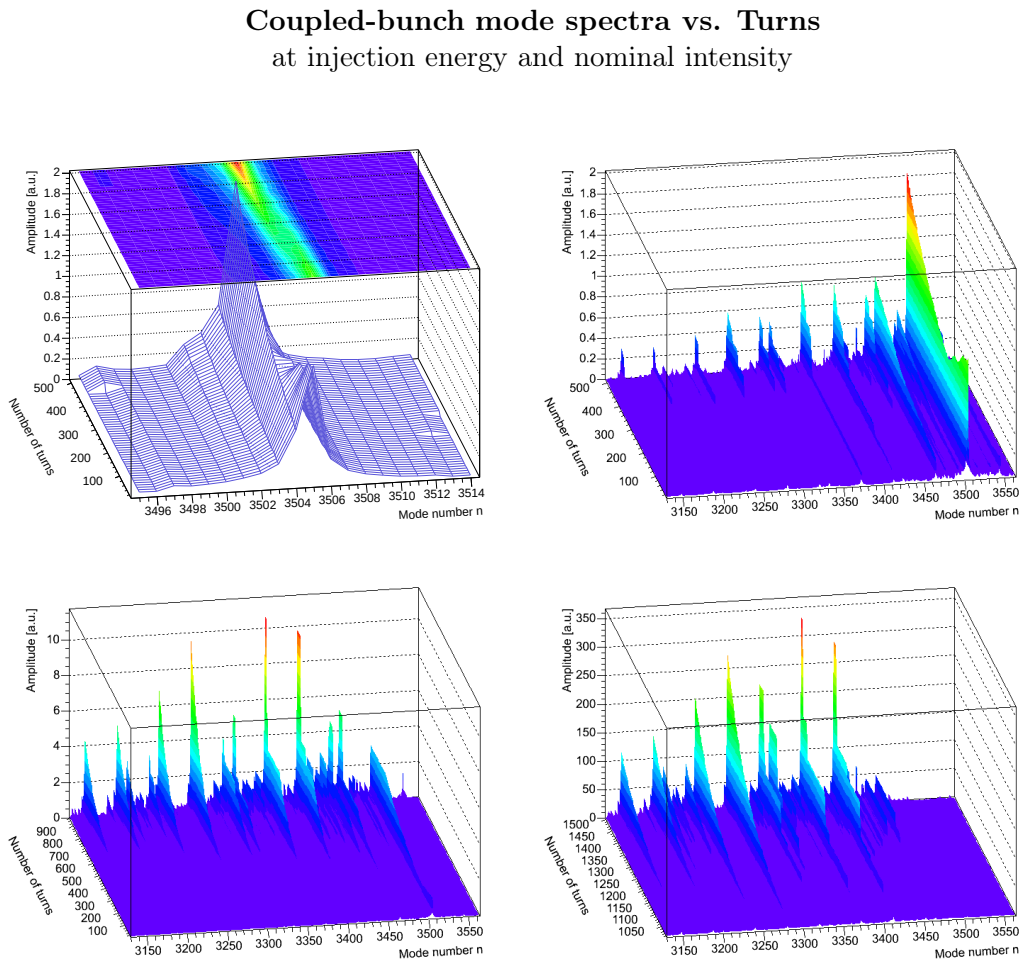

Figure 6.14: *Coupled-bunch mode spectrum of simulation with resistive wall impedance (**inductive bypass** formula) and **collimators included**. The four plots show the mode spectrum over different time scales, first mode $n = 3505$ is present after injection but dying out and mode $n = 3504$ rises. But then the modes $n = 3189, 3241, 3281, 3373, 3413$ start the grow stronger then mode $n = 3504$.*

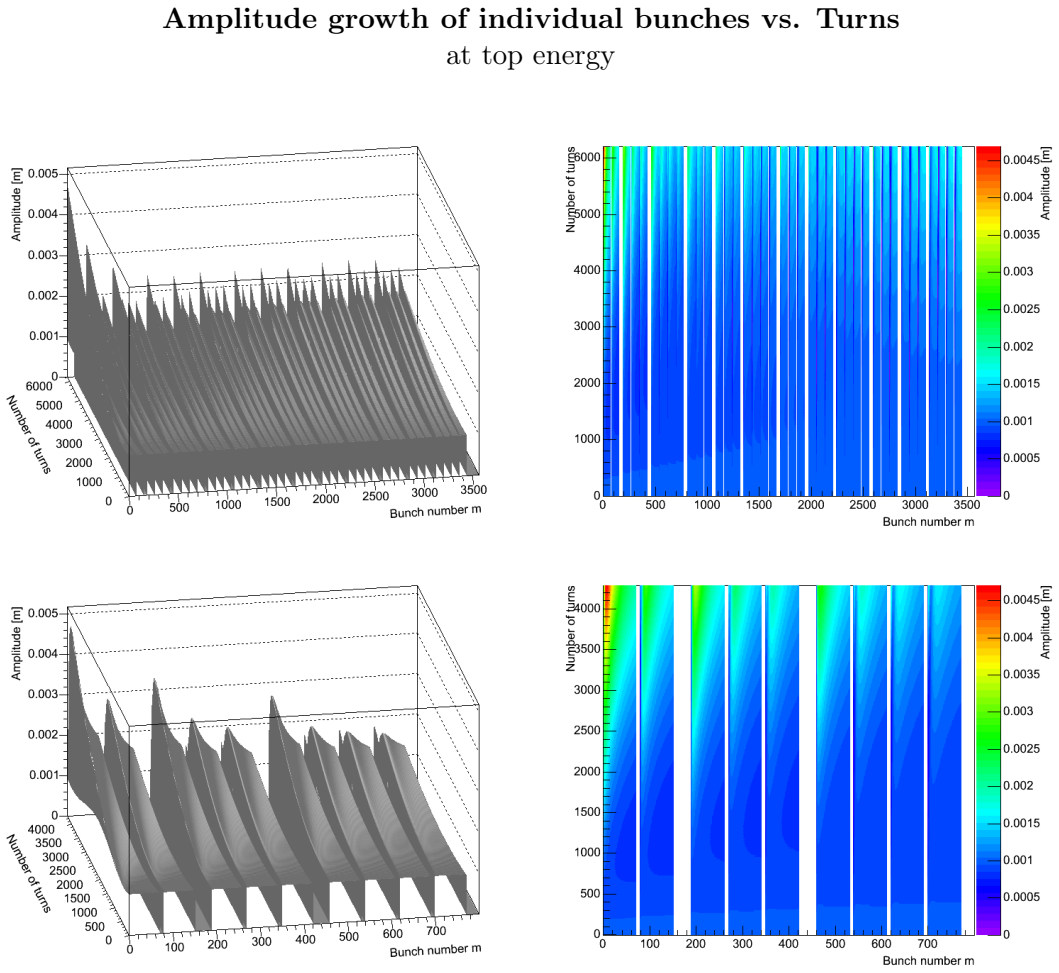

Figure 6.15: *Vertical amplitudes of bunches in the bunch train for nominal (top) and ultimate (bottom) intensity as function of turns. Simulation of resistive wall impedance (**inductive bypass** formula), **collimators included**. Higher intensity enhances the amplitude variation in the first quarter of each batch.*

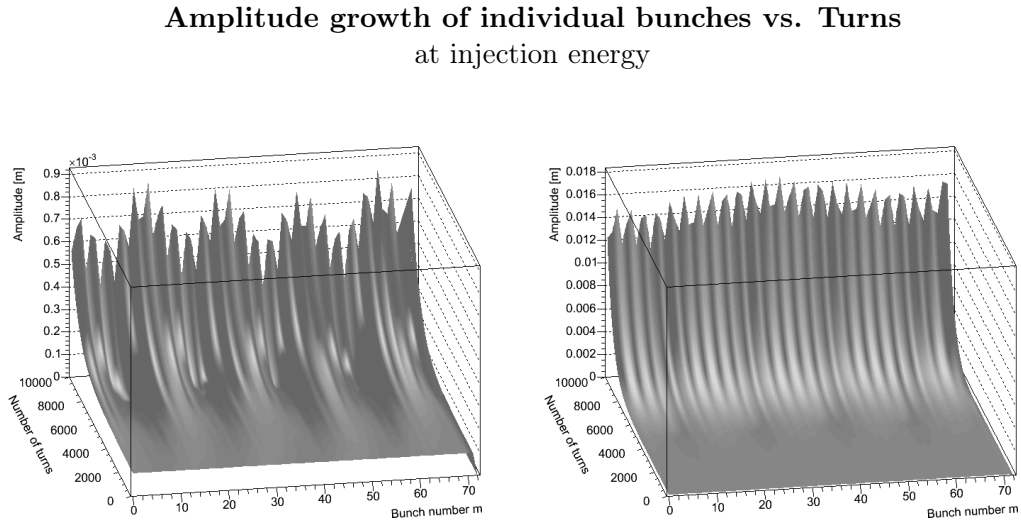

Figure 6.17: *Vertical amplitudes of bunches in the first batch for nominal (left) and ultimate (right) intensity as function of turns. Simulation of undamped modes (HOMs) of the 200 MHz cavities in LHC.*

6.5 Higher Order Modes

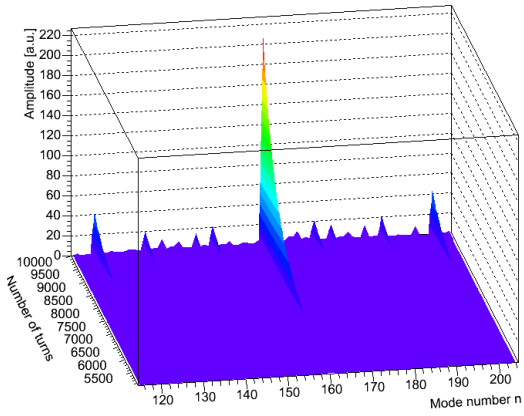

Figure 6.16: *Coupled-bunch mode spectrum of simulation with HOMs. Most dominant coupled-bunch mode is* $n = 160$.

The effect of Higher Order Modes in the LHC was simulated as well. However the effect was found to be very small in the simulation. The undamped modes of the 200 MHz capture cavities of LHC, reported in [3] were used. The growth rate of mode $n = 160$ at injection energy was found to be $\tau_{turns} = 1441$ turns and $\tau_{turns} = 994$ turns for nominal and ultimate intensity, respectively. The values compare very well to the ones reported in [3]. At top energy almost no growth was seen.

Fig. 6.17 shows the amplitudes of bunches within the first batch. Clearly, the modulation due to the resonant wakes is visible.

6.6 Non-Linearities providing Landau Damping: Octupoles

In proton machines such as LHC, non-linearities provide an amplitude-dependent detuning of the particles, thus a tune spread. This mechanism is included in the simulation code by octupole elements (usually one octupole per arc). The tune spread provides Landau damping.

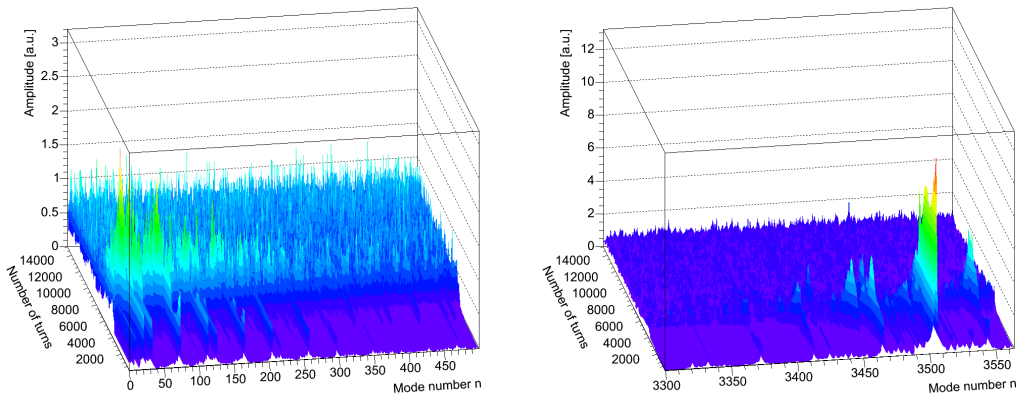

Figure 6.18: *Coupled-bunch mode spectrum of simulation with resistive wall impedance (**inductive bypass** formula), **collimators** and **octupoles** at ultimate intensity. Modes are damped.*

For the simulation with octupoles for Landau damping the parameters reported in [21] have been used. There a scheme of 88 arc octupoles with a length of $l = 0.328$ m and an octupole strength of $O_3 = 62000$ Tm^{-3} was assumed. The same values have been used in the simulation, but the 88 arc octupoles were replaced by one octupole with the strength multiplied by the factor 88.

Top energy was considered, as there the octupoles are the only means to stabilize the beam, apart from the beam-beam tune spread when the beams are brought into collision.

The simulation results are given in Figs. 6.18–6.19 for ultimate intensity. Fig. 6.18 shows the effect of the octupoles on the instability caused by the resistive wall including collimators. One can see, that all modes become eventually damped, when their amplitudes have become large enough for the octupoles to be effective. Fig. 6.19 shows the effect of the octupoles when additionally the undamped HOMs of the 200 MHz cavities are included as well. There, the damping is still visible, although to a lesser degree.

We conclude that the use of octupoles in the simulation code is an appropriate way to introduce Landau damping.

6.7 Summary of Results

We summarize the results of the simulation of LHC in Tabs. 6.7–6.8. The comparison with analytical estimates, which can be found in [3], shows some similarities and the orders of magnitude of the growth rates are the same. But in the simulation we especially find shorter growth times for injection energy and longer growth times for top energy.

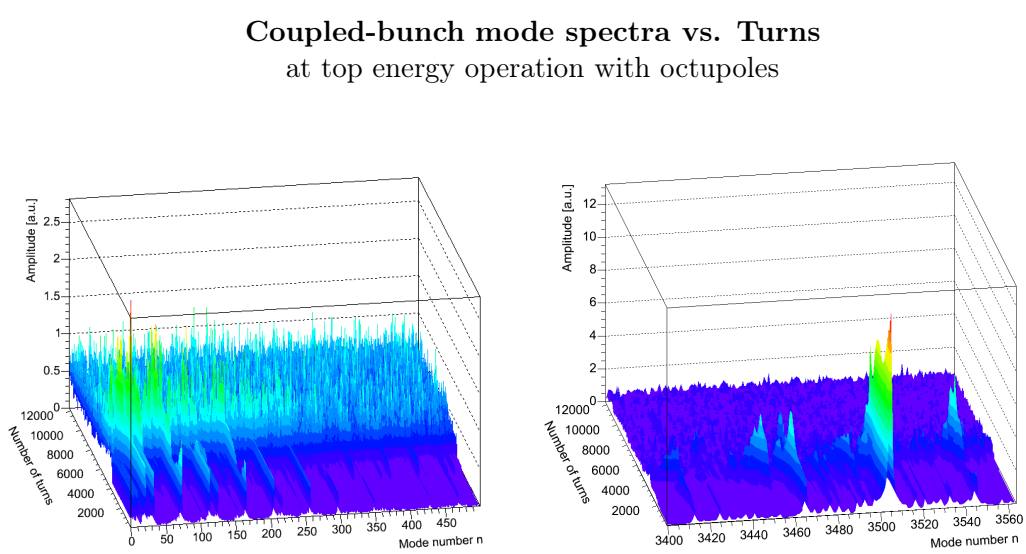

Figure 6.19: *Coupled-bunch mode spectrum of simulation with resistive wall impedance (**inductive bypass** formula), **collimators**, **HOMs** and **octupoles** at ultimate intensity. Modes are damped.*

However there is an effect of the simulation that is important to retain: It stops when the particle phase space coordinates exceed certain limits, i.e. when the particles in the real machine would also be lost. These limits are determined by the RF bucket size and the vacuum chamber dimensions. Therefore the most unstable coupled-bunch mode seen in the simulation need not necessarily be equal to the actual most unstable mode, which may only develop after a certain delay (latency time).

Concerning the operation of LHC we conclude that all growth rates obtained by simulation are in reasonable agreement with estimates from theory. For top energy in LHC even smaller growth is seen by the simulation.

Table 6.7: *Results of the LHC simulation in terms of growth times.*

	LHC injection energy			
	Nominal		Ultimate	
	Mode n	Growth Time τ_{turns} [turns]	Mode n	Growth Time τ_{turns} [turns]
Resistive Wall Classic	3504	659.2 ± 8.7	3504	453.7 ± 6.8
Resistive Wall Classic + Collimator	< 10 turns		< 7 turns	
Resistive Wall Inductive Bypass	3504	677.5 ± 8.7	3504	466.6 ± 7.2
Resistive Wall Inductive Bypass + Collimator	3149	167.8 ± 5.3	3149	115.8 ± 4.1
	3189	160.0 ± 4.6	3189	110.4 ± 3.6
	3241	158.6 ± 3.9	3241	109.7 ± 3.0
	3281	161.6 ± 3.2	3281	112.0 ± 2.7
	3373	162.2 ± 4.3	3373	119.0 ± 3.5
	3413	167.3 ± 4.5	3413	124.9 ± 3.7
	(3504)	(357.8 ± 395.3)	(3504)	(261.5 ± 259.8)
HOMs	160	1441.1 ± 114.9	160	994.0 ± 11.9

	LHC top energy			
	Nominal		Ultimate	
	Mode n	Growth Time τ_{turns} [turns]	Mode n	Growth Time τ_{turns} [turns]
Resistive Wall Classic	3504	10073.5 ± 1029.0	3504	9191.2 ± 523.8
Resistive Wall Classic + Collimator	3504	44.4 ± 40.9	3504	29.3 ± 29.3
Resistive Wall Inductive Bypass	3504	10592.1 ± 1571.8	3504	8340.3 ± 911.2
Resistive Wall Inductive Bypass + Collimator	3464	7057.2 ± 4342.9	3464	4957.9 ± 3753.4
	3465	6451.6 ± 7658.7	3465	4464.3 ± 5719.9
	3504	7352.9 ± 3746.8	3504	4310.3 ± 2285.2
HOMs	no growth visible		no growth visible	
Resistive Wall + Collimator + OCT	damped		damped	

Table 6.8: *Results of the LHC simulation in terms of growth times.*

	LHC injection energy			
	Nominal		Ultimate	
	Mode n	Growth Time τ [msec]	Mode n	Growth Time τ [msec]
Resistive Wall Classic	3504	58.622 ± 0.773	3504	40.349 ± 0.604
Resistive Wall Classic + Collimator	< 10 turns		< 7 turns	
Resistive Wall Inductive Bypass	3504	60.251 ± 0.776	3504	41.498 ± 0.639
Resistive Wall Inductive Bypass + Collimator	3149	14.921 ± 0.476	3149	10.294 ± 0.367
	3189	14.229 ± 0.410	3189	9.817 ± 0.324
	3241	14.105 ± 0.349	3241	9.754 ± 0.270
	3281	14.374 ± 0.283	3281	9.956 ± 0.240
	3373	14.425 ± 0.379	3373	10.582 ± 0.314
	3413	14.876 ± 0.3985	3413	11.104 ± 0.329
	(3504)	(31.818 ± 35.153)	(3504)	(23.256 ± 23.104)
HOMs	160	128.160 ± 10.214	160	88.400 ± 1.054

	LHC top energy			
	Nominal		Ultimate	
	Mode n	Growth Time τ [msec]	Mode n	Growth Time τ [msec]
Resistive Wall Classic	3504	895.840 ± 91.506	3504	817.371 ± 46.578
Resistive Wall Classic + Collimator	3504	3.947 ± 3.634	3504	2.603 ± 2.602
Resistive Wall Inductive Bypass	3504	941.955 ± 139.782	3504	741.701 ± 81.037
Resistive Wall Inductive Bypass + Collimator	3464	627.594 ± 386.211	3464	440.902 ± 333.792
	3465	573.742 ± 681.087	3465	397.009 ± 508.668
	3504	653.897 ± 333.199	3504	383.319 ± 203.225
HOMs	no growth visible		no growth visible	
Resistive Wall + Collimator + OCT	damped		damped	

Chapter 7

Conclusions

The goal of this thesis was to develop a simulation program that allows the study of multi-bunch and/or multi-turn instabilities and other collective effects in high energy proton machines which typically have a large number of bunches. In particular since radiation damping is weak in proton machines, such a simulation code would require exceedingly long computation times.

Approximations to make such a simulation feasible in terms of computation time have been motivated and discussed in Chap. 3. In particular, an algorithm which allows fast summation of the long-range wakes of individual bunches, based on the convolution theorem and the discrete FFT, has been adapted and incorporated in the code. Also by using the rigid-dipole approximation, which considers only the center-of-mass oscillations, the wake potentials can be replaced by wake functions in the long-range regime. These approximations simplify the simulation but still retain the accuracy required to describe the beam motion in an actual accelerator or storage ring.

Different resistive wall impedance models, which can be used to characterize the impedance of the vacuum chamber walls and the collimators in the LHC have been reviewed and compared in Chap. 4. For simulation in the time domain the wake function corresponding to the most likely impedance model has been derived.

Measurements in the SPS have been carried out to verify the results of the code. The agreement has been found to be quite satisfactory. Also predictions have been made for the upcoming test of an LHC collimator prototype which has been installed in the SPS.

In the final Chap. 6 the performance limitations of the LHC due to collective effects have been investigated. At injection energy the beams in the LHC have been found to be unstable without transverse feedback. At top energy the feedback must be switched off and Landau damping by octupoles is required. The simulation showed that the proposed octupole strengths are adequate to damp coupled-bunch modes due to resistive wall effect and HOMs.

The simulation code *MultiTRISIM* has been developed originally for the LHC, but should be equally valuable for the simulation and analysis of multi-bunch instabilities in other circular proton accelerators and/or storage rings. The simulation models and analyzing tools presented in this thesis, should also facilitate the interpretation of measurements in multi-bunch machines.

Bibliography

[1] Proc. of 1st International School of Particle Accelerators at the "Ettore Majorana"Centre for Scientific Culture – Theoretical aspects of the behaviour of beams in accelerators and storage rings. CERN Yellow report. CERN, Geneva, 19 Jul 1977. 10–22 Nov 1976, Erice, Italy; CERN-77-13, 484 p.

[2] *The LHC Design Report*, volume Vol. I, The LHC Main Ring. 2004.

[3] D. Angal-Kalinin and L. Vos. Coupled bunch instabilities in the LHC. 8th European Particle Accelerator Conference: A Europhysics Conference, La Vilette, Paris, France, 3-7 Jun 2002.

[4] D. Brandt. SIMTRAC: A simulation program for tracking longitudinal and transverse single bunch effects. CERN-LEP-NOTE-512.

[5] D. Brandt. Simulation of longitudinal single bunch effects in LEP. CERN-ISR-TH-82-09.

[6] P. J. Bryant and K. Johnsen. The principles of circular accelerators and storage rings. Cambridge, UK: Univ. Pr. (1993).

[7] A. Burov. Private communication. 2004.

[8] A. Burov and V. Lebedev. Proc. EPAC 2002, p.1452.

[9] A. Burov and V. Lebedev. Transverse resistive wall impedance for multi-layer round chambers. Presented at 8th European Particle Accelerator Conference (EPAC 2002), Paris, France, 3-7 Jun 2002.

[10] A. Chao. Physics of Collective Effects, Wiley 1995.

[11] A. Chao, S. Heifets, and B. Zotter. Tune shifts of bunch trains due to resistive vacuum chambers without circular symmetry. *Phys. Rev. ST Accel. Beams*, 5:111001, 2002.

[12] A. W. Chao. Physics of collective beam instabilities in high-energy accelerators. Wiley Series in Beam Physics and Accelerator Technology. John Wiley & Sons, Inc., New York, 1993. 371 p.

[13] A. W. Chao, (ed.) and M. Tigner, (ed.). *Handbook of accelerator physics and engineering*. World Scientific Publishing Co. Pte. Ltd., Singapore, 1999. 650 p.

[14] W. Chou and F. Ruggiero. Anomalous skin effect and resistive wall heating. *LHC Project Note*, 1995. LHC-PROJECT-NOTE-2 (SL/AP).

[15] R. C. Davidson and H. Qin. *Physics of intense charged particle beams in high energy accelerators*. ICP Imperial College Press, London, UK, 2001. 583 p.

[16] D.A. Edwards and M.J. Syphers. An introduction to the physics of high energy accelerators. Wiley Series in Beam Physics and Accelerator Technology. John Wiley & Sons, Inc., New York, 1993. 292 p.

[17] M. Frigo and S.G. Johnson. FFTW: Fastest Fourier transform in the west. World Wide Web, `http://www.fftw.org/`. last visited: June 2004.

[18] M. Frigo and S.G. Johnson. FFTW: An adaptive software architecture for the FFT. In *Proc. 1998 IEEE Intl. Conf. Acoustics Speech and Signal Processing*, volume 3, pages 1381–1384. IEEE, 1998.

[19] R. Gluckstern. CERN yellow report 2000-011 (2000).

[20] B. Goddard. Expected delivery precision of the injected LHC beam. *LHC Project Note*, Feb 2004. LHC-PROJECT-NOTE-337.

[21] J.P. Koutchouk and F. Ruggiero. A summary on Landau octupoles for the LHC. *LHC Project Note*, 1998. LHC-PROJECT-NOTE-163.

[22] M. Krassilnkov, A. Novokhatski, T. Weiland, W. Koch, and P. Castro. V-code on-line simulation of collective beam effects. ICAP2000. http://www.icap2000.de/.

[23] J. Laslett, K. Neil, and A. Sessler. Rev.Sci.Instr. (1965).

[24] J. Laslett, K. Neil, and A. Sessler. *Rev.Sci.Instr.*, 1965.

[25] A. Mostacci, F. Caspers, and U. Iriso. Bench measurements of low frequency transverse impedance. *CERN-AB-2003-051-RF*. Proc. of Particle Accelerator Conference (PAC 03), Portland, Oregon, 12-16 May 2003.

[26] G. Nassibian and F. Sacherer. Methods for measuring transverse coupling impedances in circular accelerators. *Nucl. Instrum. Meth.*, 159:21–27, 1979. Also available as: CERN-ISR-TH-77-61, CERN-PS-BR-77-40.

[27] A. Novokhatski and T. Weiland. Self-consistent model for the beams in accelerators. *eConf*, C980914:69–73, 1998.

[28] A. Novokhatsky and T. Weiland. The model of ensembles for the beam dynamics simulation. Prepared for IEEE Particle Accelerator Conference (PAC 99), New York, New York, 29 Mar - 2 Apr 1999.

[29] V. Nys. Computer simulation of the longitudinal motion including the wake field force, using a hermite polynomial expansion. CERN-LEP-TH/86-34.

[30] F. Pedersen. *Multibunch Instabilities.* Springer-Verlag, Berlin, 1994. In Proceedings of Topical Course on Particle Accelerators, Benalmádena, Spain, 1992, Frontiers of Partcile Beams: 425.

[31] S. Prabhakar. New diagnostics and cures for coupled-bunch instabilities. SLAC-R-554.

[32] W.H. Press, B.P. Flannery, S.A. Teukolsky, and W.T. Vetterling. *Numerical Recipes in Fortran.* Cambridge University Press, Cambridge, UK, 1992.

[33] F. Ruggiero. Single beam collective effects in the LHC. *Part. Accel.*, 50:83–104, 1995. CERN-SL-95-09-AP, CERN-LHC-NOTE-313.

[34] G. Sabbi. Simulation of single bunch collective effects in lep by linear expansion of the distribution moments. *CERN-SL Technical Report*, 1995. CERN-SL-95-25-AP.

[35] F. J. Sacherer. Transverse bunched beam instabilities. theory. (talk). Proceedings of Ninth International Conference On High Energy Accelerators, Stanford 1974, Springfield 1975, 347-351.

[36] S. D. Strasburg. *Dynamics Of Intense Charged-particle Beams.* PhD thesis, Princeton Univ., Princeton, NJ, 2001. 280 p.

[37] D. Sundararajan. *The discrete Fourier transform.* World Scientific Publishing Co. Pte. Ltd., Singapore, 2001.

[38] K. Thompson and R. D. Ruth. Transverse coupled bunch instabilities in damping rings of high-energy linear colliders. *Phys. Rev.*, D43:3049–3062, 1991.

[39] H. Tsutsui. Resistive wall impedance of an LHC collimator. *LHC Project Note*, Jul 2003. LHC-PROJECT-NOTE-318.

[40] L. Vos. The impedance of multi-layer vacuum chambers. *CERN-AB-Note*, Oct 2003. CERN-AB-2003-093-ABP.

[41] L. Vos. The transverse impedance of a cylindrical pipe with arbitrary surface impedance. *CERN-AB-Note*, Feb 2003. CERN-AB-2003-005-ABP.

[42] A. Wagner. *3-dimensional simulation of collective effects in particle accelerators.* PhD thesis, TU Graz, Graz, Austria, 1997.

[43] T.S. Wang. Hersim2. CERN/SL/90-08-AP.

[44] E. J. N. Wilson. *An Introduction to Particle Accelerators.* New York, 2001. 252 p.

[45] S. Wolfram. Mathematica (1991).

[46] K. Yokoya. Restive wall impedance of beam pipes of general cross- section. KEK-PREPRINT-92-196.

[47] B. Zotter. Transverse oscillations of a relativistic particle beam in a laminated vacuum chamber. *CERN 69-15*, 1969.

[48] B. W. Zotter and S. A. Kheifets. *Impedances and wakes in high-energy particle accelerators*. World Scientific Publishing Co. Pte. Ltd., Singapore, 1998. 405 p.

[49] B. W. Zotter and S. A. Kheifets. *Impedances and wakes in high-energy particle accelerators*. World Scientific Publishing Co. Pte. Ltd., Singapore, 1998. p.170.